POLITECNICO
MILANO 1863

POLITECNICO DI MILANO
DEPARTMENT OF ELECTRONICS, INFORMATION AND BIOENGINEERING
DOCTORAL PROGRAMME IN BIOENGINEERING

XXVIII CYCLE

INVESTIGATION OF ALTERNATIVE IMAGING METHODS TO IMPROVE ACCURACY IN CANCER THERAPY WITH CARBON IONS

Doctoral Dissertation of:
Marta F. Dias

Advisors:
Professor Marco Riboldi and Professor Guido Baroni

External Advisor:
Professor João Seco

Tutor:
Professor Manuela Teresa Raimondi

2016

Para ti Mãe, para ti Pai, para aqueles a quem não disse adeus e para ti Marta do futuro...

To you Mum, to you Dad, to the ones I couldn't say goodbye and to you future Marta...

Acknowledgments

This work has been funded by the grant SFRH/BD/85749/2012 from Fundação para a Ciência e a Tecnologia (FCT).

First of all, I would like to express the deepest appreciation to my two main supervisors Professor Marco Riboldi and Professor João Seco. To Professor Marco Riboldi for the exchange of ideas and all the support throughout all of these years. To Professor João Seco for pushing me, showing that there are no limits to where research can go.

Secondly, but not less important, my colleague and friend Charles-Antoine Collins-Fekete. I cannot express with words how much I am grateful for all the shared ideas, support and help. I am certain that without him (you) this work would not be possible and I will never be able to thank him (you) for all the work and friendship.

Thirdly to those who did not contribute directly to my work but were there supporting me and making my live more cheerful. Ana Manata and Mario Girasa you two were without any question the two people I interacted the most and that I have the pleasure to call my best friends. Ana, for trying to show me the beauty and the positive side of the world even though annoying me constantly. Mario, my husband, for showing me how sick our world is but that there is always a bright side and we

can always make it better just by being happy.

Finally, to my family. À minha irmã bia, por estar sempre presente ao lado dos meus pais e por tratar deles. Aos meus pais, sem dúvida as pessoas mais importantes da minha vida e todos os sacríficios e decisões que tomei na vida, mesmo que muitas vezes não parecendo, foram sempre tomadas a pensar em neles.

Contents

List of Figures

List of Tables

Acronyms

Symbols =
α = helium.
A =
ART = Algebraic Reconstruction Technique.
B =
BP = Bragg peak.
C =
c-rad = carbon radiography.
CDRR = Carbon Digitally Reconstructed Radiography.
CNAO = Centro Nazionale di Adroterapia Oncologica.
CSP = Cubic Spline Path.
CT = Computed Tomography.
D =
DECT = dual-energy computed tomography.
DNA = Deoxyribonucleic Acid.
F =
FWHM = Full-Width-Half-Maximum.
G =
GPU = Graphics Processing Unit.
H =

HIT = Heidelberg Ion Therapy Center.
HU = Hounsfield Units.
I =
IC = Ionization Chamber.
IMPT = Intensity-Modulated Proton Therapy.
L =
LET = Linear Energy Transfer.
M =
MC = Monte Carlo.
MCS = Multiple Coulomb Scattering.
MLP = Most Likely Path.
MRI = magnetic resonance imaging.
O =
OAR = Organ at Risk.
OER = Oxygen Enhancement Ratio.
P =
p-CT = proton computed tomography.
p-rad = proton radiography.
PET = Positron Emission Tomography.
PMMA = polymethyl methacrylate.
R =
RBE = Relative Biological Effectiveness.
RMS = Root Mean Square.
RSP = Relative Stopping Power.
S =
SLP = Straight Line Path.
SOBP = Spread-Out Bragg Peak.
SP = Stopping Power.
W =
WEPL = Water Equivalent Path Length.
WET = Water Equivalent Thickness.

Abstract

THE interest in carbon therapy for cancer treatment has been growing. However, in order to take full advantage of their depth-dose curve, precise knowledge of their range and patient interfaces is necessary. Range uncertainties in carbon therapy are significant due to the current method to determine the range, which uses X-ray CT and a calibration curve, and due to patient variations. The purpose of this dissertation was to find possible solutions to decrease range uncertainties. The first method consisted in optimizing the elemental ionization values in the calculation of the relative stopping powers in order to obtain a better estimation of the calibration curve. The second method involved a phenomenological approach which predicted carbon paths trajectories better than using straight path trajectories (root mean square error was reduced by 50 %). The third method, used multiple Bragg peak detection in order to obtain knowledge about the tumor edge position in a high contrast medium. The method avoided irradiation of multiple angles/positions and provided 1mm accuracy in the determination of the tumor edge. Finally, the forth and last method proposed the use of charged particle (protons, carbons and heliums) radiography combined with X-ray CT to obtain a patient-specific calibration curve to be used for carbon range calculations. The obtained results were extremely promising with maximum range errors of 1.5mm for helium radiography. These results suggest that helium radiography might be the method of choice for future carbon and proton treatment planning. The results derived in the different chapters of this dissertation show that carbon therapy accuracy can be increased with respect to current clinical practice.

Summary

According to the World Health Organization (WHO), cancer is a leading cause of death worldwide, with approximately 14 million new cases and 8.2 million cancer related deaths in 2012. A 70% increase in new cases of cancer is expected over the next 2 decades [WHO16].

In recent years, the interest in using charged particles, such as protons and carbon ions, has shown a considerable increase with more than 140000 patients being treated in 2015 [Jer15]. The most common form of charged particle therapy is performed with hydrogen ions (protons). However, new facilities have been built to provide cancer treatment using carbon ions due to its higher Linear Energy Transfer (LET) and Relative Biological Effectiveness (RBE). Over the past ten years the number of patients treated with carbon ions has doubled [Jer15].

The growing interest in charged particle therapy can be explained by their characteristic depth-dose curve. This shows a low and nearly flat energy deposition in the entrance point, it increases with the penetration depth until it reaches a maximum (Bragg peak) followed by a steep fall to approximately zero.

In theory, when properly modeled, charged particle therapy allows the delivery of a defined dose distribution within the target volume and barely none outside of it. However, there is still a large number of uncertainties in determining the range of charged particles inside the patient.

In the clinical environment these uncertainties are accounted by increasing the target margins up to 3.5%±1mm [Pag12a]. Such margins implicate an increase dose to nearby healthy organs, and depending on the treatment site, these can lead to severe side-effects to the patient [SPW+12].

Range uncertainties can come from different sources. They can be random, due to errors in patient positioning, organ motion, chemical variations in the patient tissues, and beam fluctuations [KMS+14]. And/or they can be systematic, due to the fact that treatment planning is made using X-ray Computed Tomography (CT).

The range calculation of charged particles is currently performed by converting Hounsfield Units (HU) from the X-ray CT into Relative Stopping Power (RSP) [SPL96a]. Through the RSP, which measures the ratio between the tissue stopping power and water stopping power, it is possible to determine the particle's range inside the patient and place the Bragg peak within the pre-defined margins. X-rays behave very differently from charged particles when crossing matter. Therefore, the conversion between HU to RSP contains errors that in some situations can be up to 5% [YZP+12].

The current state-of-the-art calibration is known as the stoichiometric method, which was proposed by Schneider *et al.* [SPL96a]. In order to calculate the tissues RSP, the stoichiometric method requires precise knowledge of the tissue composition and ionization energy (I-value). There are different literature sources for such values, therefore there is not precise knowledge of the tissue composition and I-value, leading to uncertainties in the calibration method.

Another issue with the stoichiometric method is that it only works on human-like materials. Surgical implants materials are not accounted having significantly larger errors in the range calculations. This prevents treatment through such implants since errors up to 18% can be intro-

duced in the range calculation [JR14].

Different methods have been proposed to deal with range uncertainties. Such is the case of the measurement of PET and prompt gamma produced during treatment with charged particles. These methods provide knowledge about the dose delivered and range verification, respectively [MMRea69, MKYK06]. However, both methods still need to deal with low statistic issues. Another method that has been proposed is charged particle radiography/CT.

Charged particle radiography/CT uses charged particles with energy high enough to cross the patient. From the measured residual range/energy it is possible to obtain information about the particle's range inside the body. However, charged particle radiography/CT is still limited by physical and technical constraints. In order to produce high quality images, correct knowledge of the particles path is necessary which can lead to long reconstruction times. Also, full coverage of the patient is necessary for charged particle CT, which requires long acquisition times and in the case of carbon imaging, it is limited by the fact that clinical accelerators are not able to accelerate carbons to energies high enough to cross all areas of the patient body. Having correct knowledge of carbon's range and interface positions in the body it is crucial for an accurate treatment.

The main aim of this dissertation was to investigate alternative methods which rely on charged particle imaging principles to reduce range uncertainties in carbon therapy.

Objectives and dissertation outline

In each chapter a specific aim is considered:

Chapter 1, the aim of this chapter is to summarize the basic concepts behind charged particle therapy, what are the major drawbacks/uncertainties and the current research trends on this topic.

Chapter 2, in this chapter two different approaches are shown, whose

aim is to reduce range uncertainties. The first idea does not involve charged particle imaging. But it is related with the RSP calculation that currently is performed through the stoichiometric method which converts HU values in RSP. The aim of this work is to show that by optimizing the elemental I-values using experimental measurements it is possible to obtain a better calibration curve. In the second part of this chapter the aim is to develop a phenomenological formulation which allows a better estimation of charged particle's path using the cubic spline path formalism. This formalism increases spatial resolution in charged particle radiography/CT, hence providing better range prediction.

Chapter 3 proposes a method which is based on the principles behind carbon imaging with a range detector. The aim of this chapter is to obtain tumor edge positioning through multiple Bragg peak detection in a range detector. The method avoids irradiation of the patient over different angles/positions, consequently leading to low dosage.

Chapter 4, the aim of this chapter is to show that by using charged particle radiography combined with X-ray CT it is possible to obtain a patient specific calibration curve which can be used to predict carbon range for cancer treatment.

Chapter 5, summarizes the results and conclusions derived in the previous chapters.

The proposed methods, even though relying on imaging principles, *i.e.* detection of high energetic carbons/heliums/protons after irradiation of the patient, do not involve carbon CT and imaging reconstruction methods. The results derived in the different chapters of this dissertation show that carbon therapy accuracy can be increased from what it is currently performed in clinical environment, however, there is still room for improvements and clinical experimentation should be performed on the proposed methods.

CHAPTER 1

Background information

1.1 Brief history and current status of charged particle therapy

In 1946 Dr. Robert R. Wilson, a physicist who had worked in the development of particle accelerators, suggested the use of charged particles (protons and heavy ions) as a possibility for cancer radiation treatment. His argument was based on the depth-dose distribution presented by these particles which could be suitable to treat tumors in humans [Wil46]. An energetic charged particle beam deposits a great part of its energy at the end of its range, resulting in what is called the Bragg peak (BP) (Figure 1.1). However, as shown in Figure1.1, the BP is very narrow and usually not enough to cover most treatment volumes. Therefore, Wilson also proposed a technique, still used today, for modulation of the beam in depth. He proposed to use a range wheel that creates beams with different energies and peak positions. When superimposed, the beams produce the Spread-Out Bragg Peak (SOBP) which provides a delivery of an uniform dose to the tumor volume (Figure1.2). The superposition of multiple BPs leads to higher and uniform dose proximal

to the target with the sharp falloff to its distal part (Figure 1.2).

Other method that has started to be used instead the SOBP method is the Intensity-Modulated Proton Therapy (IMPT) [Lom08]. In this method, the uniform dose distribution over the target volume is constructed only by the combination of two or more treatment fields (different irradiation angles). Each individual field can deliver a highly heterogeneous dose distribution to the target, but when combined lead to a uniform dose over the target.

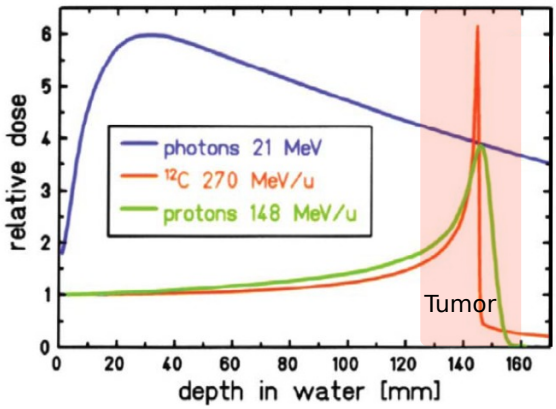

Figure 1.1: *Depth-dose distribution for photons and monoenergetic Bragg curves for carbon ions and protons. The shaded red area represents the tumor area. Figure adapted from [FKAEC09].*

It took less then 10 years for protons to be used to treat cancer patients for the first time [TLB+58]. In 1974, Joseph R. Castro and associates started to study therapy with heavier charged particles aiming to understand its clinical use. Between 1977 and 1992, several clinical experiences using heavy-ions (especially helium, carbon and neon ions) took place at the Lawrence Berkeley Laboratory, where encouraging results (mainly for skull base tumors and paraspinal tumors) were achieved [SEJS06]. However, the cost of developing and delivering heavy ions eventually could not be justified by the relatively limited number of patients leading to a slow development of charged particle therapy [Lin12].

Nowadays, due to the technological development (e.g. accelerators and delivering technology), charged particle therapy with protons and carbon ions has gained again an increasing interest [KFM+10]. Worldwide there are about 60 particle therapy facilities that treat patients with charged particles (protons and/or carbon ions) and more than 30 under construction. Charged particle therapy has been used to treat more than 137000 patients worldwide from 1954 to 2014, ranging different patient ages and tumor sites. [Gro16].

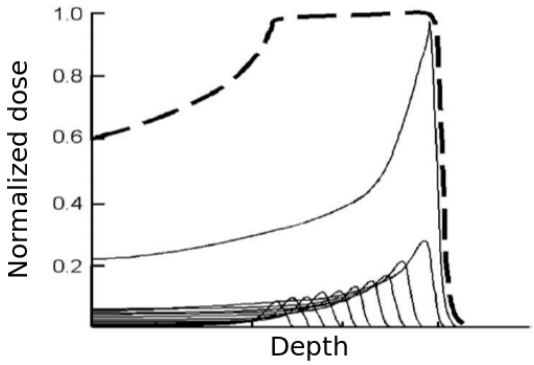

Figure 1.2: *Spread-Out Bragg peak (dashed line) composed by composed a number of BP with different energies. Adapted from [SEJS06].*

1.2 Rational of charged particles

The rationale of using charged particles in radiotherapy is related to the physical processes these undergo (the physical rationale) and to the reactions (and its consequences) that occur at a cellular level after irradiation with a charged particle beam (radiobiological rationale). In this section the physical and the biological rationale of using charged particles is summarized.

1.2.1 Charged particles physical rational

While charged particles travel through matter, they transfer energy to the medium due to atomic and nuclear interactions. This energy transfer is approximately inversely proportional to the square of their velocity [Tur07]. As they start slowing down, the probability of interaction

increases. As a result of the accumulation of interactions, the particles stop and transfer the rest of their energy to the medium. This typical energy loss leads to a depth-dose curve with a sharp increase of dose at a well-defined depth (BP) and a rapid dose falloff beyond that maximum (Figure1.1). By positioning the BP in the tumor it is possible to deliver a therapeutic dose while sparing the surrounding tissues as shown in (Figure1.3).

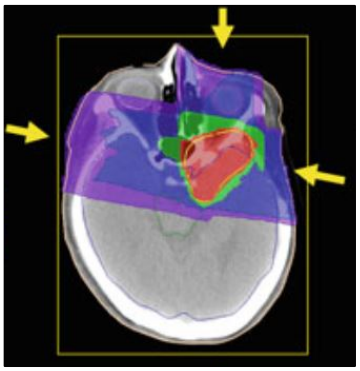

Figure 1.3: *The dose distribution of using three direction carbon ion beams. Carbon ion beams can produce a conformal dose distribution and steeper dose gradients without an increase in the normal tissue integral dose and with a small number of beams. Figure adapted from [TKSN14].*

The depth and magnitude of the BP in a determined medium can be determined by the Bethe-Bloch equation (equation 1.1) also known as the Stopping Power (SP) of a charged particle. This gives the mean rate of energy loss (or stopping power) of a charged particle along its path. The stopping power of a charged particle can be defined as:

$$\frac{\partial E}{\partial x} = \rho \frac{k}{\beta^2} z^2 \frac{Z_t}{A_t} \left\{ ln\left(\frac{2m_e c^2 \beta^2}{1-\beta^2}\right) - \beta^2 - ln(I_t) - \frac{C}{Z_t} - \frac{\delta}{2} + \Delta L \right\} \tag{1.1}$$

Where z, β^2, are the atomic charge and velocity of the projectile. k is a constant, ρ, A_t and Z_t are the density, relative atomic mass and number of the target atom. I_t is the mean ionization energy of the target, also known as the I-value. ΔL is inserted in the stopping power equation to account other corrections, such as Bloch, Mott and Barkas corrections. According to ICRU49 [ICR93], these corrections are only

important for low projectile velocities. The I-value, the shell term correction term (C/Z) and the density correction ($\delta/2$) only depend on the target, therefore they are assumed to be the same for heavy (carbons) and lighter (helium and protons) charged particles. However, in section 2.1 and chapter 4 it will be shown the impact of the different correction in the determination of charged particles range and the differences in using helium SP to determine carbon range.

Even though the depth dose distribution of charged particles is well defined by the Bethe-Bloch formula, the penetration of a charged particle into a medium is governed by stochastic interactions which cause energy loss and changes of direction. Each type of possible interaction has associated a cross-section value which defines the probability at each collision that a given type of interaction will occur. Charged particles are mainly affected by two electromagnetic processes: inelastic collisions with atomic electrons of the medium and elastic scattering from nuclei. The cumulative result of these two processes will lead to the energy loss and deflection of charged particles. Other processes through which charged particles can lose energy are: emission of Cherenkov radiation, nuclear reactions and Bremsstrahlung. However, in comparison with the atomic collision processes they are extremely rare. The Bethe-Bloch equation only accounts for inelastic electromagnetic processes, *i.e.*, soft and hard collisions as will be next explained.

1.2.1.1 Inelastic collisions

Inelastic collisions are the principal process of energy loss for charged particles in matter. In these collisions, the kinetic energy of the incident particle is not conserved, it is transferred from the incident particle to the atom causing ionization or excitation of the latter. The energy transferred in each collision is only a minute fraction of the incident particle's kinetic energy, although in dense matter, the number of collision per unit path length is large leading to a considerable energy loss.

Inelastic collisions are caused by the Coulomb-force. Coulomb-force

interactions can be characterized in terms of the relative size of the classical impact parameter b vs the atomic radius a, as show in Figure 1.4.

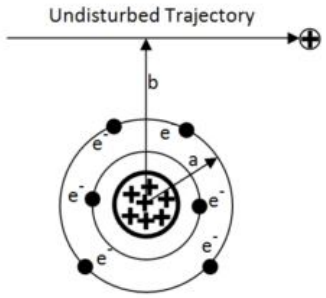

Figure 1.4: *Representation of an atom, the impact parameter (b) and the classical atomic radius.*

These atomic collisions can be divided into two groups: Coulomb interactions (soft collisions ($b >> a$) and hard collisions ($b \approx a$)) and nuclear interactions.

In soft collisions (for $b >> a$ in Figure 1.4)), the charged particle passes at a considerable distance from the atom. Due to the particle's Coulomb force, the atom is affected as a whole and it is excited to a higher energy level. Sometimes, it ejects a valence shell electron and becomes ionized. In soft collision a small amount of energy (a few eV) is transferred to the atom of the absorbing medium [Att91]. Large values of b are very probable so soft collisions are by far the most numerous type of charged-particle interaction.

If the impact parameter, b, is of the order of the atomic radius, a, there is a high probability that the incident particle will interact with an atomic electron, which is then ejected from the atom (leaving it ionized) with considerable kinetic energy. This electron is known as delta, δ-ray, which can causes secondary ionizations. This interaction is known as hard collision and its probability of happening is smaller than soft collision.

In addition to Coulomb interactions with atomic nuclei, charged particles can also suffer nuclear interactions with the nucleon via the so called strong nucleon-nucleon force. A charged particle having sufficiently high energy (near 100 MeV/u) and an impact parameter less than the nuclear radius may interact inelastically with the nucleus [Att91]. In these collisions, the nucleus is broken apart and the incident particle loses a significant fraction of its energy and is usually deflected by several degrees. The nucleus disintegrates and emits secondary particles (mostly nucleons of relatively low energy and γ-rays).

Nuclear interactions lead to a reduction of the incident beam fluence (ϕ) with increasing thickness (x) of the traversed object. This can be computed by:

$$\phi(x) = \phi_0 \cdot e^{-N\sigma_r x} \tag{1.2}$$

where ϕ_0 is the initial beam fluence of the primary particles, N is the density of nuclei target material, σ_r the total reaction cross section.

Besides decreasing the beam fluence, nuclear interactions produce a halo of scattered primary charged particles and knocked-out secondaries that travel long distances. This halo leads to a "tail" to the lateral dose profile of a beam. Nuclear interactions are also responsible for a halo of neutrons that escapes the patient and for a small contribution to the dose inside and outside the primary radiation field. Finally, these create heavily ionizing fragments, which deposit their dose very close to the point of interactions, increasing the RBE.

It is important to mention that there are also elastic nuclear collisions in which the nucleus is left intact but the incident charged particle loses a significant fraction of its energy and is usually deflected by several degrees.

1.2.1.2 Elastic collisions - Multiple Coulomb Scattering

In elastic collisions the amount of energy transferred to the medium is less than the smallest energy difference of the atomic or molecular levels, being the energy and momentum of the incident charged particle conserved.

Charged particles are much heavier than electrons and are hardly deflected by Coulomb interactions with atomic electrons. However, they also experience a repulsive force when they pass close to a positively charged nucleus of an atom. Due to this repulsive force, charged particles can be deflected through large angles. The incident particles suffer many of these interactions resulting in a net angular and radial deviation. This important phenomenon is known as Multiple Coulomb Scattering (MCS) [Goi08].

MCS is the physical process that most contributes to deflections in charged particle's direction as they cross matter without changing their total momentum. The Coulomb scattering distribution is well represented by Moliére's theory [Mol47]. It is a statistical process involving the sum of many individual elastic interactions between a charged particle and the nuclei of the matter traversed. For small angle deflections the scattering can be approximated to a Gaussian distribution, but for larger angles it behaves like a Rutherford scattering, having larger tails than does a Gaussian distribution [Wil04a]. For most applications, it is sufficient to assume a Gaussian approximation whose width, σ_θ, can be determined by [Eid04]:

$$\sigma_\theta = \frac{13.6\,\text{MeV}}{\beta cp} z\sqrt{x/X_0}\,[1 + 0.038\,ln(x/X_0)] \tag{1.3}$$

Here p, βc, and z are the momentum, velocity, and charge number of the incident particle, and x/X_0 is the thickness of the scattering medium in radiation lengths.

MCS also tends to affect the particles trajectory as shown in Figure 1.4. The distribution of displacements y is also fairly Gaussian, whose

width, σ_y, is proportional to the distance x traversed by the particle and to σ_θ [Wil04a]:

$$\sigma_y = \frac{1}{\sqrt{3}} x \sigma_\theta \tag{1.4}$$

The presence of MCS greatly contributes to uncertainties in predicting a charged particle's path. Different path estimates have been proposed to account the MCS effect. The Most Likely Path (MLP) proposed by [SP94] was the first attempt to model protons trajectories considering the effect of MCS. Others MLP formalism have followed [Wil04a, SPTS08], all considering the statistical behavior of MCS and using proton coordinates and angles to determine the statistical estimate of their trajectory. All of these studies showed that even though the MLP is the most accurate path it requires a certain amount of computational effort, slowing down reconstructions algorithms. Given this, Li *et al.* [LLS$^+$06] proposed a Cubic Spline Path (CSP) to model proton trajectories and to be used in a Algebraic Reconstruction Technique (ART) for proton computed tomography (p-CT). Results with the CSP were an improvement over the Straight Line Path (SLP) approximation providing images with the same spatial resolution as the MLP. Also the CSP is mathematically simpler than the MLP, requiring less computer power. In section 2.2, the role CSP in determining carbons and protons paths will be shown. Results led to the formulation of a phenomenological method, which provides an improvement in the CSP approximation for the path [FCDD$^+$15b].

1.2.1.3 Range/Energy straggling

When traversing an object of certain thickness and density, monoenergetic charged particles experience a varying numbers of collisions. Statistical fluctuations occur along the traveled path due to the random distribution of atoms and due to the stochastic behavior that a certain interaction can occur. Therefore, not all the particles undergo the same number of collisions leading to different energy loss, which also affect the beam range. This effect is known as energy loss/range straggling.

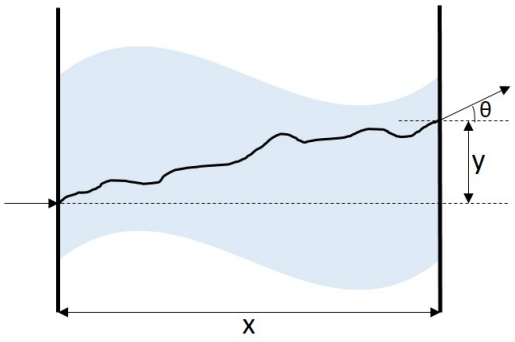

Figure 1.5: *Diagram illustrating the scattering of a charged particle through a material of thickness x resulting in a deflection of y and a scattering angle of θ (in one plane).*

This phenomenon leads to a broadening of the measured BP and it depends on the mass of the projectile and on the penetration depth in a given material. For different ion species range straggling varies approximately with the inverse of the square root of the charged particle mass [SESE10].

All these physical phenomenons contribute for the typical depth-dose distribution which is one of the main reasons why charged particles have been used to deliver high dose to tumors.

1.2.2 Radiobiological Rationale

When interacting with matter, radiation can damage tissues by direct or indirect action (Figure 1.6). In direct action, the Deoxyribonucleic Acid (DNA) molecules are directly ionized, being therefore damaged by the ionizing particles [Cre05]. Since DNA is found in almost all the cell and it is responsible for the function that each cell performs, the damage made in the DNA either kills the cell or turns it into a different kind [sit12]. In indirect action, the radiation interacts with other molecules and atoms, mainly water, within the cell producing free radicals that can damage the DNA cells. However, to make the DNA damage permanent, further reaction with oxygen is required to prevent the DNA to repair itself [OzR12].

The effect of radiation in oxygenated and hypoxic tumors can be mod-

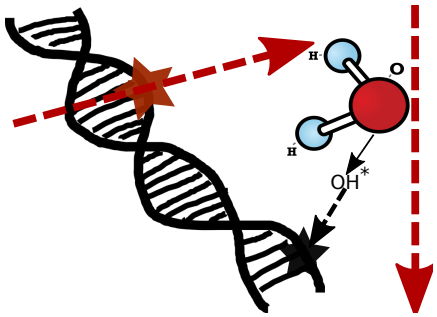

Figure 1.6: *Direct and indirect (via diffusion of free radicals) radiation effects on the DNA. The dashed red lines show two potential particle paths leading to the two interaction types (direct with the DNA and indirect by interacting with water).*

eled through the Oxygen Enhancement Ratio (OER) concept. The OER of radiation is given by the ratio between the dose required to produce a certain biological effect in the absence of oxygen and the dose required to produce the same effect in the presence of oxygen [Lin12]. As one can see in Figure 1.7, for carbon ions the survival curves in air (oxygenated environment) and nitrogen atmosphere (hypoxic environment) do not differ much (low OER). For X-rays these are quite different, showing that when X-rays are used the survival rate in nitrogen is smaller than for air. The reason behind this fact is because carbon ions are considered to be high-LET particles while X-rays low-LET.

The LET is a measurement of the energy that is transferred by an ionizing particle to the medium where it travels [Lin12]. For high-LET radiation, the DNA damage is mainly caused by direct action. Whilst for low-LET radiation (like X-rays, protons, and helium) about two-thirds of the damage is caused by indirect action. It is due to this factor that high-LET radiation presents smaller OER. This reduction in OER and the fact that high-LET particles produce greater damage to cells than low-LET particles, have become one of the main reasons behind to use high-LET radiation in cancer therapy [Lin12].

As it is possible to see in Figure 1.7, the fraction of cells surviving a particular dose of X-rays (D_{photon}) is larger than the fraction of cells surviving the same dose of charged particles ($D_{particle}$) [HKM11]. This means that charged particles are biologically more effective than

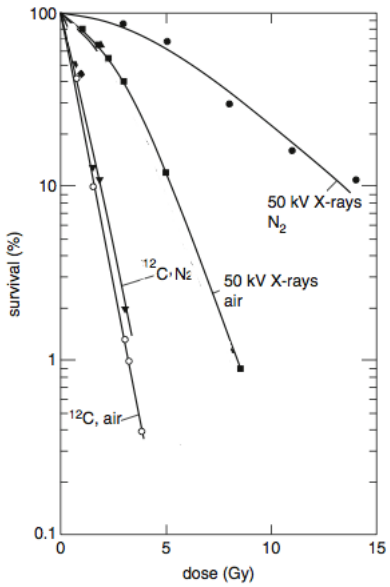

Figure 1.7: *Cell survival curves of human kidney T1 cells after irradiation with ions or X-rays in air or nitrogen atmosphere, respectively. Figure adapted from [Lin12].*

X-rays, being necessary a lower dose to achieve the same biological effect [SEJS06]. Therefore, a parameter which compares the biological effectiveness of charged particles to photons called RBE was defined. The RBE can be written as [HKM11]:

$$RBE = \frac{D_{photon}}{D_{particle}} \tag{1.5}$$

The RBE depends on the type of particle (underlying LET), cell type and delivered dose. For proton therapy, the generic RBE of protons is 1.1, however due to the dependency on the aforementioned parameters, this value can vary by about 10% to 20% [PG00]. The dependence on the various physical and biological properties of RBE for heavy ions (such as carbons) is much stronger than for protons. They show diverse RBEs as they travel through matter. Under specific conditions the RBE can be approximated to be only a function of depth [SEJS06].

1.3 Clinical charged particle beams

After the extraction of the beam from a particle accelerator, this is guided to the treatment room and to the patient using magnets which bend, steer

and focus the particle beam. The success of cancer treatment in radiation therapy is strongly related to the possibility of applying the beam to the target volume using multiple fields [SEJS06].

The use of a gantry which rotates around the patient offers this possibility. However, gantries for charged particles are of great size and weight. A proton gantry weights around 100 tons and has a diameter of 10 meters, whereas an isocentric gantry for carbon ions has a weight of about 600 tons and a diameter of 13 meters [Rob12]. The enormous size and weight of a gantry for heavy particles, is one of the reasons why most of the heavy-ion center do not have one. Therefore, in heavy-ion centers fixed beam lines are typically used: vertical beams, 45° beam inclination and horizontal beams. Moreover, it is possible to move the patient using special treatment chairs [GSI11].

The first center to have a heavy ion gantry was (Heidelberg Ion Therapy Center (HIT)) [KFM+10] (Figure 1.8). In beginning of 2016, The National Institute of Radiological Sciences (NIRS) and Toshiba Corporation announced the first rotating heavy ion gantry using superconducting technology. This is very promising since by using superconducting magnets it is possible to obtain a more compact, lighter rotating gantry than the typical heavy ion radiotherapy gantry [Tho16].

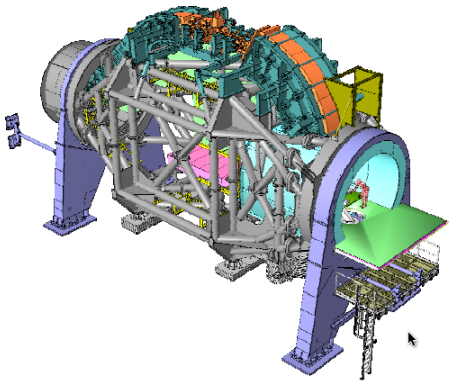

Figure 1.8: *Representation of the heavy ion gantry at HIT including echanics, beam line components and patient treatment room. Figure adapted from [WK08]*

The beam produced in the accelerator has a small diameter and small

extension of the BP in depth, being necessary to shape the beam in order to be useful for treatment. Nowadays, in charged particle therapy, there are two methods to shape the beam and thus to tailor the dose to the target volume: *passive scattering* and *active scanning* techniques [KWO07].

1.3.0.1 Passive Scattering

Passive scattering (Figure 1.9) was the first method to be developed and is still broadly used in charged particle therapy centers. In this technique a ridge filter and/or range shifters are used, which are responsible to modulate the beam to the desired radiological depth (or SOBP). These range modulators consist of a number of homogeneous plastic plates of different thickness, that can be moved into the beam.

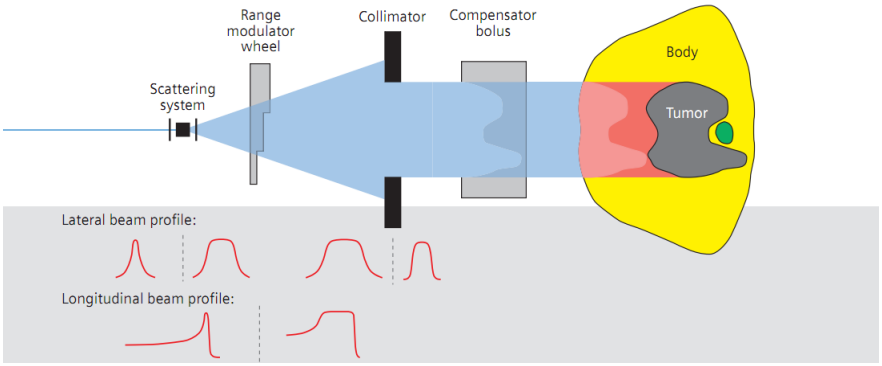

Figure 1.9: *Principle of passive scattering (upper part: schematic setup; lower part: variation of lateral and longitudinal beam profile along. Adapted from setup [Gro05].*

The lateral spread out of the beam can be produced by interposing scattering material in front of the beam [Goi08]. Furthermore, patient and beam-specific collimators are used to adapt the dose distribution the maximal lateral cross section of the target volume. Variations in depth of the distal edge of the target volume are mapped to the dose distribution by a patient and beam-specific device, the compensator. The distal edge of the dose distribution can be adapted very precisely to the prescribed target volume, but due to the fixed width of the SOBP, this shape is transferred to the proximal edge of the dose distribution, resulting in an unwanted irradiation of proximal normal tissue (Figure 1.9, dark red) [Gro05].

Instead of using a scattering system for the lateral spread of the beam, it is possible to use fast, continuous magnetic deflection (wobbling), that move the beam over a defined area (Figure 1.10) [SEJS06].

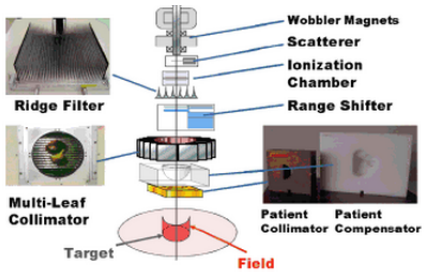

Figure 1.10: *Principle of passive shaping with wobbling system. Figure adapted from [CC09].*

Whilst passive scattering has proved to be robust, there are some important disadvantages: the cumbersome use of patient-specific collimators and compensators, the significant beam energy and intensity losses, the contamination in the beam by fragments, and neutron production in the scattering material, leading to an unnecessary neutron dose [KWO07].

1.3.0.2 Active Scanning

In *active scanning* (Figure 1.11) there are two dipole magnets connected in series which steer the narrow pencil beams in the lateral plane while the range is modulated by controlling the beam energy [Goi08]. This minimizes the equipment required and automates the treatment delivery process by a control system [KWO07].

The target volume is virtually divided into slices of constant particle range (and energy), the so-called isoenergy slices. Each of these slices is further divided into single picture elements (pixels or spots). The beam is then steered over each slice in a way that a pre-calculated number of particles is deposited to every spot assigned by the treatment plan [Gro05].

Active scanning can be divided into two categories: *Discrete* or *spot scan*, where the beam is turned off during the scanning between consec-

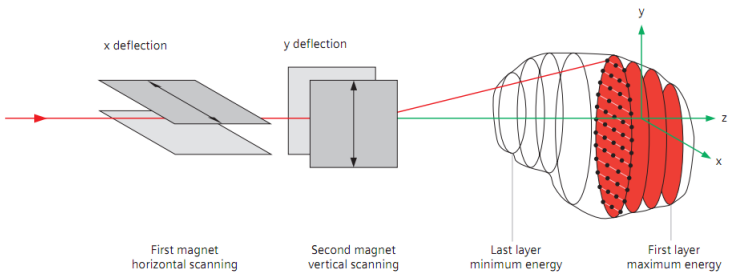

Figure 1.11: *Principle of active beam scanning. Figure adapted form [Gro05].*

utive spots, and *raster* or *quasidiscrete scan* where instead of turning off the beam between consecutive spots, this is only turned off when a slice is finished and a new energy is set [KWO07].

In *Active Scanning* the dose distribution is delivered by placing the Bragg peak in the patient one location at a time and then one layer at a time by varying the beam energy, thus allowing the use of IMPT. With IMPT the uniform dose distribution over the target volume is constructed only by the combination of two or more treatment fields (different irradiation angles). Each individual field can deliver a highly inhomogeneous dose distribution to the target, but when combined lead to a uniform dose over the target [Pag12b]. In F. Dias *et al.* [DRS+15] it has been shown that the path the beam follows during the scanning affects the dose delivered to the patient and should be taken into account.

1.4 Different charged particles and photons in cancer therapy

Nowadays, the most commonly employed radiotherapy treatment uses high-energy X-rays (*i.e.*, photons), which are generated outside the patient. In opposition to charged particles, photons do not present mass and the way they interact with matter is different. Therefore, their depth dose distribution is different and cannot be computed using the Bethe-Bloch equation (equation 1.1). Figure 1.1 shows the depth-dose distribution curves of photons, carbons and protons.

For photons the maximum of the deposited dose is located at a smaller

penetration depth than for the other particles. After its maximum, the dose decreases slowly with respect to the penetration depth. Irradiating tumors deeply located in the body while preserving simultaneously the surrounding tissues is difficult when using photons, being necessary in most situations to irradiate tumors at different angles. For charged particles, due to the BP it is possible to deliver a high dose to the tumor sparing the surrounding tissues (Figure 1.1) with a single beam. Another difference between photons and charged particles was already mentioned in section 1.2.2. The RBE of photons is smaller than charged particles (RBE=1.1 for protons and RBE>=1 for carbons). This means that more dose is necessary to deliver to the tumor when photons are used than when charged particles are used.

Even though protons are charged particles, these differ from carbons in many ways. Protons (atomic mass of 1u) are much lighter than carbons (atomic mass of 12u) and have a smaller atomic number (Z=1, for protons and Z=6, for carbons). Both carbons and protons can undergo through the different physical interactions with matter (section 1.2.1), however due to the different mass and atomic number, they present different probabilities for the different interactions. Consequently, this leads to differences in their depth-dose distribution as it is possible to see in Figure 1.1. As mentioned in section 1.2.1, range/energy straggling is proportional to the inverse of the square root of the particle's mass. Because of straggling, the width of the Bragg peak is larger for protons than for carbons (Figure 1.1). Moreover, due to the mass difference between carbons and protons, the later suffer more MCS. This effect is roughly proportional to $Z/(A \times v^2)$. In Figure 1.12 it is shown the lateral scattering suffered by protons and carbons in a clinical like environment. As one can see carbons have an almost straight path trajectory as it will be shown in section 2.2. This lateral scattering also contributes to the broadening of a proton beam in about 3.5 times larger than for a carbon beam [WK09].

A major drawback of carbons is their higher probability to suffer nuclear reactions and nuclear fragmentation. In addition to contribute to a

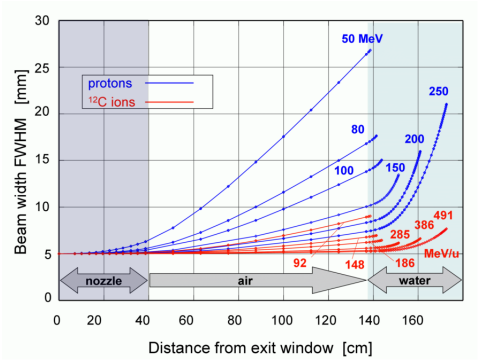

Figure 1.12: *Lateral scattering in realist scanning therapy setups. Figure adapted from [WK09].*

reduction of the incident beam fluence (section 1.2.1), these create lighter ions which will create a tail after the Bragg peak in the dose distribution of carbons. However, for carbon ions, the contribution of produced fragments does not deteriorate the dose distribution in general. It actually allows monitoring the beam inside the patient by Positron Emission Tomography (PET). This is related with the fact that the fragmentation process produces lighter carbon isotopes that are positron emitters (section 1.6.3).

Carbons and protons also have different dependencies on biological properties. Carbons show diverse RBEs as they travel through matter as mentioned in section 1.2.2. Carbon's RBE is selectively elevated in the target, and in the entrance (lower dose) has RBE values slightly higher than one [WK09]. While for protons, as previously mentioned, these have an approximately constant RBE=1.1.

Currently, there has been an increase interest in using helium beams (α particles) in clinical environment for tumor irradiation. αs, in comparison to protons, have smaller lateral scattering and when compared to carbon ions, they have a reduced fragmentation tail [MMD+16]. These advantages led to the idea of using α radiography in the determination of the carbon's range (chapter 4).

The physical and biological differences between the different particles

also lead to differences in treatment planning, production and transportation and imaging processing/reconstruction. However, describing all the differences between these particles is out of the scope of this work.

1.5 Range uncertainties in charged particle therapy

A major challenge in charged particle therapy is the uncertainty in determine precisely the range of the charged particle beam. Since it is at the end of the particle's range where the beam presents its sharpest dose gradient (Figure 1.2 and Figure 1.1), this range uncertainty can lead to an underdose of the tumor or an overdose of the surrounding tissues (Figure 1.13).

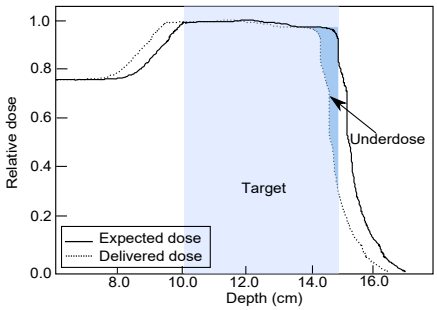

Figure 1.13: *The effect of a range undershoot on the depth-dose distribution of a proton beam in water.*

The range uncertainty can come from random sources: patient positioning, organ motion and heterogeneity, beam fluctuations [KMS+14]; and can be systematic coming from the fact treatment plan is made using computed tomography (CT).

As mentioned it will be mentioned in section 1.6.1 the energy/range necessary to irradiate the patient is computed by converting the HU from the treatment planning X-ray CT into RSP - HU-RSP calibration curve [SPL96a]. Through the RSP value, it is possible compute the beam's energy to position the BP within the tumor contour. A widely used method to determined the HU-RSP curve is the stoichiometric approach pro-

posed by Schneider *et al.* [SPL96a]. This uses experimentally obtained RSP values for plastic materials and theoretical determined RSPs for human biological tissues. Assumptions on the composition and ionization value of tissues have to be made, therefore, the stoichiometric calibration is not patient-specific.

Recent studies demonstrated that the stoichiometric method introduces large errors (up to 5%) [YZP+12] in the range estimate of the BP. The use of charged particle CT and/or radiography which employs a direct measurement of the incident charged particle stopping power, could remove this uncertainty. However, in practice the reconstruction methods struggle with uncertainty in reproducing the charged particle's path, due to MCS. The classic X-ray CT reconstruction algorithms assume a SLP which for the case of protons is not valid, leading to images with poor spatial resolution [SPH+12]. Furthermore, challenges related with detectors also contribute for images with poor resolution and noisy (mostly caused by secondary particles hitting the detector).

Using heavier particles such as carbons should reduce the effect of MCS since these travel practically straight paths as it will be shown in section 2.2. However, carbons present a large number of nuclear interactions as mentioned in section 1.2.1, making more difficult the use of single particle detectors (section 1.6.2).

Other source of range uncertainty can come from the algorithm used to compute the range and dose given to the patient. In the case of interfaces between tissues with different densities, the computation of the beams scattering is more complex. Pencil-beam dose algorithms, commonly used in clinical environment, are know to introduce uncertainties up to $\pm 2.5\%$ for specific treatment sites and beam arrangements [Pag12c].

In the clinical environment the range uncertainty is accounted by increasing the target margins up to 3.5% [Pag12c]. These can be different depending on the institution and on the treatment site. In some situations

additional margins can be added or shrunken. Even though adding margins to the treatment planning makes it more robust it comes with a cost: additional dose is delivered to the surrounding tissues.

1.6 State of the art: imaging techniques in charged therapy

As previously stated, the depth-dose distribution of charged particles allows a precise and high dose delivery to the tumor. To do so, correct knowledge of the particle's range is necessary. This section aims to explain how this is obtained currently in a clinical environment, what are the drawbacks of the current method and what are the major research tendencies to tackle such drawbacks.

1.6.1 The treatment planning computed tomography and the calibration curve

A volumetric X-ray CT image of the patient is the basis of current treatment planning in charged particle therapy which takes into account the effect of tissue inhomogeneities. A X-ray CT, without any contrast agent, measures the photon attenuation coefficient - μ_x of each tissue x. This is converted to the scale HU using the photon attenuation coefficient of water - μ_w. The scaled HU is defined by :

$$HU_x = 1000.\frac{\mu_x}{\mu_w} \tag{1.6}$$

The HU of water is normally set to zero.

The beam range required for patient treatment in charged particle therapy is calculated from the CT HU numbers, which are converted into RSP through a calibration curve. The calibration curve in most centers is obtained through the stoichiometric approach proposed by Schneider *et al.* [SPL96a]. In the stoichiometric approach both measured HU of tissue substitutes and the chemical composition of real tissues are used to predict HU for human tissues. The HU values of a number of tissue equivalent materials, whose chemical composition is known, are measured on a CT scanner. The obtained HUs are parametrize as a function

of the chemical composition, using the equation [DFCD+16]:

$$HU = \rho_e^{rel}(AZ^{3.62} + BZ^{1.86} + C) \tag{1.7}$$

where ρ_e^{rel} is the volumetric electron density relative to water; Z is the effective atomic number (calculated using the fraction by weigh of the individual elements for compounds); A,B,C are constants that characterize the contributions of photo-electric, Rayleigh scattering and Compton scattering to the total attenuation. From this parametrization the HU for human biological tissues is computed using the chemical compositions and effective densities from literature [WW86, WWH87, Wat99].

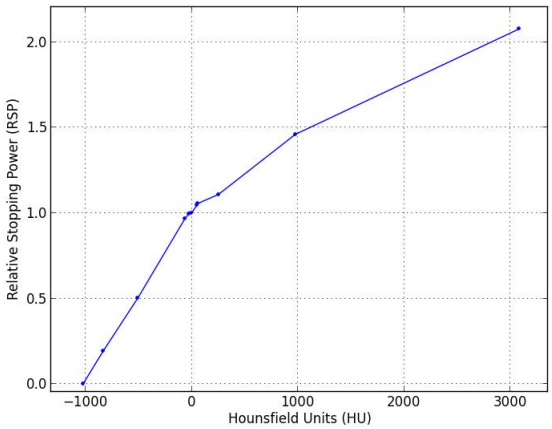

Figure 1.14: *Centro Nazionale di Adroterapia Oncologica (CNAO) calibration curve.*

The RSP of each material is then computed and may be confirmed by directly measure the energy loss of the charged particles after crossing a known material. The RSP is defined as the ratio between the tissue stopping power and the stopping power of water. These can be computed using equation 1.1. Using all of this information, the HU to RSP correlation is built and used to obtain information about all other tissues. This method is not patient-specific since it relies on plastic-tissue materials and theoretical human tissue compositions. Tissue composition can be variable leading to changes in the calibration curve. Furthermore, the stopping power equation besides depending on the density of the tissue,

depends on its I-value, which also changes according to the tissue chemical composition. In chapter 2, it will be presented a method developed by Doolan *et al.* [DFCD$^+$16] which optimizes the I-value of tissues using knowledge from experimental measurements. In chapter 4, it is proposed the use of charged particle radiography (carbon, helium and proton) to determine a patient-specific calibration curve which is able to account for chemical composition changes. Figure 1.14 shows the calibration curve used in CNAO.

It is worth to mention that the reason why in charged particle therapy is used the RSP instead of the particle's SP is because this is independent of the particle's energy (at least for the energies considered for treatment).

1.6.2 Carbon radiography and computed tomography

As mentioned in section 1.5, the stoichiometric method can introduce errors up to 5%. A possible solution to tackle this problem is to use charged particle radiography or/and charged particle CT. By using charged particles to image the patient, the process of converting HU into RSP is no longer necessary since charged particle radiography/CT allows a direct measurement of the patient RSP [FCSLJ16].

Moreover, X-ray CT is limited in density sensitivity which arises from the detection of a finite number of X-rays. An increase in the number of detected X-ray leads to higher dose delivered to the patient. Imaging with charged particles, due their dependency in the density of the medium (equation 1.1), provides an improved density resolution for a given dose [HBK$^+$82].

The first studies with charged particle radiography date from 1968 [Koe68], where it was shown that images obtained on a radiographic film from irradiating objects with a thickness slightly smaller than the range of the incident 160 MeV proton beam had a greater contrast than images produced with X-rays under the same conditions. Others produced

proton radiographs using this fluence method, however this method was limited to thin samples [SK73].

In 1972, Goitein [RS16] reconstructed CT images using data from the helium (α). The following years, research on proton radiography (p-rad) [SK73] and p-CT [CK76] addressed proton imaging as a diagnostic tool. Cormack and Koehler [CK76] used a proton-integrating system..

Hanson *et al.* [HBC$^+$78] at the Los Alamos Laboratory (Los Alamos, NM), presented pCT results of human specimens. Two varieties of detector module with very different functions were utilized: a position-sensitive detector and a residual energy-range detector. These concepts are still relevant for the design of proton imaging systems today. The former tracks each proton's position and the latter implies its residual energy or range. Figure 1.15 shows the basic concept of position-sensitive (Figure 1.15a) and residual range detector (Figure 1.15b). Nowadays, through a system that allows to obtain the incident and exit charged particle direction, position and energy, it is possible to apply path reconstruction algorithms which estimate their trajectories [FCSLJ16].

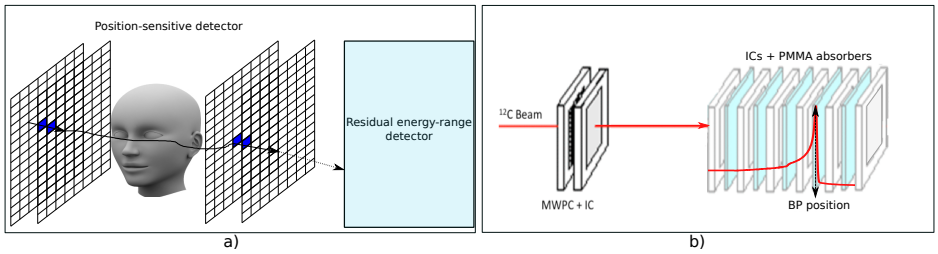

Figure 1.15: *a) A schematic of the ideal charged particle tracking radiography/CT system. It is constituted by a position-sensitive detector (four panels) placed before and after the patient, through this it is possible to retrieve information about the particles entrance and exit position/directions. The residual energy/range detector is placed after the patient and it records the residual (remaining) energy/range of the particles after crossing the patient. b)shematic representation of the range detector developed at HIT [RBG$^+$13]. The range detector is build up wtih a stack of parallel-plate Ionization Chamber (IC) interleaved with a polymethyl methacrylate (PMMA) absorber plate. This figure was adtapted from [RBG$^+$13].*

The increase interested in charged particle therapy led to the construction of a first radiographic system at PSI [PBdB$^+$99]. The system

was proton-tracking with a setup similar to the one in Figure 1.15a with a range telescope. This system was used to acquire a p-rad of a live canine subject, being the first live animal radiography [SBP+04]. The biggest disadvantage of p-rad and p-CT is the poor spatial resolution due to MCS. To improve the spatial resolution different methods have been consider in order to model proton trajectories [Wil04a, SPTS08, LLS+06, FCDD+15b, FCSLJ16]. In section 2.2 it is explained a new model for charged particle trajectories.

Even though most research on charged particle radiography/CT is performed on protons, heavy ion radiography/CT studies have also been carried out. Abe *et al.* [ASF12] proposed in 2002 a heavy ion CT system based on measurement of the residual range by a fluoroscopy detector consisting of an intensifying screen and a CCD video camera. The range information was extracted by the analysis of the transmitted signal acquired for five different thicknesses of the range shifter for each radiographic projection.

Ohno *et. al.* [OKMK04] and Shinoda *et. al.* [SKK06] used a detector system that consisted of two position-sensitive detectors, an energy detector and two gate detectors. The individual ion residual energy in combination with the position before and after the target were acquired only for those valid events which triggered a coincidence signal between the two gate scintillators (adjacent to the position sensitive detectors, PSDs). Since both, primary and fragmented secondary ions, add to the residual energy, the discrimination of their contributions to the signal was difficult, leading to noise in the collected data.

Rinaldi *et. al.* [RBG+13] proposed the use of a range telescope as an alternative detector. The Bragg peak position of a charged particle beam is determined only by primary ions and therefore no noise from secondary particles is present in the signal. Figure 1.15b shows a schematic of a range detector. The Water Equivalent Thickness (WET) of the traversed object can be deduced from the BP position using an calibration procedure [RBG+13]. Since no position sensitive detector is used, this

method relies on the scanning of the object with a mono-energetic pencil beam and that charged particles travel straight paths. In a clinical environment, one has to deal with a Gaussian-like pencil beam. Since the human body is heterogeneous, carbons from the same incident beam traverse various materials, causing range dilution effects which lead to a broadening of the BP and consequently errors in the determination of the WET. In the case of high contrast interfaces along the beam path, multiple BPs can be detected. In chapter 3 it is proposed a method where the detected multiple peaks are used to retrieve information about high contrast edges.

Other difficulties related to ion-based CT concern the financial and technical effort needed to accelerate therapeutic ion beams to a sufficiently high initial energy that allows charged particles to cross the whole object, for carbons, since these are heavier, this plays a larger effect.

1.6.3 Indirect charged particle imaging

The first *in vivo* range verification being investigated was PET imaging [MMRea69]. As mentioned in 1.4, during ion beam irradiation, positron emitters are produced along the beam path due to nuclear fragmentation. For heavy ions such as carbons, the nuclear fragmentation can happen in both the incident particles and in the target nuclei. For a proton beam only target fragmentation is possible [ZE13].

A PET scanner detects the coincident γ-rays that are emitted when the positrons annihilate. These can be detected in a patient either during (on-line) or after (shortly after: in-room, with greater delay: off-line) treatment [Rin11]. The tomographic reconstruction provides a three-dimensional distribution of the positron emission, which is correlated to the delivered dose. So far, PET is the only method clinically implemented for *in-vivo* range verification. However, it has major drawbacks, such as the intrinsically low signal and the biological washout, depending on the time elapsed between irradiation and imaging. These will contribute for a blurred and limited precision on the PET measure-

ments [Par14].

Alternative or complementary solutions to PET and charged particle radiography/CT, which use charged particles, are being explored. Such is the case of prompt γ, which consists in the detection of γ-rays that are emitted due to particle-nuclear interactions. Experiments have shown that there is a correlation between the charged particle range and the prompt γ emissions [MKYK06]. A major drawback of this method is related with the detection of the γ-rays because of the neutron-induced background radiation.

Other imaging method which uses charged particles is interaction vertex imaging. This consists in the detection of secondary charged particles emerging from the patient that were generated in nuclear interactions. By reconstructing the trajectories of the emerging particles, it is possible to determined their production point. The position of the fragmentation and the amount of emerging secondary particles, in principle, is correlated with the incident charged particle range and dose delivered [HTC$^+$12].

More recently, the use of the acoustic signature of a proton beam has been studied for range verification in proton therapy [JWSA14]. Pulsed proton beams can create a measurable acoustic signal. The energy deposition of the pulsed proton beam leads to a local heating of the medium which creates sound waves that can be measured by a ultrasound equipment. This method offers a direct relation between the dose, *i.e.* energy deposition and the signal. However, is not compatible with common proton acceleration methods [Ver15].

1.6.4 Other imaging modalities

Besides the treatment planning CT, which uses X-rays, all the aforementioned imaging modalities involve shooting the patient with charged particles. Other imaging modalities have been proposed to be used for treatment planning in carbon/proton therapy, such as magnetic resonance imaging (MRI) and dual-energy computed tomography (DECT).

The main advantage of using MRI is the better spatial resolution and improved signal-to-noise ratio. The use of MRI in proton therapy has been investigated as alternative to the planning CT [KWK16]. The method relies on conversion of MRI intensity values to HU. Even though the method demonstrates good agreement with the planning CT, the aforementioned range errors due to calibration procedure will still exist. Other method which relies on MRI has been investigated which consists in the evaluation of the range of the beam by analyzing changes in the tissue that occur on a molecular level following proton irradiation [GYL+10]. This method is limited by the fact that it relies on effects which occur on longer time scales and by the fact that the biological effects and difference between patients are not fully understood.

The interest in using DECT has been growing over the past years. DECT uses two different X-ray spectra, allowing the calculation of the electron density and atomic number of the materials. Yang *et al.* [YVC+10] showed that this could be used for stopping power calculations (with range uncertainties of 1.9%-2.3% [YVC+10]). A major drawback about DECT is that it does not image the patient directly in the treatment position, and does not account for morphology change that might occur between planning and treatment.

CHAPTER 2

The impact of charged particles path and the ionization value in their range

As stated in the previous chapter, the finite range of charged particles, which allows a high dose delivery, represents one of the main reasons why these are used for cancer therapy. However, there is still a large number of uncertainties in determining their range inside the patient (section1.5). One of these major uncertainties is related with the fact that charged particles range is determined from X-ray CT through a calibration procedure which converts HU into RSP (section 1.6.1).

The accuracy of the RSP calculation depends on the uncertainty in the real tissue composition, deviations of the patient from the literature compositions and uncertainties in the mean ionization energies (I-value) of tissue and water. In order to avoid this calibration procedure, charged particle radiography/CT has been proposed (section 1.6.2). However, problems due to spatial resolution are still needed to be dealt with. Charged particles do not present SLP trajectories and such assumption may lead to low spatial resolution and errors in the determination of

the RSP values.

In this chapter it will first shown the effect of the I-value in the RSP calculation followed by the impact of using different path formalism in the prediction of charged particle's trajectories.

The work here presented is based on the results and contribution made to the following work:

- **Inter-comparison of relative stopping power estimation models for proton therapy**, P. J. Doolan, Charles-Antoine Collins-Fekete, Marta F. Dias, Thomas A. Ruggieri, Derek D'Souza and Joao Seco. Phys. Med. Biol., 2016 [DFCD$^+$16].
- **Developing a phenomenological model of the proton trajectory within a heterogeneous medium required for proton imaging**, Charles-Antoine Collins-Fekete, Paul Doolan, Marta F. Dias, Luc Beaulieu and Joao Seco. Phys. Med. Biol., 2015 [FCDD$^+$15b].
- **TU-F-CAMPUS-J-02: Developing a Phenomenological Model of the Proton Trajectory Within a Heterogeneous Medium Required for Proton Imaging**, Charles Antoine Collins-Fekete, Paul Doolan, Marta F. Dias, Luc Beaulieu and Joao Seco. Med. Phys.,2015 [FCDD$^+$15a].
- **SU-E-T-550: Range Effects in Proton Therapy Caused by Systematic Errors in the Stoichiometric Calibration**, Paul Doolan, Marta F. Dias, Charles-Antoine Collins Fekete, Joao Seco. Med. Phys, 2014 [DDFS14].

2.1 Ionization value and the impact on the relative stopping powers

The stoichiometric method by Schneider [SPL96a] is the most widely used method for producing the HU-RSP calibration curve [Tay15]. As explained in chapter 1, section 1.6.1 the RSP is the ratio between the tissue SP and water SP. The Bethe-Bloch formula is used to compute

the SP (equation 1.1, section 1.2.1), however, this can be written using different correction terms. The equation presented in section 1.2.1 in chapter 1, without the correction term ΔL, was first proposed by Bichsel [Bic72]. This can be re-written as the multiplication of two terms, K and B:

$$\begin{aligned} S_B &= K \times B \\ K &= \rho \frac{k}{\beta^2} z^2 \frac{Z_t}{A_t} \\ B &= ln\left(\frac{2m_e c^2 \beta^2}{1-\beta^2}\right) - \beta^2 - ln(I_t) - \frac{C}{Z_t} - \frac{\delta}{2} \end{aligned} \tag{2.1}$$

All the parameters have been defined in chapter 1, section 1.2.1.

Janni [Jan82] proposed that the stopping power, S_J, should contain some corrections. So, the Bethe-Bloch formula proposed by Janni was:

$$\begin{aligned} S_J &= K\left\{B + J_1 + J_2 + J_3\right\} \\ J_1 &= -\frac{1}{2} ln\left(1 + \frac{2m_e}{M\sqrt{1-\beta^2}} + \left(\frac{m_e}{M}\right)^2\right) \\ J_2 &= \frac{\pi \alpha z \beta}{2} \\ J_3 &= \frac{z Z_t \alpha^3 F(\beta, Z_t)}{\beta^3} \end{aligned} \tag{2.2}$$

where M is the charged particle's rest mass, J_1 accounts for the maximum kinetic energy that can be transferred to an unbound electron at rest; α is the fine structure constant and it is equal to 1/137.036. J_2 is only relevant at relativistic energies and J_3 is the Barkas correction, where the function $F(\beta, Z_t)$ is only important at low energies and usually is set to zero.

Other SP formulation is the one defined by ICRU Report 49 [ICR93] which can be written as:

$$S_I = K \left\{ B + J_1 + \gamma J_3 - \left(\frac{z\alpha}{\beta}\right)^2 \sum_{n=1}^{\infty} \left[n \left(n^2 + \left(\frac{z\alpha}{\beta}\right)^2 \right) \right]^{-1} \right\} \tag{2.3}$$

The parameter γ comes from the free-electron model and is approximately equal to $\sqrt{2}$. The new term in the expression is the Bloch correction.

Since the SP can be computed differently, different RSP formulations arise (equation 2.1, 2.2 and 2.3). However, the most popular approach to compute the RSP ignores most of the correction terms due to the fact that these are considered to be negligible for biological tissues [ÖZB+15]. This formulation was first used by Schneider [SPL96a]:

$$RSP = \rho_e^{rel} \frac{ln[(2m_e c^2)\beta^2/(I_t(1-\beta^2))] - \beta^2}{ln[(2m_e c^2\beta^2)/(I_w(1-\beta^2))] - \beta^2} \tag{2.4}$$

where ρ_e^{rel} is the volumetric electron density relative to water and I_w is the I-value of water.

Each formulation incorporates different corrections and as a result each uses different I-values. The aim of the work by Doolan *et al.* [DFCD+16] was to show the impact of using the different methods to compute the SP and the different sources of I-values on the RSP calculation. To do so, the RSP of different materials from a Gammex phantom were experimentally measured and compared with the ones calculated from the different formulations. Finally, it was proposed an optimization method which recomputed the I-value of the elements so that the measured and computed RSPs matched.

2.1.1 Materials and Methods

The RSP and HU values of twelve tissue substitutes from the Gammex RMI 467 phantom (Gammex Inc. Middleton, WI) were experimentally obtained. Details of the experimental setup can be seen in Doolan *et*

Table 2.1: *I-values of elements and water using different sources: Bichsel [Bic72], Janni [Jan82] and ICRU [ICR93].*

	I-value (eV)		
Element (Z) / Material	Bichsel [Bic72]	Janni [Jan82]	ICRU [ICR93]
H (1)	19.2	20.4	19.2±0.4
C (6)	86.9	73.8	81±7
N (7)	80	97.8	82±2
O (8)	95	115.7	106±2
F (9)	119	124.8	112±0
Na (11)	148	143.0	168.4±0
Mg (12)	156	151.1	176.3±0
Si (14)	17	174.5	195.5±3
P (15)	172	179.1	195.5±0
S (16)	180	183.6	203.4±0
Cl (17)	187	182.6	180±0
K (19)	193	186.8	214.7±0
Ca (20)	196	191.9	215.8±8
Fe (26)	293	278.2	323.2±9
I (53)	510	515.2	535.6±0
Water	79.7	81.8	75.3

al. [DFCD$^+$16].

Using the chemical composition from the Gammex RMI vendors the theoretical RSP was computed using the different SP formulations (equation 2.1, 2.2 and 2.3) and their I-values (Table 2.1). Using the experimentally obtained HU, the HU-RSP calibration curve was derived for each formulation. These calibration curves will be referred to as the "Bichsel", "Janni" and "ICRU" for the remainder of this work.

The I-value for compounds can be computed using the Bragg's additivity rule [ICR92]:

$$lnI_t = \left(\sum \frac{w_i Z_i}{A_i} lnI_i\right) \left(\sum \frac{w_i Z_i}{A_i}\right)^{-1} \tag{2.5}$$

where I_i are the individual elemental I-value; Z_i and A_i the atomic number and atomic weight of the ith element and w_i is its proportion by weight.

Using the I-values from the different sources (table 2.1), the RSPs for the Gammex tissues were also computed using Schneider RSP computation (equation 2.4).

All of the computed RSP values were compared to the experimental ones. Using Schneider's formulation (equation 2.4), it was used an optimization method in which elemental I-values were modified until the theoretical RSP computations matched the experimental RSP. The cost function, Δ, of the optimization method was:

$$\Delta = \frac{1}{n}\sqrt{\frac{\sum_i (RSP_c^i - RSP_m^i)^2}{\sum_i (RSP_m^i)^2}\frac{1}{(Err_m^i)^2}} \tag{2.6}$$

where n is the number of tissues, RSP_c^i and RSP_m^i are the computed and measured RSPs for the tissue i and Err_m^i is the uncertainty of the experimental RSPs. The optimization was performed using the Nelder-Mead optimization function from Matlab [TMI00].

In order to assess the impact of the optimization of the elemental I-values, the RSPs of 72 human tissues were computed using the Schneider formulation with the optimized I-values. These were then compared with the Bichsel, Janni and ICRU formulations whose I-values were not optimized. The human tissue composition was obtained from [WW86, WWH87, ICR89].

2.1.2 Results and Discussion

Table 2.2 shows RSP relative errors obtained by calculating the RSP values using the different formulations. Figure 2.1, shows the calibration curve and relative errors obtained for the RSPs computed with the optimized I-values. The experimental RSP were used as reference.

Using the three different theoretical SP formulations (equation 2.1,2.2 and 2.3), the RSPs for the different Gammex tissue substitutes were computed. The RSPs were computed over the energy range 10-330 MeV and averaged. By analyzing the results in table 2.2, one can infer that the

Table 2.2: *The relative stopping powers (RSPs) for the Gammex tissue substitutes calculated using the Bichsel, Janni, ICRU and Schneider formulations. The Schneider formulation was computed using the I-values from the different sources. The RMSE is the root mean square error.*

					Schneider formulation		
Material	Measured	Bichsel (%)	Janni (%)	ICRU (%)	Bichsel (%)	Janni (%)	ICRU (%)
LN-300 lung	0.280	-1.74	-0.82	-2.37	-2.30	+0.23	-1.21
LN-450 lung	0.473	-2.33	-1.42	-2.96	-3.17	-0.66	-2.09
Adipose	0.946	-0.34	+0.81	-0.69	-2.05	+0.70	-0.69
Breast	0.974	+0.10	+1.19	-0.30	-1.71	+0.98	-0.39
CT solid water	1.005	-0.42	+0.58	-0.88	-2.17	+0.43	-0.91
Brain	1.067	+0.92	+2.10	+0.58	-1.00	+1.78	+0.39
Liver	1.080	-0.70	+0.28	-1.16	-2.50	+0.09	-1.25
Inner bone	1.094	-0.16	+0.57	-0.89	-1.75	+0.61	-0.73
CB2-30% $CaCO_3$	1.260	+1.21	+1.88	+0.45	-0.49	+1.83	+0.51
CB2-50% $CaCO_3$	1.433	+0.74	+1.08	-0.31	-0.73	+1.28	0.00
Cortical bone	1.620	+1.47	+1.50	+0.15	+0.06	+1.82	+0.57
RMSE		+1.14	+1.24	+1.30	+1.86	+1.13	+0.96
Mean error		-0.12	+0.71	-0.76	-1.62	+0.83	-0.53
Max error		-2.33	+2.10	-2.96	-3.17	+1.83	-2.09

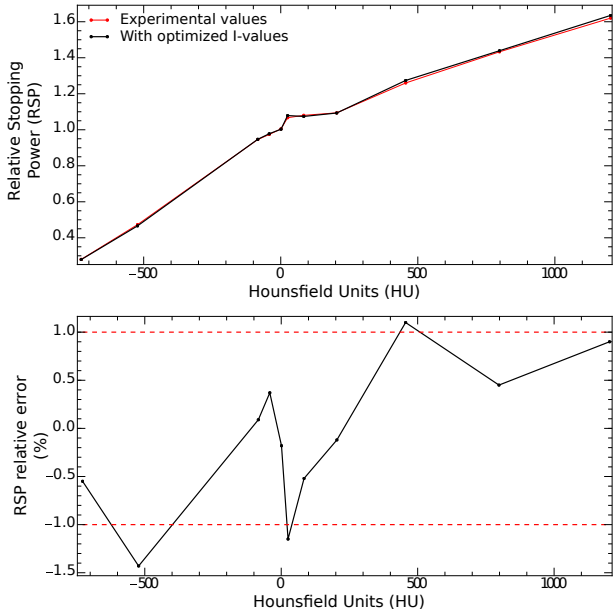

Figure 2.1: *Calibration curve (top) and relative errors (bottom) from the RSPs computed with the optimized I-values with the measured RSPs. The red dashed lines in the bottom graph represent 1% error.*

Bichsel and ICRU approaches generally underestimated the RSPs, while Janni overestimated them.

Using the I-values from the three sources (Bichsel, Janni and ICRU), but with the Schneider approximation for the RSP (equation 2.4), the results were similar to the previous ones: a systematic underestimation in the Bichsel and ICRU approaches and an overestimation in the Janni. The errors using Schneider calculation method were generally larger than using the theoretical formulae (equation 2.1,2.2 and 2.3). This was expected since the I-values from each source account for correction terms that are not present in the Schneider approach.

The optimization of the elemental I-values significantly improved the estimates of tissue substitute RSP (Figure 2.1). The maximum errors decreased and the mean error was of +0.11%.

The largest errors in overall results were typically found in the lower density lung inserts (underestimations of more than 3%). In clinical environment these errors can translate into proton range errors, particularly critical in regions such as the lung as it was shown by Seco *et al.* [SPW$^+$12]. The optimization of the I-values was able to reduce RSP uncertainties to under 1.5%.

To assess the potential impact of using the Bichsel, Janni and ICRU I-values on proton therapy patients, comparisons were made with the optimized I-values across a range of human tissues. Figure 2.2 shows the mean/max differences across 72 human tissues. For Bichsel these were: -0.5%/-1.7%; for Janni: +0.4%/+1.1% and -0.1%/-0.4% for ICRU I-values. The largest differences were found in the bony and fatty regions (+1.1 for Janni in the Skeleton Cranium, -1.7% for Bichsel in adipose tissue 3, for example), which could be a concern for particular treatment sites.

All the obtained results suggest that an additional step should be added to the stoichiometric calibration procedure, in which RSP values are

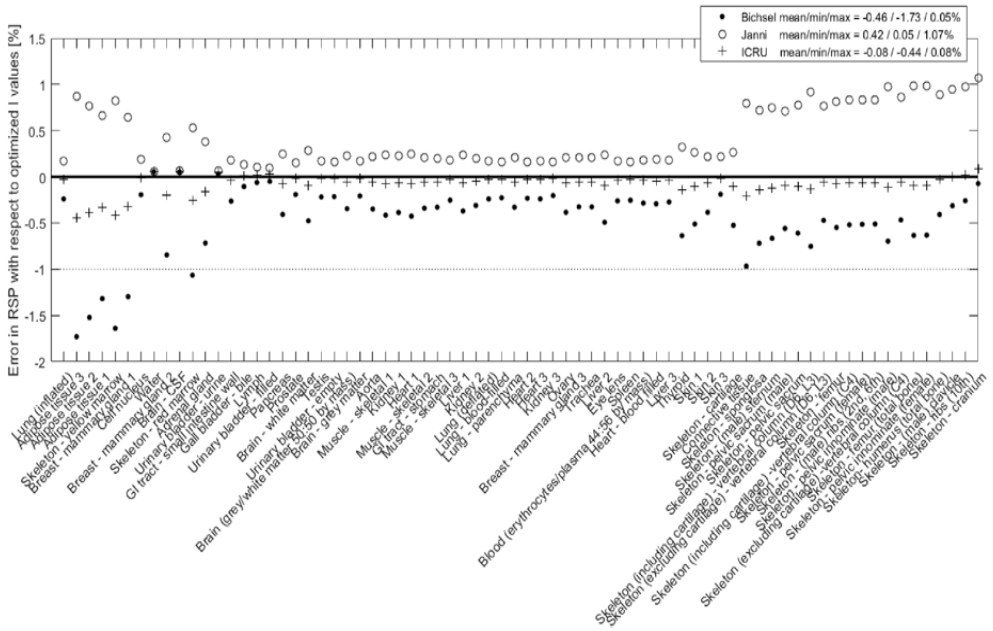

Figure 2.2: *Errors in the RSP for 72 human tissues, calculated using literature elemental I-values compared to using the optimized I-values. This figure was addapted from [DFCD$^+$16].*

fitted to measurement through the optimization of elemental I-values. These I-values should be used in subsequent estimates of human tissue RSPs, which are used to form the stoichiometric calibration curve.

2.1.2.1 Importance and applicability in carbon and proton therapy treatment

The presented theoretical formulations (Bichsel, Janni and ICRU) and the general formulation of the RSP (Schneider) only consider the electronic stopping power of a charged particle. For the same β, *i.e.*, energy per nucleon, the corrections presented by the different formulations of stopping power can be considered to be independent of the ion species, *i.e.*, the RSP values for both carbons and protons are the same for the same energies per nucleon. This is because the introduced corrections do not depend on the charged particle, depending only on the target, such is the case of the shell corrections. Bloch and Barkas corrections depend on the charged particle type. Bloch correction depends on z^2 while Barkas correction on z [WW02]. However, for treatment energies their effect can be approximately considered the same for both carbons

and protons. In fact, in clinical environment the RSP of carbons and protons are considered the same given the same initial energy per nucleon [WWK+15,MSSM10]. Therefore, since the I-value is independent of the particle's type, the results and conclusions derived previously in this section are applicable to both carbons and protons HU-RSP calibration curves.

Therefore, the proposed method should be implemented in clinical practice in order to reduce both proton and carbon range errors due to non-specific I-value in the determination of the HU-RSP calibration curve.

2.1.3 Conclusion

In this section, it was shown that there are different formulas to compute the SP of a charged particle and therefore different ways to determine the RSPs. Three theoretical SP formulations were presented, each with their own set of I-values. The RSP of Gammex inserts were computed using the different formulas and compared with their experimental values. Results showed that method with the lowest mean error was obtained for the Bichsel formulation. Using the Schneider method to compute the RSPs and the I-values from the different sources, the RSPs were also compared to the experimental values, being the average errors greater. Using the Schneider approximation, the ICRU elemental I-values were optimized until the theoretical tissue substitute RSP values matched measurements (mean error reduced from -0.53% to +0.11%).

The impact of not using these optimized elemental I-values was assessed by calculating the RSP of 72 human tissues with the Bichsel, Janni and ICRU elemental I-values. Results showed that without the optimization, mean errors would be up to -1.7%/+1.1%/-0.4% for Bichsel/Janni/ICRU respectively. The presented results suggest that experimental measurements of the tissue insert RSPs should be performed in order to obtain a list of optimized elemental I-values which will be used to compute the theoretical RSPs of other tissues.

2.2 Developing a phenomenological model for charged particle trajectories.

As mentioned in section 1.2.1.2, charged particles suffer MCS leading to uncertainties in predicting their path. This effect is expected to be mainly seen in protons than in carbons since these are heavier and faster (for the same range), suffering less scattering (equation 1.3). The classic X-ray CT reconstruction algorithms assume SLP, however due to MCS, this is not valid in charged particle imaging and such assumptions can lead to images with poor spatial resolution [SP94].

To tackle the MCS effect, different proton path estimates have been proposed. The MLP was first introduced by Schneider and Pedroni [SP94] and derivations of it have been proposed [Wil04a, SPTS08]. The MLP is a statistical approach which uses the incident charged particle entrance and exit coordinates/angles to derive an approximation of the real trajectory. These studies showed that the MLP is the most accurate path estimate, however, it requires certain amount of computational effort, slowing down reconstruction algorithms. Thus, CSP was introduced, providing reasonably good estimates of the proton path [LLS$^+$06].

In Wang *et al.* [WDA11], the SLP, MLP and CSP were compared for dosimetric pre-treatment verifications. The obtained results showed that the CSP could be used for proton path estimation since it is mathematically simpler than the MLP. The CSP requires knowledge of both the entrance and exit positions (X_0, X_1) and direction vectors (P_0, P_1). The magnitude of the direction vector is of great importance in CSP as multiple trajectories may cross the same entrance and exit position vectors as it is shown in Figure 2.3.

In Fekete *et al* [FCDD$^+$15b], it was derived a new formulation of the CSP, which included a phenomenological model of the direction vectors magnitudes.

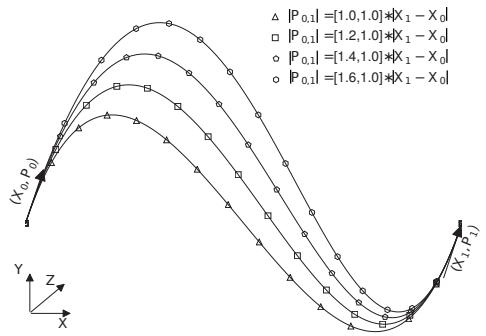

Figure 2.3: *Schematic representation of cubic spline paths with the same entrance and exit positions ($X_{0,1}$) and direction vectors ($P_{0,1}$) but with different magnitude of the direction vectors ($P_{0,1}$). Figure adapted from [FCDD+15b].*

2.2.1 Materials and methods

Three homogeneous phantoms (LN-300 lung, Water and CB2-50% $CaCO_3$ [Wat99]) with varying WET(10-30cm) were considered. Protons with initial energies of 180-330MeV were propagated through the phantoms. For each simulation 10^5 particles were used. The position of each particle crossing the phantom was recorded at 200 equally spaced, as well as the entrance and exit direction vectors. The simulations were performed using Geant4 [AAA+03] simulation code (v.4.9.p02). Standard processes include energy loss and straggling, multiple coulomb scattering using the model from Urban [Urb06] and elastic/inelastic ion interactions from Geant4 ion dedicated packages [LIK10].

2.2.1.1 Cubic spline path

Using the particle's entrance and exit positions vectors (X_0, X_1) as well as the entrance and exit directions vectors (P_0, P_1), the CSP of a charged particle ($S(t)$) can be modeled as:

$$S(t) = (2t^3-3t^2+1)X_0+(t^3-2t^2+t)P_0+(-2t^3+3t^2)X_1+(t^3-t^2)P_1 \tag{2.7}$$

$S(t)$ represents the position vector (X_t, Y_t, Z_t); the parameter $t \in [0, 1]$ represents the fraction of the distance traveled by the particle over the

total distance.

A charged particle's path divergence from a SLP increases with the transversed WET [Wil04b]. Also, more energetic particles deflect less. Therefore, it is reasonable to assume that the magnitude of the direction vectors is a function of incident energy and crossed WET.

The incident energy can be expressed in terms of range, so that the magnitude of the direction vector is dimensionless. The range of a charged particle in water can be expressed by the Water Equivalent Path Length (WEPL), which can be defined as:

$$WEPL(E_i) = \int_0^{E_i} \left(\frac{dE}{dx}\right)^{-1} dE \tag{2.8}$$

Where E_i is the particle's initial energy and dE/dx the particle's stopping power in water. The WET of a particle is the water equivalent thickness a particle crossed, so this can be computed from equation 2.8, but instead of the integral being between 0 and E_i it is between E_f and E_i, where E_f is the energy the particle after crossing the phantom.

In the work by Fekete *et al.* [FCDD$^+$15b] it is proposed a representation of the direction vector magnitude which minimizes the CSP Root Mean Square (RMS) deviation for all paths:

$$\begin{aligned} P_0 &= \hat{P}_0 \cdot \Lambda_0 \cdot |X_1 - X_0| \\ P_1 &= \hat{P}_1 \cdot \Lambda_1 \cdot |X_1 - X_0| \end{aligned} \tag{2.9}$$

With $\Lambda_{0,1}$ being a function that depends on both WEPL and WET.
Λ values were found by simulating proton CSP over a range of possible values. The optimal Λ_{opt} value is the one that minimizes the RMS deviation between the CSP and the MC proton path.

2.2.2 Results and Discussion

An optimal CSP was sought that minimized RMS deviation with a MC simulated proton path. To do so, two Λ factors were introduced into

equation 2.9 for adjustment of the magnitude of the direction vectors. The optimal Λ_{opt} were found by simulating different CSP over a range of possible values. The optimal values were the one that minimized the RMS deviation between the CSP and the MC path.

2.2.2.1 Cubic spline path fit to the proton path and generalization of the Λ_{opt} model

Figure 2.4 shows the $\Lambda_{0,1}^{opt}$ values that minimized the difference between the CSP and the MC path. Different WET/WEPL were considered as well as different materials. All the results converged on the same curve.

A quadratic law ($\Lambda_{0,1}^{opt} = A+B(WET/WEPL)^2$) with $A = [1.01, 0.99]$ and $B = [0.43, -0.46]$ was used as the best fit to the obtained data. The shaded area (blue/red) shows the uncertainty envelope.

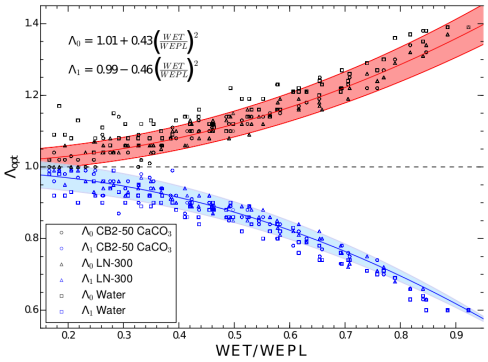

Figure 2.4: *The Λ_{opt} factor that minimizes the RMS deviation as a function of the WET/WEPL ratio. The shaded area represents the standard deviation between the fit (line) and the experimental data. Blue represents the values for Λ_1 and black/red the values for Λ_0. Image adapted from [FCDD$^+$15b].*

Using the $\Lambda_{0,1}^{opt}$ the RMS deviations between the MC proton path and their estimated CSP were calculated for 10^5 events, results are shown in Figure 2.5.

In Fekete *et al.* [FCDD$^+$15b], the CSP with optimized $\Lambda_{0,1}^{opt}$ was compared with the MLP. Results showed that the MLP required longer computation times than the CSP and that the CSP with $\Lambda_{0,1}^{opt}$ provided the

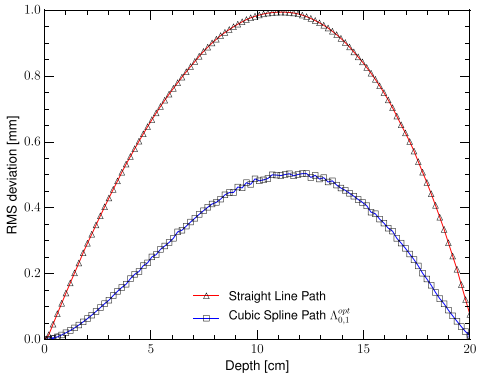

Figure 2.5: *RMS difference for the different path formulations. The CSP was calculated using the optimal Λ. The reference is the MC path over a 20cm water tank. 10^5 protons (E_i=200MeV) have been considered in the RMS computation. Image adapted from [FCDD$^+$15b].*

best compromise between an accurate estimate of proton trajectories and reasonable calculation time.

2.2.2.2 Phenomenological formulation applied to carbon paths

Carbons CSP trajectories were compared with SLP and MC trajectories. To do so, Monte Carlo (MC) simulations were used to propagate 10^5 carbons (500MeV/u) through a 30cm water tank.

The $\Lambda_{0,1}^{opt}$ derived by Fekete *et al.* [FCDD$^+$15b] and previously explained were used in the CSP calculation:

$$\begin{aligned} \Lambda_0 &= 1.01 + 0.43 \left(\frac{WET}{WEPL} \right)^2 \\ \Lambda_1 &= 0.99 - 0.46 \left(\frac{WET}{WEPL} \right)^2 \end{aligned} \tag{2.10}$$

Results for the RMS deviation and path representation are shown in Figure 2.6. As one can see by Figure 2.6-right, carbon RMS deviations are smaller than proton RMS deviations (Figure 2.5). The reason for such behavior is related with the fact that more energetic carbons were used and they are heavier particles. Consequently, the MCS is smaller for carbons than for protons.

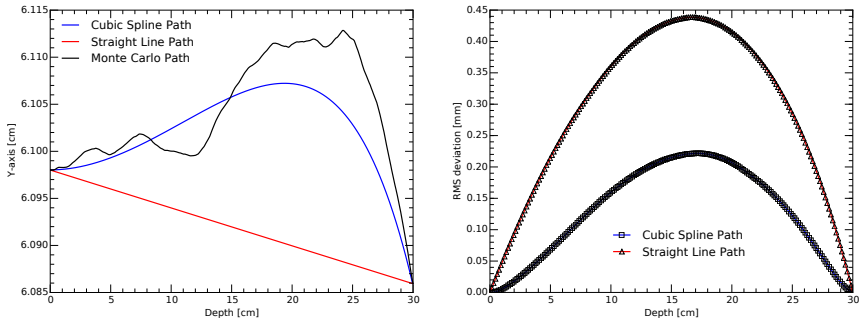

Figure 2.6: *The left figure displays the various carbon path estimates (SLP,CSP with Λ_{opt} and MC). On the right it is shown the mean RMS difference between the carbon paths and MC paths. 10^5 carbons with E_i=500MeV/u were propagated through a 30cm water tank.*

The CSP with Λ_{opt} reduced the RMS deviation from the SLP to about half. Nonetheless, the SLP path provides a reasonable approximation. The SLP RMS deviation for carbons was in the order of the CSP RMS deviation of protons (Figure 2.5). This reason contributes for the use of range detectors in carbon imaging, where no knowledge of the particle's position and direction are necessary. However, as shown the CSP with Λ_{opt} does improve carbon path accuracy and therefore should be used if the entrance and exit positions/directions are available.

2.2.3 Conclusion

The CSP proton trajectories were optimized by minimizing the RMS deviation between those reconstructed trajectories and a MC trajectory. Optimal Λ values for the direction vector magnitude were derived which minimized the RMS deviation. The Λ_{opt} that minimized the RMS deviation were parameterized as a power law function which depends on the WEPL/WET. Carbon trajectories were simulated through a 30cm water tank. CSP with Λ_{opt} and SLP were reconstructed and compared with the MC paths. CSP was able to reduce the RMS deviation to about half of the SLP. This optimization approach offers the potential for a better estimate of charged particles paths, leading to future better spatial resolution for charged particle radiography and CT.

CHAPTER 3

Edge detection using multiple peak detection with a range detector

As briefly mentioned in section 1.5, a source of range uncertainties comes from the organ motion and patient heterogeneity. Carbon beam therapy range precision is extremely sensitive to tissue density variations. These are further emphasized in the lung due to the high density difference between tumor and lung tissue. Therefore, lung tumor shifts/shrinkage can lead to high dose deposition on Organ at Risk (OAR)s. It is crucial to have correct knowledge of tumor edges for accurate dose delivery.

At the presence of high density interfaces, carbons from the same beam will cross different materials leading to multiple BP in the detector. The purpose of this chapter is to attempt to obtain tumor edge detection using information from these BPs.

The work here presented is based on the results and contribution made to the following work:

- **Investigation of tumor edge detection using multiple Bragg peak**

detection in carbon therapy, Marta F. Dias, Charles-Antoine Collins-Fekete, Guido Baroni, Marco Riboldi, Joao Seco. Submitted to Medical Physics, 2016 [DFB+16b];

- **PO-0822: Tumor margin estimation by multiple Bragg peak detection in carbon ion therapy**, M.F. Ferraz Dias, C.A. Collins Fekete, G. Baroni, J. Seco, M. Riboldi. Radiotherapy and Oncology, 2016 [DFB+16a];

- **SU-F-J-204: Carbon Digitally Reconstructed Radiography (CDRR): A GPU Based Tool for Fast and Versatile carbon imaging Simulation**, M F Dias, J Seco, G Baroni and M Riboldi. Med. Phys. 2016, [DSBR16].

3.1 Multiple Bragg peak detection due to human heterogeneity

Carbons are very sensitive to tissue density variations, which is further accentuated within the lung region due to the high density difference between tumor and lung tissue. As documented by Mori *et al.* [MZK13, MDS+14], tumor shifts/ shrinkage can lead to geographical miss and/or high dose deposition on OARs.

Different approaches have been considered in order to account for these effects and to increase the accuracy in treatment planning [MZK13]. One of these approaches, as it is explained in section 1.6.2, is carbon imaging, since it offers a direct way to obtain information about the carbon beam behavior during treatment and a low dose image that can be used for patient and target positioning [RBG+13, TJM12, MNA+07, ASF12, HBSS14, DS13].

Recent detectors [RBG+13, ASF12] have been developed with the aim to reproduce carbon radiography (c-rad)/CT through measurement of the BP position produced in a range detector, after these cross the material to be imaged (section 1.6.2). Different image reconstruction methods using the BP position extracted from range detectors have been

documented [RBJ+14, KTB+15]. However, they require the irradiation of the patient over different positions/angles causing a high dose delivery, long acquisition/reconstruction times. Moreover, carbon imaging is limited by the accelerator maximum energies, *i.e.*, it is not possible to produce carbon beams energetic enough to cross certain body regions.

The BP position can be translated into WET through a calibration process (see Rinaldi *et al.* [RBG+13] for further details). The WET can also be computed as the integral of the materials RSP along carbons path, l [FCDD+15b]:

$$WET = \int_l RSP \partial l \tag{3.1}$$

As it was mention in section 1.6.1, through the RSP value one can compute the beam energy to position the BP within the tumor delineation. The current clinical approach to obtain information about carbons RSP, is to use the HU-RSP calibration curve (section 1.6.1), which induce range errors (section 1.5).

In a clinical environment, one has to deal with a Gaussian-like pencil beam. Since the human body is heterogeneous, carbons from the same incident beam traverse various materials, causing range dilution effects. In the case of high contrast interfaces along the beam path, multiple BPs and/or range dilution may occur, contributing for errors in the computation of the WET.

The main purpose of this work was to attempt to obtain information of tumor/target (gross tumor volume) edges position using a reduced number of irradiation beams. To do so, a theoretical model is proposed which allows through a single irradiation beam close to the interface to determine the distance between the edge and the beam lateral position. When more than two BP are detected, the interface is scanned to retrieve the interface/edge position. X-ray CT prior-knowledge is required in the later case to determine the relevant BPs that describe the interface. MC and ray tracing simulations were performed to validate the proposed ap-

proach.

3.2 Materials and Methods

A theoretical formula was derived which outputs the distance between the beam lateral position and a edge/interface when two clearly distinguished BPs are detected.

3.2.1 Edge detection through two Bragg peaks

3.2.1.1 Edge detection through two Bragg peaks: theoretical formulation

To derive an initial theoretical formulation, let one first assume that there is only one interface parallel to the beam direction given by two different homogeneous materials (Figure 3.1a - a water tank with a CB2-50% $CaCO_3$ [Wat99] rectangular insert). This interface is then irradiated with carbon beams with various Full-Width-Half-Maximum (FWHM). Carbons paths (represented in green and blue) will either cross the water medium (green carbons) or the bone (blue carbons).

A range detector (Figure 3.1b), located at the end of the phantom records the energy deposition of the carbons after these have crossed the phantom. Two BPs are detected (Figure 3.1b, red line): one corresponding to carbons that crossed the insert (shallower BP at depth R_2) and the other to carbons that crossed only water (deeper BP at depth R_1). The intensity difference between the two BPs can be computed as:

$$\Delta I = \frac{\partial E(R_2) - \partial E(R_1)}{\partial E(R_1)} \tag{3.2}$$

Where $\partial E(R_2)$ and $\partial E(R_1)$ are the BPs intensity at depth R_2 and R_1, respectively (Figure 3.1b). The relationship between the intensity of these two BPs can be analytically modeled. Assuming a mono-energetic (initial energy $E_1(0)$) carbon beam impinging on a homogeneous medium such as a water tank, its depth-dose distribution will be similar to the one represented by the green dashed in Figure 3.1b. The position of the BP can be determined by the charged particle's range (R_1) which can be computed by [BS96]:

$$R_1 = \alpha E_1(0)^p \tag{3.3}$$

With α and p being fitting parameters. The beam deposits energy along its path between $z = 0$ and R_1 in the medium. The remaining energy $E_1(z)$ at an arbitrary depth $z < R_1$ must be enough to travel the distance $R_1 - z$. Thus, according to equation 3.3:

$$R_1 - z = \alpha E_1(z)^p \Leftrightarrow E_1(z) = \left(\frac{R_1 - z}{\alpha}\right)^{1/p} \tag{3.4}$$

The energy deposit along a particle path is determined by its derivative:

$$-\frac{\partial E_1}{\partial z} = \frac{(R - z)^{1/p-1}}{p\alpha^{1/p}} \tag{3.5}$$

This equation allows the computation of the dose/intensity delivered at any point $z < R_1$.

At the presence of an interface the total signal is given by the superimposition of two Bragg curves (Figure 3.1b), green and blue curves). Let one consider the following assumptions:

1. The effect of multiple coulomb scattering can be neglected and carbons are assumed to travel straight trajectories.
2. The contribution of secondary particles after the Bragg Peak can be considered null when compared to the peak contribution (no tails due to secondaries).
3. The probability of losing carbons from the main beam is the same in both materials.
4. The Bragg curve shape does not depend on the initial beam energy, only its peak position depends on it.
5. The lateral beam distribution can be approximated to a Gaussian function, and since scattering is negligible, this is assumed to be valid at any depth along the phantom.

6. The reference position is such that its origin is placed at the phantom entrance and interface position. The scans are always performed from the most dense (negative beam positions) to the least dense material (positive beam positions).

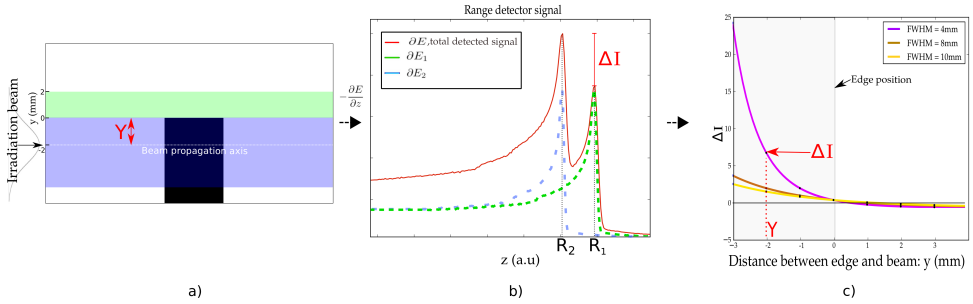

Figure 3.1: *Bone insert in a water phantom. The green area represents the least dense carbon path, whilst the blue one represent the carbons crossing the densest material. Figure b) shows the detected signal from irradiating the phantom. The total signal is the summation of all Bragg curves. In blue the ones crossing below the edge and green the ones above the edge, the dashed lines have been normalized to its maximum. Figure c) contains the theoretical ΔI which was computed using equation 3.9. The x-axis is the lateral distance between the beam and the edge (Y). The gray shaded area represents the most dense material, while the white are the least dense material.*

Figure 3.2 represents the beam's distribution profile crossing the interface. Consider N as the total number of carbons in a beam, $W_1 \times N$ the number of carbons crossing the least dense material and $W_2 \times N$ the most dense material (above and below the interface in Figure 3.1a, green and red area respectively in Figure 3.2), logically it follows that $W_1 \times N + W_2 \times N = N \Leftrightarrow W_1 + W_2 = 1$. Given these, the overall intensity ∂E at depth z:

$$\frac{\partial E}{\partial z}(z) = W_1 \frac{\partial E_1}{\partial z}(z) + W_2 \frac{\partial E_2}{\partial z}(z) \tag{3.6}$$

From assumption 4, 2 and making z the position of the shallower peak (R_2) (Figure 3.1b) the following approximations can be made:

$$\begin{aligned} \frac{\partial E_2}{\partial z}(R_2) &= \frac{\partial E_1}{\partial z}(R_1) \\ \frac{\partial E}{\partial z}(R_1) &= \frac{\partial E_1}{\partial z}(R_1) \end{aligned} \tag{3.7}$$

Rewriting equation 3.6 and dropping the term ∂z:

$$\partial E(R_2) = W_1[\partial E_1(R_2) + (W^{-1} - 1)\partial E_1(R_1)] \tag{3.8}$$

So, taking all of these equations and considerations into account, and making $R_1 - R_2 = \Delta WET$, which represents the water equivalent thickness difference between the two materials, the equation 3.2 can be rewritten as:

$$\Delta I = \lambda^{1-1/p} \Delta WET^{1/p-1} + (W_1^{-1} - 2) \tag{3.9}$$

Where λ represents the minimum distance when z is at the BP position, *i.e.* when equation 3.5 reaches its maximum.

λ and p depend on the incident beam, and can be determined through a calibration procedure which will be later explained; W_1 as mentioned is the percentage of carbons crossing the least dense material. This depends on the beam position and can be obtained by the integral of the Gaussian distribution from $-\infty$ to the edge position in relation to the beam, as it is represented in Figure 3.2:

$$W_1 = \frac{1 - erf\left(\frac{Y}{\sigma\sqrt{2}}\right)}{2} \tag{3.10}$$

Making Y positive if the beam propagation axis is placed in the least dense medium and negative when place in the most dense material, from equation 3.10, it is possible to compute the lateral distance between the beam propagation axis and the edge, Y :

$$Y = \sqrt{2}\sigma erf^{-1}(2W_1 - 1) \tag{3.11}$$

erf and erf^{-1} are respectively the error function and its inverse. W_1 can be obtained from the measured signal through equation 3.9.

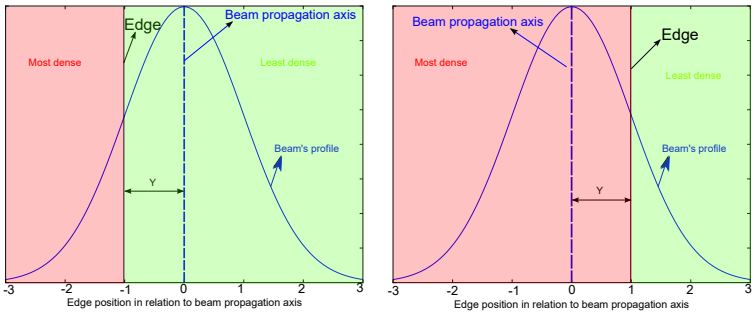

Figure 3.2: *Representation of interface shifts. From treatment planning the origin of the referential is positioned at the interface, however, this has shifted* $1mm$ *to the left and right respectively on the time of treatment delivery.*

Figure 3.1c shows the expected ΔI as a function of the distance from the beam derived from the theoretical formulations (equation 3.9), for a $\Delta WET = 2cm$, a $\lambda = 0.20$ and $p = 1.37$.

3.2.1.2 Edge detection through two Bragg peaks: Validation through Monte-Carlo simulations

Two phantoms were considered. The first one is water tank with a rectangular bone insert (CB_2-50% $CaCO_3$) for initial measurements. The insert is placed at the middle of a water tank and is irradiated for different beam lateral positions (y = [-3, -2, -1, 0, 1, 2, 3]mm). The second phantom is a semi-cylindrical bone insert (radius = 2cm) to reproduce range dilution effects.

A water tank ($10 \times 10 \times 20$ cm) was placed at the exit of the phantom in order to simulate a range detector. The deposit energy was measured every 0.4mm along the beam propagation axis. The generated signal was analyzed and the BPs intensity and ΔWET were obtained to retrieve the beam lateral distance to the edge position. This distance was compared to the real known position of the edge.

All MC simulations were performed using Geant4 [AAA+03] simulation code (v4.9.6.p02). Standard processes include energy loss and straggling, MCS using the model from [Urb06] and elastic/inelastic ion interactions from Geant4 ion dedicated packages [LIK10]. 400 MeV/u carbon (C_{12}) beams were used (n=10^6) and three different FWHM were considered, 4mm, 8mm and 10mm.

3.2.1.3 Edge detection through two Bragg peaks: Calibration curve and limitations

Equation 3.9 requires the knowledge of λ and p which need to be determined through a calibration procedure. First, the phantom with the rectangular insert was irradiated with the beam centered at the edge position (x = y = 0), for different thicknesses (along the z-axis) of bone inserts. Since the beam lateral position was aligned with the edge, the term $W_1 - 2$ disappears from equation 3.9. Without this term, ΔI can be computed by changing ΔWET. λ and p can then be inferred from a fit applied to the obtained values.

The detection of two BPs in the measured signal is limited by two factors, the detector depth spatial resolution and the width of the different BPs. To retrieve the minimum distance for two BPs to be separable, the insert width was reduced until they both collapsed into a single BP.

3.2.2 Edge detection through multiple Bragg peaks

3.2.2.1 Edge detection through multiple Bragg peaks: clinical environment and scanning edge

The theoretical formulation has two main limitations. First, it requires a calibration procedure to determine λ and p. Second, the model only works when two sharp BPs are detected. More than two BPs can be detected due to the human body heterogeneity and more than one interface/edge can be present along the beam propagation axis (Figure 3.3). In a clinical scenario, it is necessary to identify the two relevant BPs that describe the sharp edge to parameterize the theoretical $\Delta I - \Delta WET$ curve (equation 3.9). To perform this identification, X-ray CT prior-

knowledge is used.

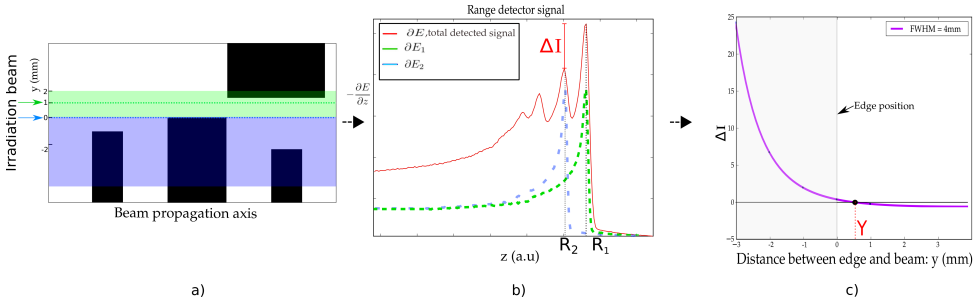

Figure 3.3: *Representation of the scanning edge method. Figure a) shows a phantom with multiple high contrast interfaces. The relevant edge is at y=0mm. Figure b) shows the detected signal (red signal) from irradiating the phantom a). The green dose deposition curve is the expected signal for a beam FWHM=0mm positioned at y=1mm. The blue curve for a beam positioned at y=0mm. c) contains an expected $\Delta I - \Delta WET$ curve. Y gives an approximation of the interface position.*

The treatment planning CT can be used to reproduce the expected Bragg signal in a range detector. The HU are converted into RSP using a calibration curve (section 1.6.1). Knowing the beam position, the calibration curve, and assuming straight paths, one can compute the expected Bragg curve. To do so, one can re-write equation 3.1 in a discrete way, where the WET crossed by each carbon from the beam, i is:

$$WET_i = \sum a_{ij} RSP_j \tag{3.12}$$

with a_{ij} being the length crossed by carbon i in the voxel, j with RSP$_j$ (Figure 3.4).

The WET can be converted into a Bragg curve as it will be explained later explained.

For a FWHM> 0 (clinical beam), as previously mentioned, carbons from the same beam cross different materials. The detected signal is the sum of all these Bragg curves of given by each individual carbon. This effect is represented in Figure 3.3 and Figure 3.5.

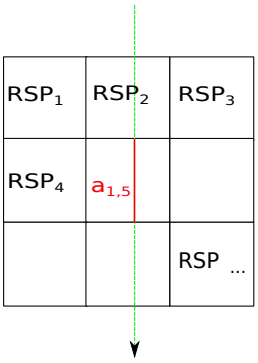

Figure 3.4: *Representation of a carbon straight path (green dashed line) crossing voxels from a CT. Each voxel has a RSP value and $a_{1,5}$ is the crossed length in the voxel $j = 5$ by the 1st-carbon.*

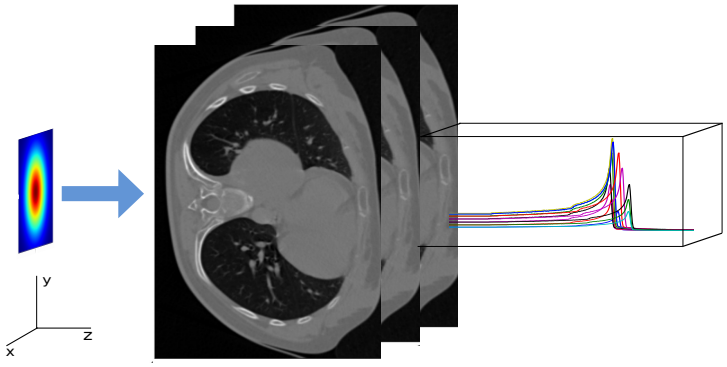

Figure 3.5: *Schematic representation of a 2D-Gaussian beam impinging on a 3D volume. Each carbon from the beam will cross different structures leading to multiple Bragg curves being detected. The final signal detected is the sum of all these curves. Each curve will have a weight to the final signal that can be determined by the initial 2-D Gaussian distribution of the incident beam. The blue arrow represents the beam's direction.*

3.2.2.2 Edge detection through multiple Bragg peaks: Validation with ray-tracing

In order to simulate a clinical environment a real lung CT was considered. 5×10^4 carbons (FWHM=4mm) were propagated along the CT voxels and the WET of each individual carbon was computed to do this a Carbon Digitally Reconstructed Radiography (CDRR) tool was developed. The lung CT patient data were obtained from the The Cancer Imaging Archive [CVS+13].

3.2.3 Carbon digitally reconstructed radiography (CDRR): A GPU based guided user interface.

A python interface tool was created in order to simulate the signal generated in a range detector after carbons crossed a CT volume. In Figure 3.6 it is shown a schematic representation of how the exit signal after carbons cross a CT is computed.

The HU-RSP calibration curve is used to convert the HU values from a CT or 4DCT into RSP. With Graphics Processing Unit (GPU) based ray-tracing algorithm carbons from an incident beam with a given energy and FWHM are propagated through the CT and the WET crossed or the energy lost computed.

The exit signal can be represented in three different ways: as a range map; an energy map or a Bragg peak spectrum. The range map contains the distribution of the WET values of each carbon that has crossed the CT. This can be determined from equation 3.12.

The energy map shows the energy carbons exit the CT, E_i^{out}, this can be approximated to:

$$E_i^{out} = E_i^{in} - \sum SP_j \times a_{ij} \tag{3.13}$$

E_i^{in} is the incident energy of each i^{th}-carbon and SP_j is the stopping power, *i.e.*, the energy lost in the voxel j. The SP_j can be computed from the RSP value of each voxel. As previously mentioned, the RSP of a material is the ratio of its SP over the SP of water. The SP of water

for carbons was obtained from Geant4. The exit energy is basically the incident energy minus the sum of the energy lost in each voxel a carbon has crossed.

The BP spectrum detector, which basically simulates the response of range detector, is obtained by the sum of each depth-dose curve of each individual carbon from the beam (Figure 3.5). In order to simulate the different depth-dose curves, a Bragg curve was obtained through MC simulation. A carbon beam with a range of 30cm was propagated through a water tank. If a slab of material is placed in from of the detector, the Bragg peak position is shifted from the reference. This shift gives the crossed WET as it is illustrated in Figure 3.7.

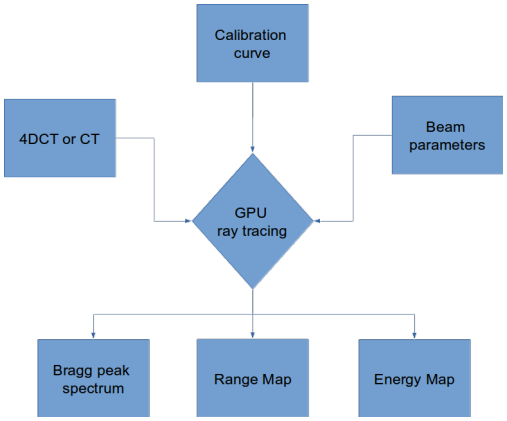

Figure 3.6: *Schematic representation of how the CDRR tool works. First the user needs to insert the input variables. These are the CT/4DCT image, the calibration curve and the beam parameters: FWHM, number of rays, number of parallel beams and distance between the beams. The user will need to select the beam direction and slice to be crossed. A ray tracing algorithm will be run and from the calibration curve the WET crossed by each carbon in the beam computed. The WET is then converted into: range; energy and/or Bragg curve spectrum.*

3.3 Results

3.3.1 Edge detection through two Bragg peaks

This section presents the results for the first two phantoms, *i.e.* the rectangular insert and the semi-cylindrical insert. First the calibration curve

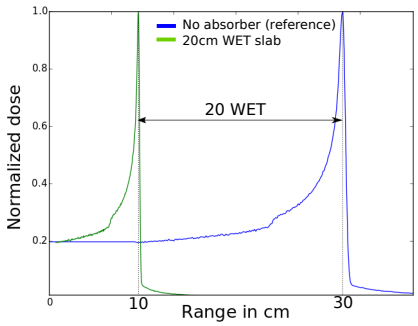

Figure 3.7: *How the range detector is simulated by shifting a reference peak, which was obtained without an absorber material in from of the detector (water tank). The distance between the reference peak location and the measured one is the WET of the crossed material placed in front of the detector.*

and its parameters (λ and p) were computed following the procedure in section 3.2.1. Then, the distance between the irradiation beam and the edge using the theoretical model was computed for each phantom.

3.3.1.1 Edge detection through multiple Bragg peaks: obtaining the calibration curve

As expected, two BPs were detected on the range detector after crossing the high contrast interface (Figure 3.8a). In Section 3.2.1, an expression was derived which allows the computation of the lateral distance between the beam propagation axis and the edge (equation 3.11).

Figure 3.8b shows the obtained results for the calibration curve. The data was fitted using the power relationship in equation 3.9 to compute λ and p. For smaller ΔWET, it becomes more difficult to determine the exact relationship between the two BPs. This can be visualized in Figure 3.8a, where the two BPs started to collapse into one.

To minimize this effect a threshold of ΔWET=3mm was chosen as a conservative minimum difference between two BPs to be separable. Although BP identification is affected by the detector range resolution, Rinaldi *et al.* [RBJ$^+$14] have shown a potential resolution of 0.8mm, which is below the limit imposed by range dilution (3mm).

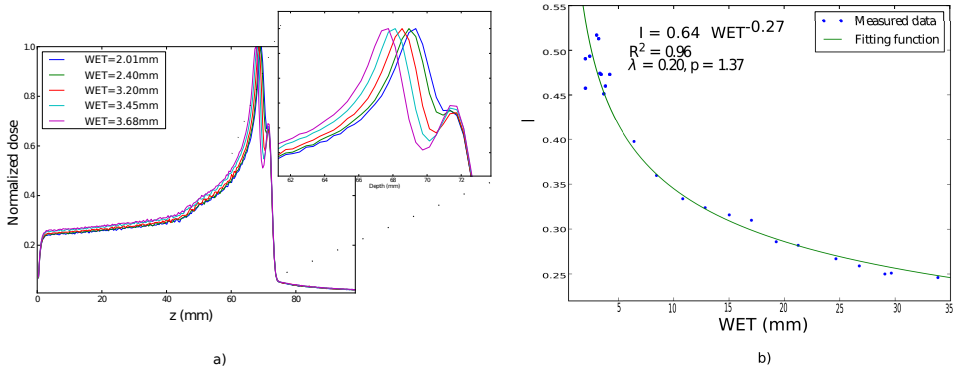

Figure 3.8: *Figure a) obtained signal after irradiating the phantom with the rectangular insert with thickness of 0.55,0.60,0.70,0.80,0.90cm. The ΔWET was obtained by the difference between the two BPs position. Figure b) calibration curve: intensity difference, ΔI , as a function of ΔWET. The data was obtained by placing the incident beam aligned with the interface and by changing the insert thickness.*

3.3.1.2 Edge detection through two Bragg peaks: theoretical formulation

For the two different initial phantoms (2cm rectangular bone insert and 2cm radius semi-cylindrical), the BP intensities (equation 3.9) were measured at different lateral irradiation positions (y = [-3, -2, -1, 0, 1, 2, 3]mm), ΔWET and ΔI were computed.

Figure 3.9 shows the obtained signal for different beam FWHM (4,8,10mm) and beam lateral positions on the semi-cylindrical insert phantom. The distance between the beam and the edge (Y in Figure 3.1a) was computed for the different irradiation beam positions (equation 3.11). The results are presented in Table 3.1 and 3.2 for the rectangular and semi-cylindrical phantoms respectively. The lateral distance is the distance between the irradiation beam and the edge position which is known from parametric definition of the phantom. The uncertainty was computed by taking into account a 2% variation in the fitting parameters λ and p to evaluate the robustness.

As mentioned before, the theoretical formulation requires a calibration procedure and only accounts for the detection of two BPs. A good approximation to determine the edge position is by scanning the interface to obtain the $\Delta I - \Delta WET$ curve. Figure 3.10 shows ΔI as a function of

Table 3.1: *Distance between the beam position and interface using equation 3.9. The standard deviations were computing using a 2% variation on λ and p. The negative sign means that the beam is inside of the densest material of the interface. These data was computed for the phantom with the rectangular insert.*

Lateral distance (mm)	FWHM = 4mm Y(mm)	FWHM = 8mm Y(mm)	FWHM = 10mm Y(mm)
-3	-2.35 ±0.001	-3.00±0.01	-2.67±0.01
-2	-1.70±0.003	-2.08±0.01	-1.96±0.02
-1	-0.93±0.010	-1.20±0.02	-1.13±0.03
0	-0.11±0.020	-0.34±0.03	-0.32±0.04
1	0.61±0.030	0.59±0.05	0.56±0.05
2	1.15±0.050	1.38±0.07	1.10±0.07
3	-	2.06±0.09	1.86±0.09

Table 3.2: *Distance between the beam position and interface using equation 3.9. The standard deviations were computing using a 2% variation on λ and p. The negative sign means that the beam is inside of the densest material of the interface. These data was computed for the phantom with the semi-cylindrical insert.*

Lateral distance (mm)	FWHM = 4mm Y(mm)	FWHM = 8mm Y(mm)	FWHM = 10mm Y(mm)
-3	-2.04±0.001	-3.34±0.16	-3.96±0.18
-2	-1.21±0.01	-2.78±0.12	-2.90±0.13
-1	-0.38±0.013	-1.66±0.06	-1.94±0.09
0	0.47±0.03	-0.89±0.06	-1.13±0.07
1	1.24±0.05	0.02±0.04	-0.25±0.03
2	1.84±0.09	0.88±0.02	0.73±0.03
3	-	1.76±0.02	1.63±0.02

the beam position for both phantoms, for the rectangular insert (left) and the semi-cylindrical insert (right). The theoretical equation that predicts the $\Delta I - \Delta WET$ curve (equation 3.9, Figure 3.1c) has a power function dependency. For this reason, in the clinical scenario where no analytic solution can be found, it is assumed the following fitting function:

$$\Delta I = A\Delta WET^{By} - 1 \tag{3.14}$$

A and B are the fitting parameters. Equation 3.14 fit was applied to the data and offered a high regression coefficient (R^2 >0.9) and describes the $\Delta I - \Delta WET$ curve. The interface position can be approximately assumed to be positioned at $\Delta I = 0$.

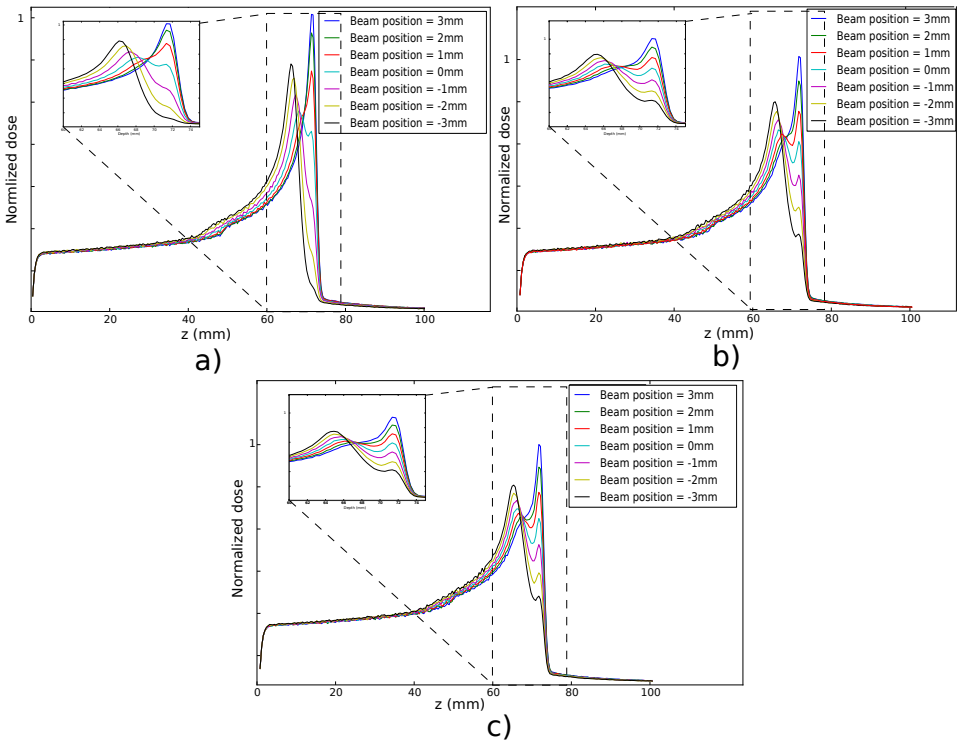

Figure 3.9: *Obtained Bragg curves from irradiating the phantom with the semi-cylindrical insert with different FWHM and beam positions. Figure a) FWHM=4mm, Figure b) FWHM=8mm, Figure c) FWHM=10mm.*

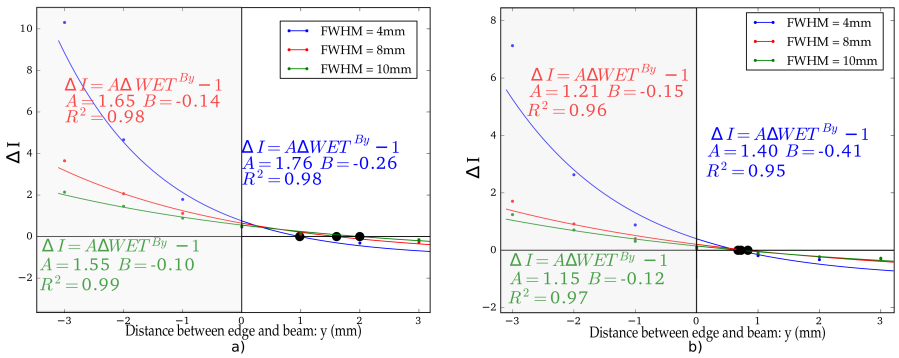

Figure 3.10: ΔI *as a function of the distance between the beam and the edge. Figure a) data obtained for the phantom with the rectangular insert. Figure b) data obtained for the semi-cylindrical insert. The bold black dots represent* ΔI*=0.*

3.3.2 Edge detection through multiple Bragg peaks: clinical environment and scanning edge

A ray tracing method with Gaussian carbon beams (FWHM=4mm) was used to simulate a range detector signal. Data from a lung tumor CT was used and two beam directions selected to represent the high-gradient interface (Figure 3.11a, $Beam_1$ and $Beam_2$). A scanning of the interface was performed for y = [-3,-2,-1,0,1,2,3]mm for the two beam directions.

The reference BPs positions were computed at beam lateral positions y = [0,+1]mm (Figure 3.11a-right dashed curves). The respective Bragg curves were obtained (Figure 3.11b) and the ΔI was computed as a function of the beam lateral distance to the interface (Figure 3.12). The power fit in equation 3.14 was applied to the measured intensities and the ΔI = 0 extracted. From this point, the interface position was calculated and compared to the known position from the CT.

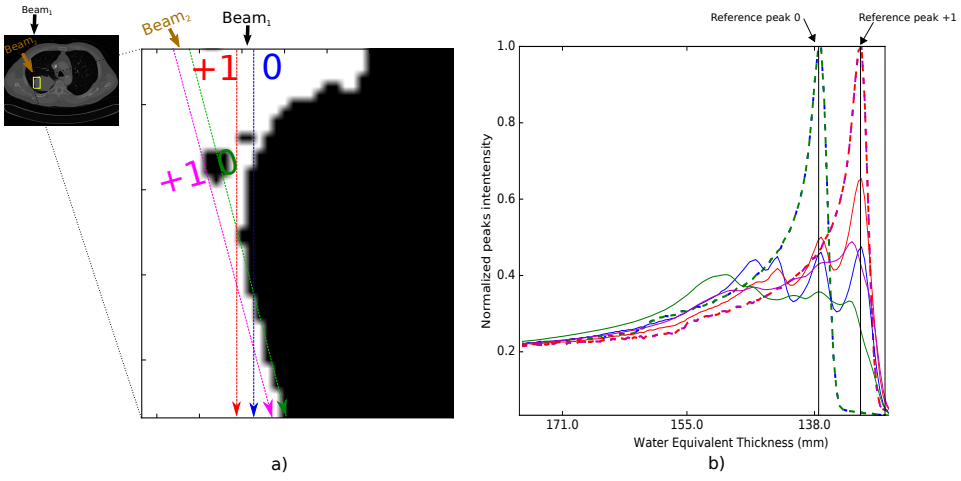

Figure 3.11: *Figure a) Slice from a CT of a lung adenocarcinoma. The colored lines represent the different beam directions/scanning positions. Two different directions are considered: $Beam_1$ and $Beam_2$. The spacing between each scanning position is 1mm. Figure b) shows the detected signals for a FWHM=0 (dashed) and FWHM=4mm (filled line) for the beam positions/directions shown in a).*

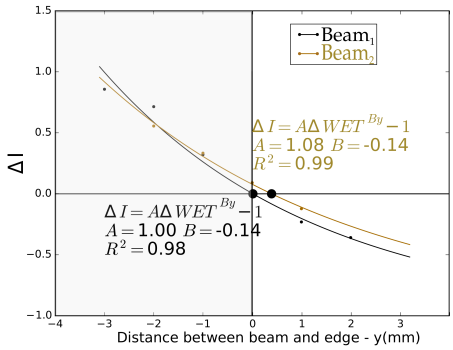

Figure 3.12: *ΔI as a function of the beam positions for the lung CT case for two different beam direction (Figure 3.11a). The data was obtained using a FHWM=4mm. The black dots represent ΔI=0.*

3.3.3 Number of scanning positions necessary to retrieve edge detection

In order to reduce the dose given to the patient, only two scanning positions were considered. For all the phantoms, the error between the real edge position and the computed one from the power fit (equation 3.14, by making $\Delta I = 0$) were calculated. For robustness evaluation, multiple pairs of scanning points were used with different distance to each other. Figure 3.13 shows the obtained errors as a function of the distance between the selected scanning points.

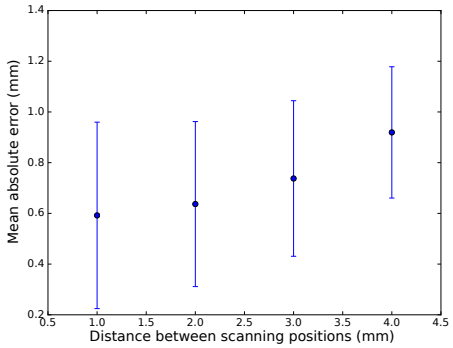

Figure 3.13: *Absolute errors from the edge detection for all study cases. The interface position was obtained using an exponential fit considering only two irradiation spots. The x-axis shows the distance between the two irradiation positions. The standard deviation of the errors comes from different pair of irradiation points near the interface.*

3.3.4 Carbon digitally reconstructed radiography (CDRR): A GPU based guided user interface

Figure 3.14 shows the CDRR tool interface layout. Written in red it is explained what is the function of each area. The user is allowed to draw the beam directions on the selected slice of the uploaded CT/4DCT. Per beam direction, the user can select the number of parallel beams being shot and the spacing between them (Figure 3.14, colored dashed lines crossing the CT). Each beam has a 2D-Gaussian distribution. The GPU-ray tracing method allows the computation of a range detector response by considering that each individual carbon from the beam crosses different materials (Figure 3.11).

By knowing the WET crossed it is possible to infer the required minimal energy necessary to cross the full patient so that a carbon image can be built. This tool offers an easy and fast way to simulate carbon imaging data without the need to use MC simulations. It can be used for educational and for clinical purposes, allowing the user to test beam energies and angles before real acquisition.

3.4 Discussion

A theoretical model was derived which provides the distance between the irradiation beam lateral position and a high-gradient interface in a phantom, using information from two BPs (equation 3.11). The model was tested using two phantoms; one with a rectangular insert and the other with a semi-cylindrical insert (Table 1 and 2). The theoretical prediction of the interface position matched the real interface positions up to a maximum deviation of 0.9mm when using a Gaussian FWHM = 4mm. When the interface was farther apart from the beam central position, it became difficult to discriminate the two BPs in the measured signal beam and the expected error was greater.

The semi-cylindrical insert simulated range dilution in the tumor. Figure 3.9 shows the obtained signal for three different beam FWHM. The

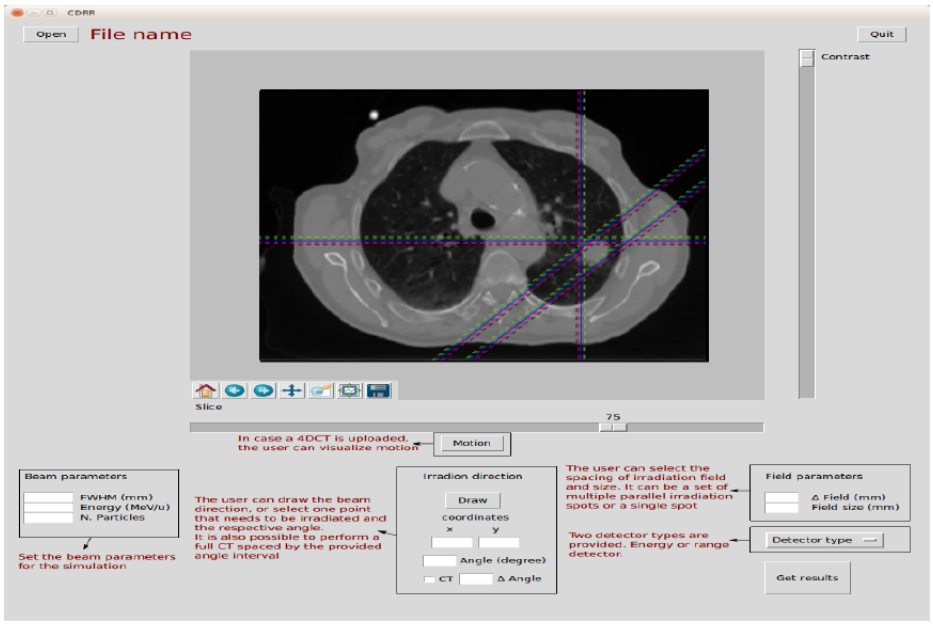

Figure 3.14: *Interface layout of the CDRR tool. In red it is explained the different functions of the tool.*

shallower BP (i.e. from the carbons that cross the densest material) is smeared and its depth position depends on the beam's FWHM. This can be easily explained by the insert geometry: broader the beam, thicker is the insert along the beam's path. The theoretical formulation (equation 3.11) was applied in these non-optimal conditions with results shown in Table 2. These show that the range dilution effects induced by the semi-cylindrical insert do not severely influence (accuracy<1mm) the theoretical formulation.

The deviations between the real edge position and the ones extracted from the derived model might come from different sources: the tail in the Bragg curve due to nuclear reactions; MC noise; detector discretization and range dilution effects. None of these was considered in the derivation of the theoretical model.

A limitation from equation 3.11 is that it requires a calibration procedure, working solely in the presence of a single interface, i.e. only two detected BPs. Moreover, it only accounts for displacements along

the y-axis. To overcome these limitations in clinical cases, the interface was scanned and a power fit (equation 3.14) applied to the obtained data.

The power fit was first applied in the simple parametric phantoms. The BP, ΔI and ΔWET were extracted from the detector output signal. The $\Delta I - \Delta WET$ power fit (equation 3.14) was applied to the data and a high regression coefficient was found (R^2 >0.9). In clinical environment, the WET crossed is given by the most intense BP, considering this and from the results in Figure 3.9, one can approximate the edge to be positioned when $\Delta I = 0$. For a beam with FWHM=4mm this approximations leads to an error smaller than 1mm (Figure 3.9).

The power-fit results obtained for the semi-cylindrical insert results were more accurate than the rectangular insert. This can be explained by the range dilution effect on the signal. Range diluted BPs are smeared, decreasing their total intensity and leading to a decrease in ΔI. Consequently, the beam ΔI at the interface is closer to be zero.

Next, the scanning method was applied to a clinical environment where the edges of a lung tumor were scanned. Figure 3.11 shows that more than two BPs were detected in the range detector. These come from the irregular tumor shape and/or more than one high contrast interface, such as bone structures or metastases along the carbon's path. Prior-knowledge is used to retrieve a first approximation of the expected BPs positions. This is done by shooting a narrow single beam (FWHM = 0) at two scanning positions around interface edges (Figure 3.11). The power fit in equation 3.14 was applied to the measured intensities and the ΔI=0 point was computed. As in the previous results, the power fit provided a good approximation to the data for both beam directions (Figure 3.12).

As means to reduce the dose delivered to the patient, only two scanning positions were considered. The results showed that a 1mm sampling of the scanning positions provided an accuracy with an error lower than 0.9mm (Figure 3.13). The use of only two scanning beams ensure that the total dose to the patient is less than with any other techniques. A

limitation of this method is that by making ΔI=0 at the interface it is introduced a bias towards placing the edge at the least dense medium. However, this bias is smaller than 1mm in all scenarios for a beam with FWHM<=4mm.

The clinical section work is limited by the requirements of a X-ray CT prior knowledge to identify the edge position. Furthermore, the minimal resolution possible is restricted by the half of the FWHM. Per example, a Gaussian beam with FWHM =4mm cannot detect an edge movement greater than $\pm$2mm since very few carbons cross either inside/outside the interface, and the BP pair does not appear in the detected signal. The disappearance of the BP pair indicates a sizable edge movement, which could be used as a trigger for replanning.

From these results, one can conclude that when only two BPs are detected it is possible to compute the edge position just by irradiating within a FWHM/2 mm field around the interface. However, it requires the computation of the beam parameters and it is not applicable for cases in which more than two BPs are detected. On the other hand, scanning the edge interface allows the determination of the tumor edge when using two or more scanning beams with accuracy<1mm.

3.5 Conclusion

The irradiation of a high contrast interface leads to the detection of two BPs in a carbon range detector. Each BP contains information about the structures that were crossed. In this study it was derived a formulation, based on the theoretical definition of a Gaussian beam and the dose deposition curve of carbons, to determine the position of an edge with respect to the incident beam. It was showed that if the measured signal has only two BPs, it is possible to determine the distance between an edge and the irradiation beam with a single shot. When more than two BPs are detected, the interface position can be determined by scanning the edge at multiple scanning points ($n \leq 2$). A $\Delta I - \Delta WET$ power fit is applied to the obtained data and the edge retrieved by mak-

ing $\Delta I = 0$. Both methods provided results with an error lower than 1mm. Prior-knowledge strategies are required for the identification of the relevant BPs when more than two are detected. The technique seems promising since it allows edge detection with a few irradiation beams (two are sufficient), providing a low dose to the patient and does not require image reconstruction methods. If performed during treatment it offers a fast way to determine where edges are positioned and decreasing OARs dose.

Future work should include testing the proposed methods with other structures where high contrast interfaces are present and experimental work, where range detector noise and resolution can influence the models.

CHAPTER 4

Charged particle radiography combined with X-ray CT to determine patient-specific calibration curve

As mentioned in section 1.6.1, in charged particle (carbon and proton) therapy the range of the incident particle in the patient's body is calculated using information from X-ray computed tomography (CT) leading to range uncertainties up to 5%. The aim of this chapter was to evaluate if these uncertainties can be reduced by combining charged particle radiography with pre-treatment X-ray CT to determine a patient specific calibration curve that converts Hounsfield units (HU) into carbon relative stopping power (RSP).

The work here presented is based on the results and contribution made to the following work:

- **Helium radiography combined with X-ray CT to determine patient-specific calibration curve for carbon cancer therapy**, Marta F. Dias, Charles-Antoine Collins-Fekete, Lennart Volz, Guido Baroni, Marco Riboldi, Joao Seco. Submitted to Physics in Medicine and

Biology, 2016 [DFV+16].

- **Improving carbon relative stopping power estimates for patients, using daily carbon imaging with pre-treatment single or dual energy CT**, Marta F. Dias, Charles-Antoine Collins-Fekete, David C. Hansen, Guido Baroni, Marco Riboldi, Joao Seco. International Workshop on Monte Carlo Techniques in Medical Physics, Quebec City, 2014 [DFC+14].

- **SU-E-J-83: Ion imaging to better estimate *in-vivo* relative stopping powers using X-ray CT prior-knowledge information**, Marta F. Dias, Charles-Antoine Collins-Fekete, Marco Riboldi, Paul Doolan, David C. Hansen, Guido Baroni, Joao Seco. Medical Physics, 2014 [DFCR+14].

- **SU-E-J-37: Combining proton radiography and X-ray CT information to better estimate relative stopping power in a clinical environment**, Charles-Antoine Collins-Fekete, Marta F. Dias, Paul Doolan, David C. Hansen, Luc Beaulieu, Joao Seco. Medical Physics, 2014 [FCDD+14].

- **On-line relative stopping power optimisation using multiple angle proton radiography and SECT/DECT prior-knowledge information**, Charles-Antoine Collins-Fekete, Marta F. Dias, David C. Hansen, Luc Beaulieu, Joao Seco. International Workshop on Monte Carlo Techniques in Medical Physics, Quebec City, 2014 [FDC+14].

4.1 Patient-specific calibration curve with combined X-ray CT and charged particle radiography

The finite range of charged particles represents one of the main reasons for their usage in cancer therapy. With precise range calculations, it is theoretically possible to deliver precise dose distribution in the vicinity of organs at risks such as the spine and brainstem [SKB+14]. However, there still exists a large number of uncertainties affecting the range estimate inside the patient. In the clinical environment these uncertainties

are accounted for by increasing the target margins up to 3.5%±1mm [Pag12c]. Range uncertainties origin from various sources such as patient positioning, organ motion and beam fluctuations [KMS+14]. The major uncertainty in treatment planning comes from the fact that the beam range prediction is made using X-ray CT by converting the HU from the X-ray treatment planning CT into RSP [SPL96b] (section 1.6.1). As previously mentioned, the RSP of a material is defined as the ratio of the materials stopping power to that of water and the main unit used while computing charged particle range in a medium. The stopping power of a material is given by the ionization energy loss along the charged particle's path. It can be divided into two components: the electronic stopping power and the nuclear stopping power. The electronic stopping power can be computed by the Bethe-Bloch (equation 1.1 in section 1.2.1. The nuclear stopping power is due to the elastic collisions between the ion projectile and atoms from the target, larger the atomic number of the incident particle, larger is the energy loss due to these collisions. The range of a charged particle, *i.e.*, the Bragg peak position is only related to the electronic stopping power, however, the influence of the nuclear stopping power at high energies is almost null.

Through the RSP value, it is possible to compute the beams range which is necessary to position the Bragg Peak within the tumor contour. The RSP is approximately constant in energy and insensitive to the ion species (e.g. protons to carbons) given the same initial energy per nucleon [WWK+15, MSSM10].

A widely used method to determine the HU-RSP curve is the stoichiometric approach (section 1.6.1) [SPL96b]. This uses experimentally obtained RSP values for plastic materials and theoretical determined RSPs for human biological tissues. The method relies on every patient having the same chemical composition as determined by the theoretical values. However, differences in age, sex, diet, or health state result in variability of the chemical composition of tissues [YZP+12]. Therefore, the stoichiometric calibration is not patient specific and range prediction errors are expected. Yang *et al.* [YZP+12], showed that RSP uncertainties due

to this calibration procedure can be up to 5%.

To tackle this problem, charged particle radiography/CT has been proposed since it allows the computation of the RSP values without the need of a HU-RSP calibration curve (section 1.6.2). If both the entrance (E_i) and exit (E_f) energy of the incident particle are known, the WET, i.e the thickness of water that would cause the charged particle to lose the same amount of energy as it would lose in the traversed medium, can be computed by:

$$WET = \int_{E_f}^{E_i} \left(\frac{dE}{dx}\right)^{-1} dE \tag{4.1}$$

Where $\frac{dE}{dx}$ is the particle's stopping power in water. Assuming the image space is digitized and the particles path is known, equation 4.2 can be written as:

$$WET = \sum a_{ij} RSP_j \tag{4.2}$$

with a_{ij} being the length crossed by particle i in the voxel with RSP$_j$ (Figure 4.1). The reconstruction of individual radiographic projections allows for a 3D map of the patients RSP to be generated.

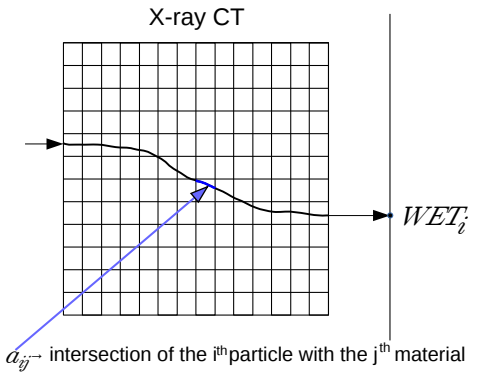

Figure 4.1: *Representation of how the system matrix is computed. By tracking the particle i along its path it is possible to calculate the total length crossed in each material j in the X-ray CT. The WET is then computed using equation 4.2.*

An important problem with carbon CT is the limited range of most commercial charged particle accelerators. These typically accelerate carbons to a maximum initial energy of 430 MeV/u corresponding to a

carbon range of less than 30cm in water. For larger patients and certain anatomical regions this is insufficient to completely cross the patient from all angles. But for reconstruction without data artifacts, full angular coverage is necessary. Furthermore, carbons suffer a large amount of nuclear interactions which lead to noisy data due to secondary particles hitting the detector and an increased dose to the patient. Nuclear interactions also greatly reduce the fluence of the incident beam. For instance, the fluence of a carbon beam crossing 16cm of water is reduced by almost half [Cus11]. Using protons tackle the aforementioned problems, however protons path reconstruction has larger errors leading to a reduction in spatial resolution quality [FVP+16]. Finally, charged particle CT is both costly (technology requirements) and time consuming (acquisition and reconstruction times).

Schneider *et al.* [SPB+05] proposed an optimization method to produce a patient specific RSP map without the need to obtain a full charged particle CT. The method consisted in combining the water equivalent map of the fluence-based radiograph with a digitally reconstructed radiograph generated from the X-ray CT through a calibration curve. The optimization method consisted in minimizing the difference between these two by modifying the calibration curve. Their work showed promising results, with an improvement in the mean range prediction from 3.6 mm to 0.4 mm for a dog patient. Doolan *et al.* [DTS+15] further pushed this method, showing that a single proton radiography could be used to generate a patient-specific calibration curve. However, they used a fluence integrated detector which only allows a straight line as estimation of the protons path. Both methods suffered from sensitivity to noise due to poor information on protons whereabouts within the patient. In 2016, Fekete *et al.* [FCBH+16] proposed an optimization method where the problem was viewed as a penalized linear square problem. They used single-event proton radiograph combined with the pre-treatment X-ray CT and a convex-conic optimization algorithm in order to obtain a new HU-RSP calibration curve. In their work, they considered cubic spline trajectories to retrieve the most likely location of protons throughout the patient. Their results demonstrated serious potential to increase the ac-

curacy of present RSP estimates.

The purpose of this work was to extend the work initially done by Fekete *et al.* [FCBH$^+$16] to heavier ions and to evaluate the feasibility of using a α radiography (α-rad) to create a patient-specific calibration curve to compute carbon and proton range. Strategies for selecting a set of materials out of the composition of the phantom to be used in the optimization algorithm were implemented and the impact of using multiple beam angles was also assessed. The optimization problem considered daily charged particle radiography, combined with X-ray CT. The obtained charged particle radiographies were obtained for protons, carbons and α particles. The obtained results were compared in order to assess which particle presents better results in the determination of proton/carbon range. Monte Carlo (MC) simulated charged particle calibration curves was computed and used as gold-standard. To the best of the authors knowledge, no work concerning patient-specific HU-RSP calibration curve with α-rad and c-rad has been done before, as well as determining which particle offers the best results.

4.2 Materials and Methods

MC simulations of 450 MeV/u proton, α and carbon particles were done to produce radiographies of the Gammex RMI-467 phantom and of two anthropomorphic phantoms (CIRS adult head and pediatric head). Each phantom geometry was obtained from the respective X-ray CT. The impact of using different methods to determine the ideal set of materials to be used in the optimization of the calibration curve as well as the number of angle projections to use in the optimizer were assessed. The gold standard calibration curve was obtained by using equation 2.4 and the stopping power tables from Geant4. For each material it was considered the mean value of the RSP for energies between 100MeV/u and 500MeV/u.

For each calibration curve produced in this study, a digitally reconstructed WET radiograph was produced using a projection of the RSP

along the beam direction. This allowed to estimate the impact of each calibration curve on the particle's range. Figure 4.2 shows the setup and the profile of the WET crossed for the slice of the phantom that included the densest material. The WET thickness difference with the reference curve was the metric used to compare the different techniques.

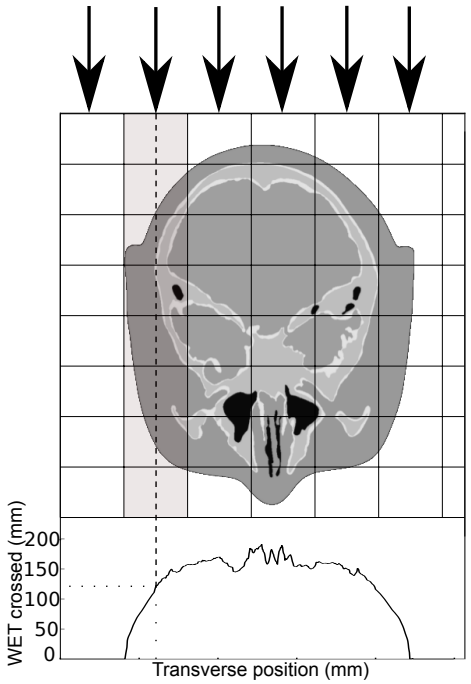

Figure 4.2: *A digitally produced charged particle radiography was obtained in the slice with the densest material. The initial projection direction is indicated by the black arrows. The total WET crossed is computed using equation 4.2.*

4.2.1 Monte Carlo simulations

Proton (p-rad), α-rad and carbon radiographies (c-rad) were generated using the MC simulation code Geant4 [AAA$^+$03] (v.4.10.2.p01). Standard processes included energy loss and straggling, multiple Coulomb scattering using the model from [Urb06] and elastic/inelastic ion interactions from Geant4 ion dedicated packages [LIK10]. The implemented method considered a phantom placed in between two detectors which record information about the particles energy, momentum and position before and after crossing the object. No detector effects were considered.

2×10^5 proton, carbon and α particles (E_{init}= 450 MeV/u) were propagated through the phantoms. The phantom geometry was based on the voxelized X-ray CT geometry acquired from the CT scans. In this study three phantoms were considered. First the Gammex RMI-467 was studied as a rapid way of characterizing the method in a simple phantom with few material present. For the Gammex phantom the X-ray CT was obtained through the ImaSim software [LDV13].

The Gammex is a solid-water cylinder (radius of 16.5 cm) with 16 cylindrical inserts (radius of 1.4cm) of tissue equivalent plastic material. Their chemical composition and density were taken from Landry *et al.* [LSG13].

Both, the second and third phantom were anthropomorphic. The CIRS pediatric head phantom was then studied to introduce complexity in the geometry of the phantom while keeping the number of materials relatively low. The CIRS pediatric head phantom is composed of 7 tissue-equivalent plastic materials. Finally, the CIRS adult head phantom was used since it comes closest to a clinical scenario. The adult CIRS head contains more than 3000 different HU values due to noise from the X-ray CT. The X-ray CTs of both CIRS anthropomorphic phantom were acquired through the Massachusetts General Hospital (MGH) X-ray CT machine. The material composition of each anthropomorphic phantom was extracted as described by Fekete *et al.* [FCBH$^+$16].

From the X-ray CT, it is obtained the HU value of each voxel. This can be converted into relative electron density (ρ^e_{rel}) and used to compute the mass density (ρ) of a material which is necessary to create Geant4 material list. The mass density can be computed as follows:

$$\rho = \frac{\rho^e_{rel}\rho^{water}N_g^{water}}{N_g} \rightarrow \quad N_g = \sum_i N_g^i = N_A \sum_i \frac{w_i Z_i}{A_i} \tag{4.3}$$

where N_g is the number of electrons per unit volume, N_A is the Avogadro's number Z_i and A_i are the atomic number and atomic weight of

Table 4.1: *Chemical composition of the materials used as reference for the Monte Carlo simulations [WW86, WWH87]. Materials for HU within the described range are interpolated in between the closest defined materials.*

Material Name	HU	H	C	N	O	Ca	P	I [eV]	ρ_e	ρ
Lung Deflated	-741	10.4	10.6	3.1	75.7	0.0	0.2	74.54	0.258	0.26
Adipose Tissue 3	-98	11.6	68.3	0.2	19.9	0.0	0.0	63.06	0.933	0.93
Adipose Tissue 1	-55	11.2	51.9	1.3	35.6	0.0	0.0	66.14	0.970	0.97
Mean Male soft tissue	5	10.5	25.6	2.7	60.2	0.0	0.2	72.3	1.016	1.02
Muscle Skeletal 1	40	10.2	17.3	3.6	68.7	0.0	0.2	73.69	1.040	1.05
Muscle Skeletal 2	43	10.3	14.4	3.4	71.6	0.0	0.2	74.03	1.043	1.05
Skin 1	72	10.1	25.2	4.6	59.9	0.0	0.1	72.25	1.0 84	1.09
Connective Tissue	100	9.5	21.0	6.3	63.1	0.0	0.0	73.79	1.103	1.12
Sternum	385	7.8	31.8	3.7	44.1	8.6	4.0	81.97	1.211	1.25
Humerus Spherical Head	538	7.1	38.1	2.6	34.3	12.2	5.6	85.43	1.279	1.33
Femur Total Bone	688	6.3	33.4	2.9	36.3	14.4	6.6	90.24	1.355	1.43
Cranium	999	5.0	21.3	4.0	43.8	17.7	8.1	99.69	1.517	1.61
Cortical Bone	1524	3.4	15.6	4.2	43.8	22.6	10.4	111.63	1.781	1.92

the ith element and w_i is its proportion by weight.

For each HU from the CT, an atomic composition was assigned. The atomic composition of individual voxel was derived from the set of materials detailed in Table 4.1. These materials were used as pivot point for defining HU materials. For voxels whose HU was between two pivots, composite materials were assigned based on linear interpolation between these pivots.

4.2.2 Determination of the patient specific calibration curve

The HU-RSP optimization problem can be formulated as a linear least squares problem:

$$\text{argmin}_x ||A\vec{x} - \vec{b}||_2^2 \tag{4.4}$$

The system matrix A is a $n \times m$ matrix which contains the length crossed in material i by particle j - a_{ij} (Figure 4.1). $\vec{x}$ is a m-dimensional vector which contains the m RSP values which are connected to the m

HU values of the X-ray CT. $\vec{b}$ is the projection data (ion radiography) which represents the WET crossed by the $i-th$ particle. $||.||_2^2$ is the squared l_2 norm. The WET values of the projection vector is obtained by solving the integral in equation 4.1.

By solving Equation 4.4 a patient-specific mapping of RSP to HU is obtained. To solve this optimization problem the linear least square function of Python's *numpy* package was used [com16]. The performance of the optimization was assessed by computing the relative error $\left(\frac{RSP_{opt}-RSP_{ref}}{RSP_{ref}}\right)$ of each obtained RSP value (RSP_{opt}) to the reference (RSP_{ref}). The reference RSP values were acquired directly via the Geant4 simulation (see section 4.2.1) through the Bethe-Bloch equation. The absolute difference between the optimized RSP and the reference in the WET crossed was also calculated. The optimization algorithm was run 10 times on different radiography in order to determine the statistical stability and variance of the solution.

4.2.3 Reconstructing the particles trajectory and computing the system matrix

A precise knowledge of the particle whereabouts throughout the patient is paramount to the presented technique, represented above in the system matrix by the parameter a_{ij}. By tracking each particle along its path through the X-ray CT, it is possible to retrieve information about the total length crossed in each material. This is done using a hull-detection algorithm and the optimized cubic spline path estimate, explained in chapter 2, section 2.2 [FCDD$^+$15b]. The hull-detection algorithm seeks for an approximate hull, so that the particle's path is only computed inside of that hull, *i.e.* the object of interest. To do so, since prior-knowledge is available, *i.e.* the X-ray CT, the particle is projected using a straight path to the hull entrance and retro-projected to the hull exit. The hull was defined as the voxel whose HU values were superior to -995HU, *i.e*, soft tissue.

4.2.4 Chemical composition

The stoichiometric method assumes inaccurately that the chemical composition of tissues, represented by the materials in the calibration curve, is constant among every patient. To validate the stability of this technique against such potential uncertainties, the chemical composition of the materials was varied using definition from various databases. This intends to represents inter-patient tissue variations. Precisely, the chemical composition of brain tissue suggested by Laundry *et al.* [LSG13] (Table 4.1) was altered in the pediatric head to the chemical composition proposed by Watanabe *et al.* [Wat99]. Although the brain HU value is identical, varying the tissue composition should leads to different RSP values and the optimization method should result in different calibration curves. A c-rad, α-rad and p-rad were obtained for both the initial and the altered chemical compositions in the pediatric head and the optimization method was applied in both cases.

4.2.5 Tissue segmentation

The heterogeneity of the human body and the intrinsic CT noise lead to a large set of HUs and therefore RSPs. Optimizing a large number of RSP values lead to a large and sparse system matrix (A) which causes statistical, memory storage and time consuming problems. Therefore, it is important to reduce the HU set of values present in the patient X-ray CT to a smaller sample.

In this work three approaches were considered in order to reduce the size of RSP values to be optimized. The first method uses the probability density function of the HU values present in the X-ray CT. The process of mapping a large set of values into a smaller one is generally irreversible resulting in loss of information and therefore introduces distortion into the new HU set that cannot be eliminated [Kul99]. However it can be minimized: Consider a M -level quantizer, *i.e*, our HU sample will be represented by M values. The most common distortion measure is given by the mean squared error, hence, the distortion can be defined as :

$$D = E[(x - Q(x))^2] = \int_{-\infty}^{\infty} (x - Q(x))^2 f(x) dx = \sum_{k=1}^{M} \int_{-b_k}^{b_k} (x - y_k)^2 f(x) dx \tag{4.5}$$

The quantizer Q is defined by $Q(x) = y_k$, where y_k are the new sampled HU values for the *k-th* interval. $f(x)$ represents the probability density function of the HU in the X-ray CT. x represents the initial complete set of HU. D is the mean squared error over every interval defined by the boundaries b_k. In order to obtain the [$\mathbf{y_k}$,$\mathbf{b_k}$] set that minimizes the mean squared error D, the Powell minimization algorithm [Pow64] was used with equation 4.5 as a cost function.

The second method uses the *k-means* cluster method from the Python package *sklearn* [sld16]. The k-means cluster algorithm takes as input the CT slice and M as the number of clusters, *i.e* the number of HU to be optimized. The output is a set of M cluster centroids that is the set of HU values to be optimized for in computing the calibration curve. All points within a cluster are closer in distance to their centroid than they are to any other centroid. This method was applied into the X-ray CT slice that comprised the densest material.

For comparison, a third and final method was implemented simply considering M evenly spaced values out of the HU set. Via each of the implemented methods a new set of HU values was obtained. Thresholds on the X-ray CT was applied taking into account the obtained set. The limits of those thresholds are the mid points between two consecutive HU values from the new set. The performance of the different segmentation methods was assessed by comparing the relative and absolute errors in the obtained calibration curves. For most of this study, 30 HU/RSP intervals were considered, representing about 1% of the total HU in the CIRS head. The impact of using different numbers of RSP intervals was assessed by using the clustering method with $M = [10, 30, 150]$.

For the tissue segmentation only α-rad was considered.

4.3 Results

All the obtained results present filtering, *i.e*, particles that were greatly deflected were not considered in the optimization process. Filtering out particles whose trajectories were greatly deflected ensures a better path estimation, reducing errors. However, as drawback more particles have to be considered and hence longer computation times.

4.3.1 Optimization accuracy on the Gammex RMI-467 phantom

A c-rad, α-rad and p-rad were obtained for the Gammex phantom. The optimization method without segmentation (since the set of HU is small) was applied to the measured data and the results are presented in Figure 4.3. The obtained calibration curves for all particles were compared with the reference curve. The optimization method provided results with relative error under 2.6% for α, under 2.5% for carbon and under 1.7% for proton over the whole HU range (middle graph in Figure 4.3). The absolute mean relative errors over the whole HU range were, $0.41\pm0.48\%$, $0.55\pm0.71\%$ and $1.08\pm0.71\%$ for proton, α and carbon respectively.

For c-rad, the absolute error between the optimized WET and the reference WET was below 2.0 mm. If a p-rad was used as basis for the optimization algorithm, this could be reduced to less than 0.5 mm (Figure 4.3, bottom). α-rad introduced an error under 1.5mm.

All, carbon, α and proton calibration curves presented larger errors in the soft tissue area compared to the rest of the HU range. It is important to state that even though the Gammex phantom is widely used to compute clinical calibration curves, it does not represent a human-like case due to its geometry and composition. The larger errors in the soft tissue area can be explained by the fact that the Gammex phantom consists of many materials. There is a strong possibility of redundancy when determining the RSP from the optimization algorithm, which could be possibly minimized by using multiple angle optimization as it will be

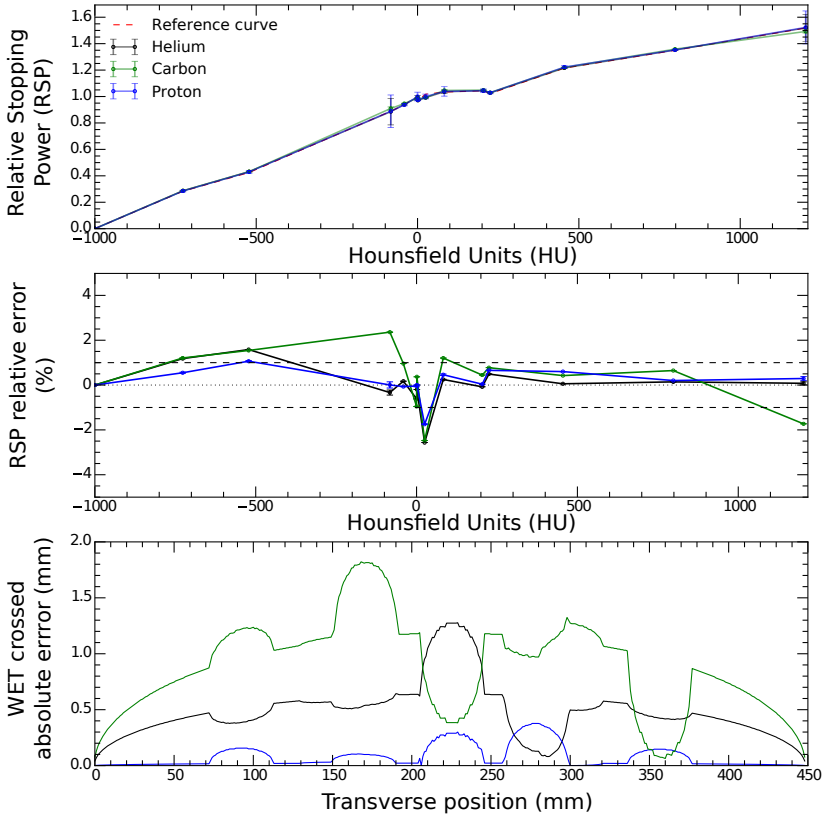

Figure 4.3: *Top: Optimized calibration curves obtained from proton, α (helium) and carbon radiographies. The dashed red line is the MC reference calibration curves for the Gammex phantom. Middle: Relative error between the MC reference and the optimized curves. The dashed lines represents 1% error and the dotted line 0% error. Bottom: Absolute error in WET crossed between the crossed WET calculated via the MC reference curve and via the calibration curves obtained via p-rad, α- and c-rad. The crossed WET is computed as shown in Figure 4.2.*

shown for the CIRS adult head.

4.3.2 Impact of the chemical composition variation on the optimization accuracy using the CIRS pediatric head

The CIRS pediatric head calibration curves were all obtained using a single angle projection. Although the material diversity is still small in the CIRS pediatric head, the tissues are chosen to represents human-like tissues and the geometry is closer to a clinical scenario. Radiographies were obtained for proton, α and carbon and the optimization method was used to compute the HU-RSP calibration curves as before. The results are presented in Figure 4.4-a. The relative difference to the reference calibration curve was below 2.1% for p-rad, 1.4% for the α-rad whereas they were below 0.7% for the c-rad. The absolute mean relative difference was: 0.43 ± 0.64 for protons, 0.29 ± 0.44 and 0.40 ± 0.19 for carbons. The absolute error in total WET crossed was below 0.2 mm using the α-rad, under 1.0 mm using c-rad and below 0.4mm for p-rad (Figure 4.4a bottom).

As mentioned before the chemical composition of a tissue might change in between patients. Therefore, to simulate this variability, the chemical composition of the brain tissue in the pediatric head was altered in between two reference sources resulting in a 2.3% and 1.2% shift in its RSP value (top and middle graph in Figure 4.4-b). This change in composition was accounted for in the optimized curves and presented a deviation to the reference below 1% for all charged particles radiographies (Figure 4.4b, middle graph). The results in the calculation of the WET crossed were similar to the ones obtained without the chemical composition change. In a scenario where a calibration curve is used across the board for every patient, *i.e.* in this case the perfect calibration curve obtained from MC without the chemical composition change (here referred as clinical curve), to compute the WET crossed, the total error is below to 2.5 mm (Figure 4.4b, bottom). These results demonstrates that the proposed technique account for chemical composition change which are aimed to represent inter-patient tissue variation.

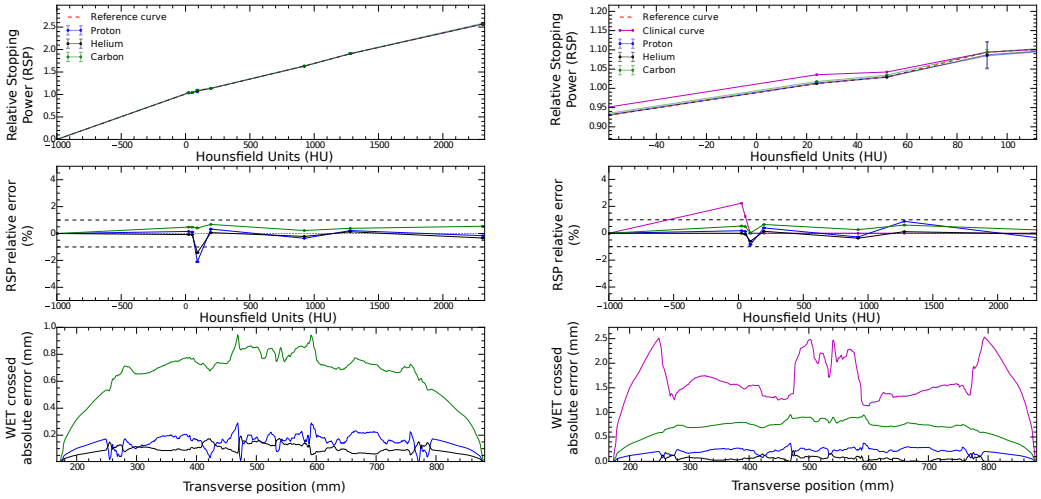

(a) *Results obtained for the CIRS pediatric head.*

(b) *Results obtained for the CIRS pediatric head with chemical change.*

Figure 4.4: *For both a) and b): Top: Calibration curves derived from the MC reference and optimized curves based on proton, α and carbon radiographies. Middle: Relative RSP deviation from the reference MC curve. Bottom: Absolute error of the WET crossed calculated using the method in Figure 4.2. In b) the optimization was done after introducing a change in the chemical composition of the material. The "clinical curve", represents the calibration curve determined with unaltered chemical composition, the one depicted (Figure 4.4a).*

4.3.3 Impact of the tissue segmentation technique on the optimization accuracy using the CIRS adult head

The CIRS adult head phantom represents the closest simulation to a clinical scenario. This section focus solely on the results based on the optimization from an α-rad for simplicity reasons.

As stated earlier, the CIRS adult head phantom consists of more than 3000 HU values and related RSP values to optimize. It is important to reduce this number of materials to improve the statistical reliability of the optimizer and accelerate it. Furthermore, a proper segmentation may help reduces the effect of X-ray CT noise expected in a clinical environment. Three segmentation methods were used to tackle this problem, as described in 4.2.5. Results for choosing 30 intervals tissues to represents the CT are presented in Figure 4.5.

The clustering method shows the smallest relative RSP errors (below 2%) for HUs between -200 and 1200. This led to smaller errors when calculating the WET crossed (Figure 4.5, bottom). The maximum error was below 0.90 mm for the clustering method, below 6 mm when using a probability density function based distortion and below 7 mm for the method using evenly spaced points in the original HU set. Since best results were obtained using the clustering method, this approach was used while evaluating the impact of the number of tissue intervals used to represent the CT data.

4.3.4 Impact of the number of optimized tissues on the optimization accuracy

In Figure 4.6, the impact of the size of the sample on the calibration curve is shown. It is seen that for the smallest number of RSP intervals (M=10), the relative difference (Figure 4.6-middle) is larger than 4% leading to maximal errors in calculated WET crossed of 7.5 mm. These errors could be reduced to below 0.90 mm by increasing the size of the sample to 30 RSPs. A large sample of RSPs led to an increase in the stan-

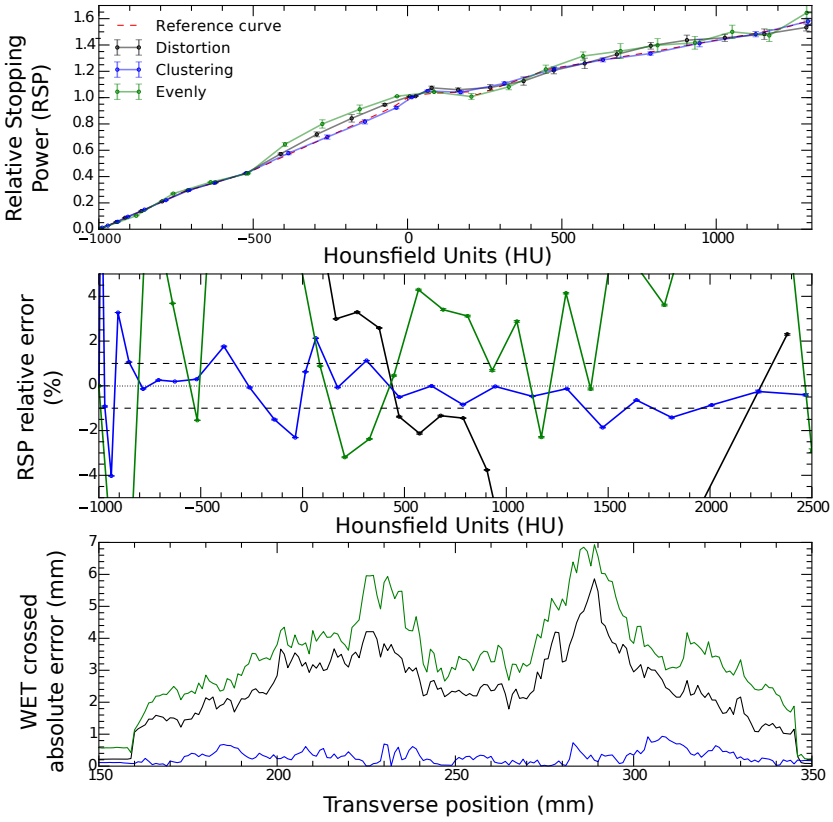

Figure 4.5: *Results for the CIRS head phantom, using 30 HU bins. Top: Calibration curves using the MC reference and the optimization method employing three different sampling methods based on a α-rad. Middle: Relative RSP errors between reference (MC data) and the optimized calibration curves. Bottom: The absolute error in WET crossed using the method in Figure 4.2.*

dard deviation of each RSP value and in fluctuations in between points of the calibration curve as it is seen in the topmost and middle graph in Figure 4.6. For a size of 150 RSPs, the maximum error in calculating the WET crossed was 0.83 mm. Since, the 150 presented larger osculations in the RSP values and the error in the WET crossed was not significantly reduced from 30RSP to 150RSP, for the next section only the clustering segmentation method with 30 RSP was considered.

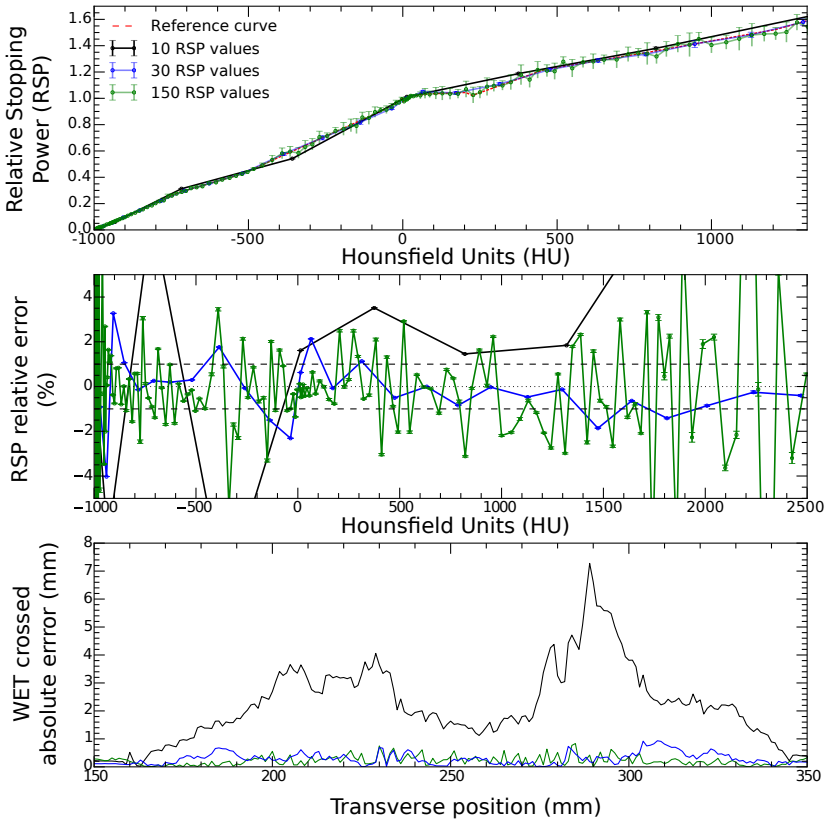

Figure 4.6: *Results for the CIRS head using the clustering method for tissue segmentation with different numbers of materials to be considered in the optimization algorithm. The topmost graph shows the calibration curves for a sample size of 10, 30 and 150 RSP. In the middle the relative differences to the MC reference curve are shown for the individual calibration curves. The bottom graph the total error of the calculated WET crossed is shown.*

4.3.5 Impact of the number of projections on the optimization accuracy

Figure 4.7 shows the impact of using a single, two or three projections (or angles) as input in the optimizer as a function of the RSP accuracy. Figure 4.7-a, shows the relative RSP difference between the optimized and the reference curves. For both protons and carbons, with more information given to the optimization algorithm, the calibration curve relative difference to the MC reference slightly decreased with increasing number of angles. This decrease is also seen in the WET crossed (Figure 4.7b). This difference is major when instead of one projection, two are used. The maximum WET crossed errors are reduced in 0.77mm and 0.17mm for protons and carbons respectively. For α-rad, multiple angle optimization does not introduce any improvements in the WET crossed. However, the absolute mean RSP difference is reduced when two angles are used. For one angle optimization, the absolute mean RSP difference is 3.70$\pm$4.81%, 1.30$\pm$2.18% and 1.92$\pm$2.74% for protons, helium and carbons, respectively. For two angle optimization: 2.76$\pm$4.60%, 1.17$\pm$1.50% and 1.85$\pm$2.46% for protons, helium and carbons, respectively. For three angle optimization: 2.21$\pm$4.43%, 1.19$\pm$1.52% and 1.43$\pm$2.42% for protons, helium and carbons, respectively.

4.4 Discussion

The aim of this study was to show that combining charged particle radiography with X-ray CT produces precise patient-specific calibration curve that can be used in carbon/proton radiotherapy. The calibration curves were obtained using the formulation first proposed by Fekete *et al.* [FCBH$^+$16] for protons. Whereas Fekete *et al.* used convex-conic optimization and considered proton radiographies, this work focused on proton, α and carbon radiographies where a simple linear least square optimization method with no penalization was used.

The method was investigated using three different phantoms: the Gammex RMI 467, which is widely used for determination of the HU-RSP curve, the CIRS pediatric head and the CIRS adult head. The proposed

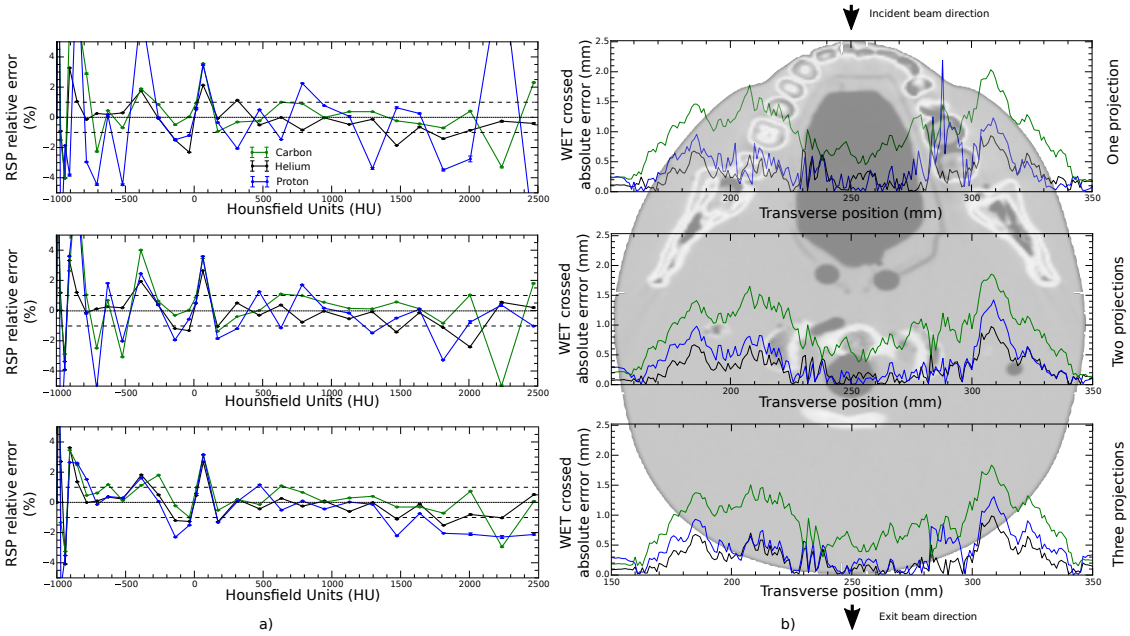

Figure 4.7: *Results for an optimization based on radiographies taken from multiple projections using the CIRS head with 30 HUs to be considered in the clustering method. The first row contains the results obtained from a single projection, the second from two projections and the third row the results obtained using three projections. a) shows the relative differences of the MC reference and the computed calibration curves based on different numbers of radiographies. b) shows the absolute error of the calculated WET crossed for the different calibration curves. The CIRS head phantom is superimposed and aligned with the transverse position in order to show the materials that results in the error of the calculated WET crossed. The arrow show the direction of how the beam was propagated.*

optimization method provided relative errors below 2.6% for all particles when determining the Gammex's RSP values (Figure 4.3 middle). The optimized curves were used to compute the absolute error of the total WET crossed, which can be used as a reference for the errors when computing the carbons range (Figure 4.2). The results were compared to the total WET crossed calculated using the calibration curve obtained from the perfect knowledge of the MC simulation. In summary, for the Gammex, the errors on the total WET crossed were below 2.0 mm. The lowest errors were obtained for p-rad, which provided errors under 0.5mm.

The CIRS pediatric head, which contains 7 tissue-like materials and air, was then used to validate the proposed method in a complex geometry. The HU-RSP calibration curves deviation from the perfect calibration curve were below 2.1% (middle Figure 4.4a) for all particles over the whole range of HUs.

A major problem of across-the-board calibration curves are the disregard towards inter-patient tissue variation. The method proposed here has been shown to solve this problem by using patient-specific data. To prove this, the brain tissue composition was altered (purple curve, middle Figure 4.4b) in between two reliable human tissue database. This change resulted in differences of up to 2.3% with the reference calibration curve obtained for the unaltered chemical composition and a maximal WET error of 2.5 mm. By acquiring a charged particle radiography, independent on the particle type, these differences were reduced to 1.0%, leading to a maximal error of the calculated WET below 1.0 mm. Using a α-rad, the error could be further reduced to below 0.2 mm. These results show that the proposed method produces precise calibration curves in the case of inter-patient tissue variation.

To investigate the methods usability for complex, clinical problems, the CIRS adult head was used. This phantom consists of more than 3000 HU values. The large number of HU values is common for a X-ray CT due to noise and needs to be reduced for both time and statistics reasons. Therefore, it is necessary to segment the X-ray CT in order to obtain a

list of representative HUs which then can be used to obtain the HU-RSP calibration curve.

In this work, it has been established that the optimal method to obtain a patient-specific calibration based on an initial clinical X-ray CT is to first use a $k-means$ clustering method to sample the X-ray CT in approximately 30 tissues and to use as many projections as possible to do the optimization. It has however been shown that a single projection gives reliable results with a maximal error throughout the phantom of 2.2 mm for p-rad, below 0.93mm for α-rad and under 2.03mm for c-rad.

The calculated WET crossed, presented in all the results, represents a summed error over the whole patient and exaggerates what is expected in a clinical beam scenario that stops in the middle of the patient. In addition, these errors represents the worse case scenario as they were seen for charged particles crossing the patient densest materials, *i.e.* the tooth and mandibular bone (Figure 4.7-b). In a realistic clinical plan, the irradiation angles and beam energies are usually selected in order to avoid such materials and those errors are therefore not expected to appear.

DECT has been proposed as an alternative method to acquire the patient RSP maps [YVC$^+$10]. Results using DECT have been promising in the RSP computation (with range uncertainties of 1.9%-2.3% [YVC$^+$10]). However, DECT has the disadvantage that it does not image the patient directly in the treatment position, and does not account for morphology change that might occur between planning and treatment. Furthermore, DECT only allows the computation of the electronic stopping power disregarding the impact of the nuclear stopping power in carbon range calculation, which could cause some severe range uncertainties.

4.4.1 The effect of the charged particle type in range computation

The proposed method of using charged particle radiography combined with pre-treatment X-ray CT proved to produce precise calibration curves

independently of the particle type. In opposition to carbon/proton particle CT, this approach does not require long acquisition and computation times and furthermore, is less limited by energy/dose constraints since it is not necessary to irradiate the body at different angles.

The maximum error in terms of WET crossed was of 2.2mm obtained with p-rad for one angle projection of the CIRS adult head. WET crossed errors for α-rad were all under 1.5mm. One should bear in mind that the WET crossed error is highly dependent on the materials that are being crossed. This means that, for example, if a beam crosses two materials whose RSP values were over and underestimate, the total error is going to be small since the errors compensate. If the beam only crosses overestimated RSP values the error is greater. Having this in mind, it should be done a comparison on the absolute mean difference between the optimized RSP and the gold standard.

Considering the absolute mean difference between the optimized RSP and the gold standard, α-rad presented the smaller errors as well. For all cases the absolute mean relative difference was under $1.3\pm2.18\%$. As mentioned in Fekete *et al.* [FVP$^+$16], α particles were found to be the optimal particles for charged particle imaging, since they offer better path estimation results (for the same energy per mass), leading to images with superior spatial. This might play an important role if image registration is necessary. In addition, p-rad requires more severe filters due to the larger effect of multiple coulomb scattering. This leads to loss of information, which in clinical environment is limited.

Furthermore, one needs to consider the aforementioned reasons for using α-rad instead of c-rad. Amongst those reasons, the nuclear fragmentation noise, the larger fluence reduction of the carbon beam in the patient, the technical difficulties to produce carbon with clinically significant range and the increase dose deposition justify the use of α-rad to obtain a carbon calibration curve.

Nonetheless, it is worth to mentioned that all the obtained results

showed range errors under of 2.2 mm for all phantoms. This value is below the clinically added margins [KHF+13].

The major drawback of this method, independently of the particle type, is that it is limited by patient motion, which can cause a displacement of the acquired RSP map to the X-ray CT HU map. Further investigation that tackles this problem and an experimental validation of the proposed method are necessary. However, these were out of the scope of this work.

4.5 Conclusion

This study aimed to use charged particle radiography combined with X-ray CT to determine a HU-RSP calibration curve to be used in proton/-carbon therapy. Different strategies to segment and select the materials used to create the HU-RSP calibration curve were assessed, showing that only 1% of the HU values of the X-ray CT and one radiography were necessary for the optimization method to provide accurate results. The results were compared for three different charged particle radiography types: proton (p-rad), α (α-rad) and carbon (c-rad). The results suggest that α-rad might be the method of choice for future carbon and proton treatment planning.

CHAPTER 5

Conclusions and future perspectives

THERE is a growing interest in using charged particles for cancer treatment. Such treatments have already proved that high-dose delivery can be achieved while sparing OARs. However, correct and precise knowledge of the range of charged particles is necessary in order to place the irradiation beam(s) within the tumor contours.

Currently in clinical practice, the range of charged particle beams (carbons and protons) is determined by converting the HU from the patient X-ray CT into RSP. The RSP of a charged particle is considered to be independent of the charged particle type and its energy.

The conversion process from HU to RSP introduces uncertainties in the calculation of a charged particle's range. Large efforts have been placed in charged particle imaging as a possible solution to reduce range uncertainties. In this thesis, it was proposed and investigated new alternatives to reduce range uncertainties. This alternatives were devolved with the aim to be applied in carbon therapy, however they are traversal

to all charged particle types.

The RSP calculation for the HU-RSP calibration curve assumes that tissues have a known chemical composition. However, there are different literature sources leading to errors in the calculation of the RSP. In chapter 2 the results of a method which optimized the elemental I-values using experimentally measured RSP were presented. The results suggested that this optimization should be added to the calibration curve procedure, in order to obtain a better estimation of the HU-RSP calibration curve.

The remaining work of this dissertation was focused in methods which relied on charged particle imaging principles. One problem in charged particle imaging is that, as opposed to X-rays, charged particles do not travel straights paths. The reconstruction algorithms that have been developed for X-ray imaging consider straight line trajectories. If this assumption is considered in practical implementation, low resolution images and range errors may arise. Therefore, in chapter 2, section 2.2, the results of a phenomenological formalism for charged particle path estimation were presented. This formalism used the cubic spline path, but accounted for the effect of the magnitude of the direction vectors. The results showed that both carbons and protons trajectories with the proposed CSP trajectories presented lower errors than using the straight line assumption. By having a better path estimation errors in range calculation can be reduced, as it will be shown in chapter 4, where each charged particle is tracked along the phantoms.

Chapter 3 presented a technique which allowed tumor edge detection with a few irradiation beams and low dose to the patient. The method consisted in detecting the difference between the intensity of the multiple Bragg peaks in the range detector after an interface was irradiated by at least two high energy carbon beams. By knowing where edges are positioned, errors in irradiating organs at risk can be avoided. This method only considered carbon beans, since these present a sharper Bragg peak. However, this method should be tested using both protons and helium

particles.

Finally, chapter 4 proposed the use of charged particle radiography (p-rad, α-rad and c-rad) combined with X-ray CT to determine a patient specific calibration curve. The results of using this method were promising with maximum errors under 2.2mm in a worst case scenario. The results also shown that α particles (helium) might be the ideal particle for charged particle imaging. Moreover, the proposed method does not require imaging reconstruction methods only requiring data from a single projection. This will tackle the problem of limited angles, reconstruction time and computational effort.

Currently, charged particle imaging is mainly limited by technological challenges. These can be related to the acquisition system, *i.e.* the detectors, and/or the irradiation/acceleration system. The energies required for carbon imaging for all anatomical sites are not reached in a clinical environment (maximum of 30WET cm can be crossed). Furthermore, most detection systems have been focused in proton imaging, *i.e.* single event detection. Carbons present a higher total reaction cross section than α particles and protons. Consequently, the fraction of carbons reaching the exit detector is greatly reduced and the percentage of secondaries hitting the detector is very high, leading to a noisy output, mainly if single event detectors are considered.

Using a range detector avoids the secondaries problem. However, several issues are still to be considered, such as the energy, multiple peak detection, the loss of beam fluence and the higher those delivered to the patient.

The work presented in this thesis showed evidence that the future of reducing range uncertainties in charged particle (both with protons and carbons) therapy might pass by using alternatives to charged particle CT. Avoiding the need of multiple angle acquisition, larger reconstruction times and computational effort. The results showed in chapter 4 are of great importance, since they suggest the use of helium radiogra-

phy as the future for both proton and carbon therapy range uncertainties. This conclusion is supported also by the results found in Fekete *et al.* [FVP+16], where it is shown that helium particles have the minimal root mean square error in their path estimation from protons and carbons.

Hence, helium based imaging will eventually enable *in-vivo* ion beam (proton and carbons) range calculations and support refinement of the HU-RSP calibration curve, without the need of high energetic beams and offering less scattering, MCS effects and beam fluence/dose to the patient.

Bibliography

[AAA+03] S. Agostinelli, J. Allison, K. Amako, Apostolakis, et al. Geant4 - a simulation toolkit. *Nuclear Instruments and Methods in Physics Research Section A: Accelerators, Spectrometers, Detectors and Associated Equipment*, 506(3):250–303, jul 2003.

[ASF12] Shinji Abe, Hitoshi Sato, and Tatsuya Fujisaki. Heavy ion CT system based range on measurement of residual distribution. *J. Med. Phys.*, 22:39–47, 2012.

[Att91] F. Attix. *Introduction to Radiological Physics and Radiation Dosimetry*. John Willey & Sons, 1991.

[Bic72] H Bichsel. Passage of charged particles through matter. *American Institute of Physics Handbook ed E D Gray (New York: McGraw-Hill)*, 1972.

[BS96] Thomas Bortfeld and Wolfgang Schlegel. An analytical approximation of depth - dose distributions for therapeutic proton beams. *Phys. Med. Biol.*, 41(8):1331–9, 1996.

[CC09] Alexander W. Chao and Weiren Chou, editors. *Reviews of Accelerator Science and Technology, Volume 2, Medical Applications of Accelerators*. World Scientific, 2009.

[CK76] A M Cormack and A M *et al.* Koehler. Quantitative proton tomography: preliminary experiments. *Physics in Medicine and Biology*, 21(4):007, jul 1976.

[com16] The Scipy community. numpy.linalg.lstsq. *SciPy.org*, Aug 2016. URL: `http://docs.scipy.org/doc/numpy/reference/generated/numpy.linalg.lstsq.html`.

[Cre05] Paulo Crespo. *Optimization of In-Beam Positron Emission Tomography for Monotoring Heavy Ion Tumor Therapy*. PhD thesis, Technische Universität Darmstadt, 2005.

Bibliography

[Cus11] Daniel Cussol. Nuclear Physics and Hadrontherapy. *LPC Caen, ENSICAEN, Universite de Caen Basse-Normandie, IN2P3/CNRS*, 2011.

[CVS+13] Kenneth Clark, Bruce Vendt, Kirk Smith, John Freymann, Justin Kirby, Paul Koppel, Stephen Moore, Stanley Phillips, David Maffitt, Michael Pringle, Lawrence Tarbox, and Fred Prior. The Cancer Imaging Archive (TCIA): Maintaining and Operating a Public Information Repository. *Journal of Digital Imaging*, 26(6):1045–1057, dec 2013.

[DDFS14] P Doolan, MF Dias, CA Fekete C, and J Seco. SU-E-T-550: Range Effects in Proton Therapy Caused by Systematic Errors in the Stoichiometric Calibration. *Medical Physics*, 41(6):354–354, jun 2014.

[DFB+16a] MF Dias , CA Fekete C, G Baroni, J Seco, and M Riboldi. PO-0822: Tumor margin estimation by multiple Bragg peak detection in carbon ion therapy. *Radiotherapy and Oncology*, 2016.

[DFB+16b] MF Dias, CA Fekete C, G Baroni, M Riboldi, and J Seco. Investigation of tumor edge detection using multiple Bragg peak detection in carbon therapy. *Submitted to Med. Phys.*, 2016.

[DFC+14] MF Dias, CA Fekete C, David C. Hansen, Marco Riboldi, and Joao Seco. Improving carbon relative stopping power estimates for patients, using daily carbon imaging with pre-treatment single or dual energy CT. *International Workshop on Monte Carlo Techniques in Medical Physics*, 2014.

[DFCD+16] P Doolan, CA Fekete C, MF Dias, Thomas A Ruggieri, Derek D'Souza, and Joao Seco. Inter-comparison of relative stopping power estimation models for proton therapy. *Phys. Med. Biol.*, pages 7–10, 2016.

[DFCR+14] MF Dias, CA Fekete C, M Riboldi, P Doolan, D Hansen, G Baroni, and J Seco. SU-E-J-83: Ion Imaging to Better Estimate In-Vivo Relative Stopping Powers Using X-Ray CT Prior-Knowledge Information. *Medical Physics*, 41(6):174–174, jun 2014.

[DFV+16] MF Dias, CA Fekete C, Lennart Volz, Guido Baroni, Marco Riboldi, and Joao Seco. Helium radiography combined with X-ray CT to determine patient-specific calibration curve for carbon cancer therapy. *Submitted to Phys. Med. Biol.*, 2016.

[DRS+15] MF Dias, Marco Riboldi, Joao Seco, Ines Castelhano, Andrea Pella, Alfredo Mirandola, Luis Peralta, Mario Ciocca, Roberto Orecchia, and Guido Baroni. Scan path optimization with/without clustering for active beam delivery in charged particle therapy. *Physica Medica*, 31(2):130–136, 2015.

[DS13] Depauw, N and Dias, MF and Rosenfeld, A and J Seco. Ion Radiography as a Tool for Patient Set-up & Image Guided Particle Therapy: A Monte Carlo Study. *Technology in Cancer Research and Treatment*, 2013.

[DSBR16] MF Dias, J Seco, G Baroni, and M Riboldi. SU-F-J-204: Carbon Digitally Reconstructed Radiography (CDRR): A GPU Based Tool for Fast and Versatile carbon imaging Simulation. *Med. Phys.*, 2016.

[DTS+15] P J Doolan, M Testa, G Sharp, E H Bentefour, G Royle, and H-M Lu. Patient-specific stopping power calibration for proton therapy planning based on single-detector proton radiography. *Physics in medicine and biology*, 60(5):1901–17, 2015.

[Eid04] S Eidelman. Passage of particles through matter. *Physics Letters*, 1(B592), 2004.

[FCBH+16] CA Fekete C, S Brousmiche, D C Hansen, L Beaulieu, and J Seco. Pre-treatment patient-specific stopping-power by combining proton radiography and X-ray CT. *Phys. Med. Biol.*, 2016.

[FCDD+14] CA Fekete C, MF Dias, P Doolan, David C Hansen, L Beaulieu, and J Seco. SU-E-J-37: Combining Proton Radiography and X-Ray CT Information to Better Estimate Relative Proton Stopping Power in a Clinical Environment. *Medical Physics*, 41(6):163–163, jun 2014.

[FCDD+15a] CA Fekete C, P Doolan, MF Dias, L Beaulieu, and J Seco. TU-F-CAMPUS-J-02: Developing a Phenomenological Model of the Proton Trajectory Within a Heterogeneous Medium Required for Proton Imaging. *Medical Physics*, 42(6):3645–3645, jun 2015.

[FCDD+15b] CA Fekete C, Paul Doolan, MF Dias, Luc Beaulieu, and Joao Seco. Developing a phenomenological model of the proton trajectory within a heterogeneous medium required for proton imaging. *Physics in Medicine and Biology*, 60(13):5071–5082, 2015.

[FCSLJ16] CA Fekete C, Brousmiche S., Beaulieu L., and Joao Seco J. A maximum likelihood method for high resolution proton radiography/proton CT. *Phys. Med. Biol.*, 2016.

[FDC+14] CA Fekete C, MF Dias, David C. Hansen, Luc Beaulieu, and Joao Seco. Online relative stopping power optimisation using multiple angle proton radiography and SECT/DECT prior-knowledge information. *International Workshop on Monte Carlo Techniques in Medical Physics*, 2014.

[FKAEC09] Emmanouil Fokas, Gerhard Kraft, Hanxiang An, and Rita Engenhart-Cabillic. Ion beam radiobiology and cancer: Time to update ourselves. *Biochimica et Biophysica Acta (BBA) - Reviews on Cancer*, 1796(2):216–229, 2009.

[FVP+16] CA Fekete, L Volz, S Portillo, L Beaulieu, and J Seco. A theoretical framework to predict the most likely ion path in particle imaging. *ResearchGate*, 2016.

[Goi08] M. Goitein. *A Physcist's Eye View*. Springer, New York, 2008.

[Gro05] By Sven Oliver Grozinger. Particle beam application: on the way to optimum dose conformity. *Science Particle Therapy, Medical Solutions*, 2005.

Bibliography

[Gro16] Particle Therapy Co-Operative Group. Particle therapy facilities in operation, 2016. URL: http://www.ptcog.ch/index.php/facilities-in-operation.

[GSI11] Helmholtzzentrum für Schwerionenforschung GmbH GSI. Chair. Online, December 2011. URL: https://www.gsi.de/forschung/bio/chair_e.html.

[GYL+10] Michael F. Gensheimer, Torunn I. Yock, Norbert J. Liebsch, Gregory C. Sharp, Harald Paganetti, Neel Madan, P. Ellen Grant, and Thomas Bortfeld. In vivo proton beam range verification using spine {MRI} changes. *International Journal of Radiation Oncology*Biology*Physics*, 78(1):268 – 275, 2010. URL: //www.sciencedirect.com/science/article/pii/S0360301609036347, doi:http://dx.doi.org/10.1016/j.ijrobp.2009.11.060.

[HBC+78] K. M. Hanson, J N Bradbury, T M Cannon, R L Hutson, D B Laubacher, R Macek, M A Paciotti, C A Taylor, and Los Alamos Scientific. The application of protons to computed tomography. *IEEE Transactions on Nuclear Science*, NS-25(No. 1):657–660, 1978.

[HBK+82] K M Hanson, J N Bradbury, R a Koeppe, R J Macek, D R Machen, R Morgado, M a Paciotti, S a Sandford, and V W Steward. Proton computed tomography of human specimens. *Physics in medicine and biology*, 27(1):25–36, jan 1982.

[HBSS14] David C Hansen, Niels Bassler, Thomas Sangild Sørensen, and Joao Seco. The image quality of ion computed tomography at clinical imaging dose levels. *Medical physics*, 41(11):111908, nov 2014.

[HKM11] Yoshihiko Hatano, Yosuke Katsumura, and A. Mozumder, editors. *Charged Particle and Photon Interactions with matter, Recent Advances, Applications, and Interfaces*. CRC Press, Taylor and Francis Group, 2011.

[HTC+12] P Henriquet, E Testa, M Chevallier, D Dauvergne, G Dedes, N Freud, J Krimmer, J M Létang, C Ray, M-H Richard, and F Sauli. Interaction vertex imaging (IVI) for carbon ion therapy monitoring: a feasibility study. *Physics in medicine and biology*, 57(14):4655–69, jul 2012.

[ICR89] ICRU. Tissue Substitutes on Radiation Units and Measurement *Report 44*. *International Commission of Radiation Units and Measurements*, 1989.

[ICR92] ICRU. Photon, Electron, Proton and Neutron Interaction Data for Body Tissues (International report 46. *International Commission of Radiation Units and Measurements*, 1992.

[ICR93] ICRU. Stopping Powers and Ranges for Protons and Alpha Particles *ICRU Report 49 . International Commission of Radiation Units and Measurements*, 1993.

[Jan82] F Janni. Part 1 - proton range-energies tables, 1keV-10GeV. Energy loss, range, path length, time-of-flight, straggling, multiple scattering and nuclear interaction probability. *At. Data Nucl. Data Tables*, 27:147–339, 1982.

[Jer15] Martin Jermann. Particle Therapy Statistics in 2014. *Int J Particle Ther*, 2(1):50–54, 2015.

[JR14] O Jakel and P Reiss. The influence of metal artefacts on the range of ion beams. *Phys. Med. Biol.*, 52(3):635–44, 2014.

[JWSA14] K C Jones, A Witztum, C M Sehgal, and S Avery. Proton beam characterization by proton-induced acoustic emission: simulation studies. *Physics in Medicine and Biology*, 59(21):6549–6563, nov 2014.

[KFM+10] A. Kitagawa, T. Fujita, M. Muramatsu, S. Biri, and A. G. Drentje. Review on heavy ion radiotherapy facilities and related ion sources (invited). *Rev. Sci. Instrum*, 2010.

[KHF+13] Peter Kuess, Stephan Helmbrecht, Fine Fiedler, Wolfgang Birkfellner, Wolfgang Enghardt, Johannes Hopfgartner, and Dietmar Georg. Automated evaluation of setup errors in carbon ion therapy using PET: feasibility study. *Medical physics*, 40(12):121718, dec 2013.

[KMS+14] Ozhan Koybasi, Pankaj Mishra, Sara St James, John H Lewis, and Joao Seco. Simulation of dosimetric consequences of 4D-CT-based motion margin estimation for proton radiotherapy using patient tumor motion data. *Physics in medicine and biology*, 59(4):853–67, feb 2014.

[Koe68] A. M. Koehler. Proton Radiography. *Science*, 160(3825), 1968.

[KTB+15] Nils Krah, Mauro Testa, Stephan Brons, Oliver Jäkel, Katia Parodi, Bernd Voss, and Ilaria Rinaldi. An advanced image processing method to improve the spatial resolution of ion radiographies. *Phys. Med. Biol.*, in press, 2015.

[Kul99] Sanjeev R. Kulkarni. Sampling and Quantization. *Information Signals course notes from Priceton University*, Chapter 5(i):9–12, 1999.

[KWK16] Lauri Koivula, Leonard Wee, and Juha Korhonen. Feasibility of mri-only treatment planning for proton therapy in brain and prostate cancers: Dose calculation accuracy in substitute ct images. *Medical Physics*, 43(8):4634–4642, 2016. URL: `http://dx.doi.org/10.1118/1.4958677`, `doi:10.1118/1.4958677`.

[KWO07] Joanne H. Kang, Jan J. Wilkens, and Uwe Oelfke. Demonstration of scan path optimization in proton therapy. *Med. Phys*, 34, 2007.

[LDV13] Guillaume Landry, François DeBlois, and Frank Verhaegen. ImaSim, a software tool for basic education of medical x-ray imaging in radiotherapy and radiology. *Frontiers in Physics*, 1, 2013.

[LIK10] A. Lechner, V.N. Ivanchenko, and J. Knobloch. Validation of recent Geant4 physics models for application in carbon ion therapy. *Nuclear Instruments and Methods in Physics Research Section B: Beam Interactions with Materials and Atoms*, 268(14):2343–2354, jul 2010.

Bibliography

[Lin12] Ute Linz, editor. *Ion Beam Therapy*. Springer, 2012.

[LLS+06] Tianfang Li, Zhengrong Liang, Jayalakshmi V Singanallur, Todd J Satogata, David C Williams, and Reinhard W Schulte. Reconstruction for proton computed tomography by tracing proton trajectories: a Monte Carlo study. *Medical physics*, 33(3):699–706, 2006.

[Lom08] A J Lomax. Intensity modulated proton therapy and its sensitivity to treatment uncertainties 2: the potential effects of inter-fraction and inter-field motions. *Physics in medicine and biology*, 53(4):1043–56, feb 2008.

[LSG13] Guillaume Landry, Joao Seco, and Mathieu Gaudreault. Deriving effective atomic numbers from DECT based on a parameterization of the ratio of high and low linear attenuation coefficients. *Physics in Medicine and Biology*, 58(19):6851–6866, oct 2013.

[MDS+14] Shinichiro Mori, Lei Dong, George Starkschall, Radhe Mohan, and George T Y Chen. A serial 4DCT study to quantify range variations in charged particle radiotherapy of thoracic cancers. *Journal of radiation research*, 55(2):309–19, mar 2014.

[MKYK06] Chul-Hee Min, Chan Hyeong Kim, Min-Young Youn, and Jong-Won Kim. Prompt gamma measurements for locating the dose falloff region in the proton therapy. *Applied Physics Letters*, 89(18):183517, 2006.

[MMD+16] A Mairani, G Magro, I Dokic, S M Valle, T Tessonnier, R Galm, M Ciocca, K Parodi, A Ferrari, O Jäkel, T Haberer, P Pedroni, and T T Böhlen. Data-driven RBE parameterization for helium ion beams. *Physics in Medicine and Biology*, 61(2):888–905, 2016.

[MMRea69] H D Maccabee, U Madhvanath, M R Raju, and et al. Tissue activation studies with alpha-particle beams. *Physics in Medicine and Biology*, 14(2):304, apr 1969.

[MNA+07] H Muraishi, K Nishimura, S Abe, H Satoh, Y Takahashi, H Hara, S Hara, R Kawai, K Yokoyama, N Yasuda, T Tomida, Y Ohno, and T Kanai. Heavy Ion CT System Based on the Measurement of Residual Range Distribution : Improvement of the Optical Detector System. *IEEE Nuclear Science Symposium Conference Record*, pages 4354–4358, 2007.

[Mol47] Gert Moliere. Theorie der Streuung schneller geladener Teilchen I Einzelstreuung am abgeschirmten Coulomb-Feld 1. *Z. Naturforschg*, 2:133–145, 1947.

[MSSM10] Michael F Moyers, Milind Sardesai, Sean Sun, and Daniel W Miller. Ion stopping powers and CT numbers. *Medical dosimetry : official journal of the American Association of Medical Dosimetrists*, 35(3):179–94, jan 2010.

[MZK13] Shinichiro Mori, Silvan Zenklusen, and Antje-Christin Knopf. Current status and future prospects of multi-dimensional image-guided particle therapy. *Radiological physics and technology*, 6(2):249–72, jul 2013.

[OKMK04] Y Ohno, T Kohno, N Matsufuji, and T Kanai. Measurement of electron density distribution using heavy ion CT. *Nuclear Instruments and Methods in Physics Research Section A: Accelerators, Spectrometers, Detectors and Associated Equipment*, 525(1-2):279–283, jun 2004.

[ÖZB+15] Jakob Ödén, Jens Zimmerman, Robert Bujila, Patrik Nowik, and Gavin Poludniowski. Technical Note: On the calculation of stopping-power ratio for stoichiometric calibration in proton therapy. *Medical Physics*, 42(9):5252–5257, 2015.

[OzR12] OzRadOnc. Factors influencing the oxygen effect, August 2012. URL: `http://ozradonc.wikidot.com/rb:factors-influencing-radiation`.

[Pag12a] Harald Paganetti. *Proton Therapy Physics*. CRC Press, Taylor and Francis Group, 2012.

[Pag12b] Harald Paganetti, editor. *Proton Therapy Physics*. CRC Press, Taylor and Francis Group, 2012.

[Pag12c] Harald Paganetti. Range uncertainties in proton therapy and the role of Monte Carlo simulations. *Physics in Medicine and Biology*, 57(11):R99–R117, jun 2012.

[Par14] K Parodi. Heavy ion radiography and tomography. *Physica medica : PM : an international journal devoted to the applications of physics to medicine and biology : official journal of the Italian Association of Biomedical Physics (AIFB)*, 30(5):539–43, jul 2014.

[PBdB+99] P. Pemler, J. Besserer, J. de Boer, M. Dellert, C. Gahn, M. Moosburger, U. Schneider, E. Pedroni, and H. Stäuble. A detector system for proton radiography on the gantry of the Paul-Scherrer-Institute. *Nuclear Instruments and Methods in Physics Research Section A: Accelerators, Spectrometers, Detectors and Associated Equipment*, 432(2):483–495, 1999.

[PG00] H. Paganetti and M. Goitein. Radiobiological significance of beam line dependent proton energy distributions in a spread-out bragg pe. *Med. Phys*, 2000.

[Pow64] M. J. D. Powell. An efficient method for finding the minimum of a function of several variables without calculating derivatives. *The Computer Journal*, 7(2):155–162, feb 1964.

[RBG+13] I Rinaldi, S Brons, J Gordon, R Panse, B Voss, O Jäkel, and K Parodi. Experimental characterization of a prototype detector system for carbon ion radiography and tomography. *Physics in medicine and biology*, 58(3):413–27, 2013.

[RBJ+14] I Rinaldi, S Brons, O Jäkel, B Voss, and K Parodi. A method to increase the nominal range resolution of a stack of parallel-plate ionization chambers. *Physics in medicine and biology*, 59(18):5501–15, 2014.

Bibliography

[Rin11] Ilaria Rinaldi. Investigation of novel imaging methods using therapeutic ion beams. *PhD thesis*, page 162, 2011.

[Rob12] David Robin. An overview of next generation gantries. Online, July 2012. URL: `http://erice2011.na.infn.it/TalkContributions/Robin.pdf`.

[RS16] Arabinda Rath and Narayan Sahoo. *Particle Radiotherapy, emerging tecnology for treatment of cancer*. Springer, 2016.

[SBP+04] Uwe Schneider, Jurgen Besserer, Peter Pemler, Matthias Dellert, Martin Moosburger, Eros Pedroni, and Barbara Kaser-Hotz. First proton radiography of an animal patient. *Medical Physics*, 31(5):1046, 2004.

[SEJS06] Daniela Schulz-Ertner, Oliver Jake, and Wolfgang Schlegel. Radiation therapy with charged particles. *Semin Radiat Oncol, Elsevier Inc.*, 2006.

[SESE10] Dieter Schardt, Thilo Elsässer, and Daniela Schulz-Ertner. Heavy-ion tumor therapy: Physical and radiobiological benefits. *Reviews of Modern Physics*, 82(1):383–425, feb 2010.

[sit12] Ionization and cell damage. NDT Resource Center, August 2012. URL: `http://www.ndt-ed.org/EducationResources/CommunityCollege/RadiationSafety/theory/ionization.htm`.

[SK73] V. W. STEWARD and A. M. KOEHLER. Proton Radiographic Detection of Strokes. *Nature*, 245(5419):38–40, sep 1973.

[SKB+14] Cody D Schlaff, Andra Krauze, Arnaud Belard, John J O'Connell, and Kevin a Camphausen. Bringing the heavy: carbon ion therapy in the radiobiological and clinical context. *Radiation oncology (London, England)*, 9(1):88, 2014.

[SKK06] Hiroshi Shinoda, Tatsuaki Kanai, and Toshiyuki Kohno. Application of heavy-ion CT. *Physics in medicine and biology*, 51(16):4073–81, aug 2006.

[sld16] scikit-learn developer. sklearn.cluster.KMeans. *scikit learn*, Aug 2016. URL: `http://scikit-learn.org/stable/modules/generated/sklearn.cluster.KMeans.html`.

[SP94] U Schneider and E Pedroni. Multiple Coulomb scattering and spatial resolution in proton radiography. *Medical physics*, 21(11):1657–1663, 1994.

[SPB+05] Uwe Schneider, Peter Pemler, Jurgen Besserer, Eros Pedroni, Antony Lomax, and Barbara Kaser-Hotz. Patient specific optimization of the relation between CT-Hounsfield units and proton stopping power with proton radiography. *Medical Physics*, 32(1):195, 2005.

[SPH+12] Uwe Schneider, Eros Pedroni, Matthias Hartmann, Jurgen Besserer, and Tony Lomax. Spatial resolution of proton tomography: Methods, initial phase space and object thickness. *Zeitschrift für medizinische Physik*, 22(2):100–8, jun 2012.

[SPL96a] U Schneider, E Pedroni, and a Lomax. The calibration of CT Hounsfield units for radiotherapy treatment planning. *Physics in medicine and biology*, 41(1):111–24, jan 1996.

[SPL96b] U Schneider, E Pedroni, and a Lomax. The calibration of CT Hounsfield units for radiotherapy treatment planning. *Physics in medicine and biology*, 41(1):111–24, jan 1996. URL: `http://www.ncbi.nlm.nih.gov/pubmed/8685250`.

[SPTS08] R W Schulte, S N Penfold, J T Tafas, and K E Schubert. A maximum likelihood proton path formalism for application in proton computed tomography. *Med. Phys.*, pages 4849–4856, 2008.

[SPW+12] J Seco, H R Panahandeh, K Westover, J Adams, and H Willers. Treatment of non-small cell lung cancer patients with proton beam-based stereotactic body radiotherapy: dosimetric comparison with photon plans highlights importance of range uncertainty. *Int. J. Radiat. Oncol. Biol. Phys*, 83:354–61, 2012.

[Tay15] P Taylor. IROC Houston's proton beam validation for clinical trials. *AAPM 57th Meeting*, 2015.

[Tho16] Thoshiba Leading Innovation. NIRS and Toshiba Complete World's First Rotating Gantry with Superconducting Technology for Heavy-ion Radiotherapy System, 2016. URL: `https://www.toshiba.co.jp/about/press/2016{_}01/pr0801.htm`.

[TJM12] Julia Telsemeyer, Oliver Jäkel, and Mária Martišíková. Quantitative carbon ion beam radiography and tomography with a flat-panel detector. *Physics in medicine and biology*, 57(23):7957–71, dec 2012.

[TKSN14] H Tsujii, T Kamada, T Shirai, and K Noda. *Carbon-Ion Radiotherapy, principles, practices and treatment planning*. Springer, 2014.

[TLB+58] C. Tobias, J. Lawrence, J. Born, R. McCombs, J. Roberts, H. Anger, B. Low-Beer, and C. Huggins. Pituitary irradiation with high energy proton beams: A preliminary report. *Cancer Res*, 1958.

[TMI00] MA The MathWorks Inc., Natick. Matlab 2010b, 2000.

[Tur07] J.E. Turner. *Atoms, Radiation and Radiation Protection*. Wiley-VCH, 2007.

[Urb06] László Urbán. A model for multiple scattering in GEANT4. *CERN-Open-2006-077*, 2006.

[Ver15] Joost M Verburg. *Reducing range uncertainty in proton therapy*. PhD dissertation, 2015.

[Wat99] Yoichi Watanabe. Derivation of linear attenuation coefficients from CT numbers for low-energy photons. *Physics in Medicine and Biology*, 44(9):2201–2211, sep 1999.

Bibliography

[WDA11] Mackie T R Wang D and Tom W A. Bragg peak prediction from quantitative proton computed tomography using different path estimates. *Phys. Med. Biol.*, 56:587, 2011.

[WHO16] WHO. WHO | Cancer. *WHO*, 2016. URL: `http://www.who.int/mediacentre/factsheets/fs297/en/`.

[Wil46] R. Wilson. Radiological use of fast protons. *Radiology*, 1946.

[Wil04a] D C Williams. The most likely path of an energetic charged particle through a uniform medium. *Physics in Medicine and Biology*, 49(13):2899, 2004.

[Wil04b] D C Williams. The most likely path of an energetic charged particle through a uniform medium. *Physics in Medicine and Biology*, 49(13):2899, 2004.

[WK08] U Weinrich and C M Kleffner. Comissioning of the carbon beam gantry at the heidelberg ion therapy (hit) accelerator. *11th European Particle Accelerator Conference, Genoa, Italy,*, 2008.

[WK09] Uli Weber and Gerhard Kraft. Comparison of Carbon Ions Versus Protons. *The Cancer Journal*, 15(4):325–32, 2009.

[WW86] H. Q. Woodard and D. R. White. The composition of body tissues. *The British Journal of Radiology*, 59(708):1209–1218, dec 1986.

[WW02] B.A. Weaver and A.J. Westphal. Energy loss of relativistic heavy ions in matter. *Nuclear Instruments and Methods in Physics Research Section B: Beam Interactions with Materials and Atoms*, 187(3):285–301, mar 2002.

[WWH87] DR White, HQ Woodard, and SM Hammond. Average soft-tissue and bone models for use in radiation dosimetry. *The British Journal of Radiology*, 60(717):907–913, sep 1987.

[WWK+15] Matthias Witt, Uli Weber, Daniel Kellner, Rita Engenhart-Cabillic, and Klemens Zink. Optimization of the stopping-power-ratio to Hounsfield-value calibration curve in proton and heavy ion therapy. *Zeitschrift fur Medizinische Physik*, 25(3):251–263, 2015.

[YVC+10] M Yang, G Virshup, J Clayton, X R Zhu, R Mohan, and L Dong. Theoretical variance analysis of single- and dual-energy computed tomography methods for calculating proton stopping power ratios of biological tissues. *Physics in medicine and biology*, 55(5):1343–1362, 2010.

[YZP+12] Ming Yang, X Zhu, Peter Park, Uwe Titt, Radhe Mohan, Gary Virshup, James E Clayton, and Lei Dong. Comprehensive analysis of proton range uncertainties related to patient stopping-power-ratio estimation using the stoichiometric calibration. *Physics in medicine and biology*, 57(13):4095–115, 2012.

[ZE13] Xuping Zhu and Georges El Fakhri. Proton therapy verification with PET imaging. *Theranostics*, 3(10):731–40, 2013.